

1-1-2015

Edge Fracture Prediction Of Dual Phase Steels With Consideration Of Microstructures

Ming Wen
Wayne State University,

Follow this and additional works at: https://digitalcommons.wayne.edu/oa_dissertations

 Part of the [Mechanical Engineering Commons](#)

Recommended Citation

Wen, Ming, "Edge Fracture Prediction Of Dual Phase Steels With Consideration Of Microstructures" (2015). *Wayne State University Dissertations*. 1387.

https://digitalcommons.wayne.edu/oa_dissertations/1387

This Open Access Dissertation is brought to you for free and open access by DigitalCommons@WayneState. It has been accepted for inclusion in Wayne State University Dissertations by an authorized administrator of DigitalCommons@WayneState.

**EDGE FRACTURE PREDICTION OF DUAL PHASE STEELS WITH
CONSIDERATION OF MICROSTRUCTURES**

by

MING WEN

DISSERTATION

Submitted to the Graduate School

of Wayne State University,

Detroit, Michigan

in partial fulfillment of the requirements for the degree of

DOCTOR OF PHILOSOPHY

2015

MAJOR: MECHANICAL ENGINEERING

Approved By:

Advisor

Date

© COPYRIGHT BY

MING WEN

2015

All Rights Reserved

DEDICATION

I dedicate this work to my parents, Jiabing Wen and Yuanjun Li.

ACKNOWLEDGEMENTS

I would like to appreciate my academic advisor Professor Xin Wu for his guidance of this dissertation and financial support from Winter/2011 to Winter /2012; Professor Trilochan Singh for his arrangement and technical suggestions of through my PhD study; Professor Min Jie for his suggestions in FEM, fracture mechanics, and damage mechanics related topics; Professor Emmanuel O. Ayorinde and Professor Qingyu Yang for their suggestions for improving this dissertation.

Professor Teng Liu, visiting Professor from Shenyang Aerospace University, Shenyang, China, planned and initiated experiments of this dissertation and performed all SEM examinations, upon which I continued his work completed planned experiments and analysis, I'd like to express my thanks to his work and suggestions for my experiments.

I'm grateful to my parents for their understanding and financial support to complete this dissertation.

TABLE OF CONTENTS

Dedication	ii
Acknowledgements	iii
List of tables	vi
List of figures	viii
List of symbols	xi
Abbreviations	xiv
CHAPTER 1. Introduction	1
1.1 Classification of steels.....	1
1.2 Dual Phase (DP) steels.....	3
1.3 Fracture modes and types	8
1.4 Damage initiation and evolution	13
1.5 Edge fracture phenomenon of AHSS.....	13
1.6 Punching process and hole expansion test	14
1.7 Research objectives and approaches	16
1.8 Outline of the dissertation	17
CHAPTER 2. Literature review of failure hypothesis	19
2.1 Basics of failure hypotheses	19
2.2 Definition of damage at different scales.....	20
2.3 Yield criteria and damage models.....	23
CHAPTER 3. Hole punching process	29
3.1 Literature review of shearing fracture dominant processes	30
3.2 Observing sheared edge from normal and tangential directions	31
3.3 The effects of investigated parameters on morphologies of sheared edges	32
3.4 Relative heights of rollover, burnish, and fracture zones	38
3.5 FE simulation of hole punching process	45
3.6 Conclusions.....	50
CHAPTER 4. Hole expanding process	51

4.1 Literature review of sheared edge stretching processes	52
4.2 Initiation of main and associated cracks on sheared edges	53
4.3 Experimental observation and data analysis of hole expansion test results	60
4.4 Criteria for edge fracture at macroscale.....	70
4.5 Conclusions.....	75
CHAPTER 5. Analysis of microstructure effects on plasticity and failure of DP steels	76
5.1 Literature review of effects of microstructures on stretchabilities of steel sheets.....	76
5.2 Determination of input conditions for fracture analysis.....	78
5.3 The effects of microstructures on fracture of DP steels.....	84
5.4 The effects of microstructures on constitutive relationships of DP steels.....	94
5.5 Discussions	99
CHAPTER 6. Conclusions and suggestions for future work.....	101
6.1 Conclusions.....	101
6.2 Future research.....	101
Appendix A.....	103
Appendix B.....	106
Appendix C.....	105
Appendix D.....	109
Appendix E.....	113
Appendix F.....	116
Appendix G.....	117
Appendix H.....	118
Abstract	130
Autobiographical statement.....	130

LIST OF TABLES

Table 1-1 Classification of steels	1
Table 1-2 Tensile test specimen geometrical parameters and test conditions	3
Table 1-3 Parameters affecting the edge fracture	15
Table 2-1 Formulas of damage at the atomic scale	20
Table 2-2 Strain and stress controlled voids nucleation law	27
Table 3-1 Investigated parameters for punching process	29
Table 3-2 DP780 (simulated) sheared edge formation process, experimental observation, and “flow-line” analysis	32
Table 3-3 Analysis of sheared edge images of DP780 with C%=10%, 20%, and 30% (observed in OD2)	33
Table 3-4 Sheared edge images of DP 980 GA (1.4) 20 with different orientations and C% (observed in OD2)	35
Table 3-5 Sheared edge images of DP980 GA (1.4) RD with different d_o (observed in OD2)	36
Table 3-6 Sheared edge images of DP980 GA 1.4 and DP780 CR 1.0, 60, RD (observed in OD2)	37
Table 3-7 Sheared edge images of DP780 and DP980 with different C% (observed in OD1)	38
Table 4-1 Investigated parameters for hole expansion test	51
Table 4-2 Comparison of HER for DP780 1.4 from two suppliers (S1 and S2)	60
Table 4-3 Comparison of HER for DP980 1.4 from two suppliers (S1 and S2)	61
Table 4-4 HE test result analysis	62
Table 4-5 Simulation of crack propagation and interference	67
Table 4-6 Data analysis of HER of DP780 and DP980 from two suppliers	73
Table 4-7 C_D values of DP780 and DP980 from two suppliers	74
Table 5-1 Measurement of martensite volume fraction at different thickness locations	79
Table 5-2 Vicker’s Hardnesses of ferrite and martensite in DP steels with different annealing cycles	82
Table 5-3 Parameters for ferrite and martensite phases	83
Table 5-4 GTN model failure related parameters for ferrite	84
Table 5-5 Simulated crack propagation paths in homogeneous and heterogeneous models	87
Table 5-6 Ferrite and martensite phases in RVE models with different $V_M\%$	89

Table 5-7 Stress and strain contours on outside surfaces of homogeneous and heterogeneous RVE models	91
Table 5-8 Cracks on outside surfaces of RVE with VM%=30% but different spatial (random) distributions	93

LIST OF FIGURES

Figure 1-1 Three generations AHSS.....	2
Figure 1-2 Dimensions of tensile test specimen	3
Figure 1-3 Engineering stress-strain curve of DP980.....	4
Figure 1-4 Typical true and engineering stress-strain curves of tested DP980.....	5
Figure 1-5 True stress-strain curves of different steels (provided by a US automaker)	6
Figure 1-6 Engineering stress-strain curves of different steels (provided by a US automaker)	6
Figure 1-7 Grain structures of DP780 and DP980.....	8
Figure 1-8 Fracture modes.....	9
Figure 1-9 Fracture types.....	10
Figure 1-10 Typical ductile fracture.....	11
Figure 1-11 Typical brittle fracture	11
Figure 1-12 Definition of damage initiation point and evolution process for DP980.....	13
Figure 1-13 AHSS edge fracture phenomena.....	14
Figure 1-14 Punching and hole expanding processes.....	15
Figure 1-15 The flow chart of the critical factors influencing the edge fracture	16
Figure 3-1 Hole punching process	29
Figure 3-2 Observation Direction (OD) 1 and 2	31
Figure 3-3 Sheared edge observation direction 1 (OD1), Rolling (R) and Transverse (T) directions	38
Figure 3-4 Original and processed images for four zones of sheared edge (observed in OD1)	39
Figure 3-5 Analysis of relative heights for rollover, burnish, and fracture zones of sheared edge.....	40
Figure 3-6 RRH with respect to d_0 , with different C%, for DP780 and DP980	40
Figure 3-7 RRH with respect to C%, with different d_0 , for DP780 and DP980	41
Figure 3-8 RRH with respect to UTS, with C%= 20% RD different d_0	41
Figure 3-9 RBH with respect to d_0 , with different C%, for DP780 and DP980.....	42
Figure 3-10 RBH with respect to C%, with different d_0 , for DP780 and DP980.....	42
Figure 3-11 RBH with respect to UTS, with C%= 20% RD different d_0	43
Figure 3-12 RFH with respect to d_0 , with different C%, for DP780 and DP980.....	44

Figure 3-13 RFH with respect to C%, with different d_0 , for DP780 and DP980	44
Figure 3-14 RFH with respect to UTS, with C%= 20% RD, different d_0	45
Figure 3-15 Sketch of the punching process model	46
Figure 3-16 Von Mises contour of DP780 under C%=10%, 20%, and 30% conditions	47
Figure 3-17 Von Mises contour within AOI of DP600, DP780, and DP980 under C%=10% condition	48
Figure 3-18 Reaction forces of punch in vertical direction under C%=10% condition.....	49
Figure 3-19 External work of punching process model with different steel grades under C%=10% condition	49
Figure 4-1 Two types hole expansion tests	51
Figure 4-2 Main crack on sheared edge of DP780 GA 1.4, 10%, 80mm (Supplier 1).....	54
Figure 4-3 Associated crack on sheared edge of DP780, GA 1.4, Supplier 1.....	55
Figure 4-4 Associated cracks on sheared edge of DP980, GA 1.4, Supplier 2.....	55
Figure 4-5 Sketch of hole expansion test model.....	56
Figure 4-6 Deformed metal sheet in HE test (quart model)	56
Figure 4-7 Sketches of sheared edge profiles	57
Figure 4-8 Stress distribution on sheared edges, initial hole diameter=20mm.....	58
Figure 4-9 Histories of Von Mises stresses at different locations of sheared edges	59
Figure 4-10 Hole expansion test results of DP980, GA 1.0, with different d_0 and C%	60
Figure 4-11 Typical edge crack phenomenon of steel sheet from Supplier 1, DP980 0.96	64
Figure 4-12 Typical edge crack phenomenon of steel sheet from Supplier 2, DP780 EG 1.4	64
Figure 4-13 Edge cracks on sheared edges of DP980 from two suppliers	66
Figure 4-14 Sketch of dual-crack model	67
Figure 4-15 C_D values for DP780 and DP980 from two suppliers	75
Figure 5-1 Typical grain structure image of DP980	79
Figure 5-2 Three families of shapes originating from a circle with different thermomechanical histories ..	81
Figure 5-3 Strain hardening curves of martensite and ferrite	84
Figure 5-4 Tensile fracture area of a DP steel	85
Figure 5-5 Crack propagation in a DP steel.....	86
Figure 5-6 Sketch of heterogeneous model with one hard inclusion.....	86

Figure 5-7 Sketch of RVE model	89
Figure 5-8 Failed elements on outside surface of RVE	92
Figure 5-9 Crack initiation and propagation in heterogeneous RVE models with different martensite volume fraction	93
Figure 5-10 Stress-strain curves of RVE models with different martensite volume fraction	95
Figure 5-11 The effects of martensite volume fraction on ultimate tensile strength (UTS) and damage initiation strain (DIS)	95
Figure 5-12 Total energy to split RVE models with different martensite volume fractions	96
Figure 5-13 Total energy to split RVE models with different martensite strengths	97
Figure 5-14 The effects of martensite strength on ultimate tensile strength (UTS) and damage initiation strain (DIS).....	97
Figure 5-15 External work for RVE with different martensite strengths	98
Figure 5-16 Stress-strain curves of RVE models with different martensite damage initiation strain	98
Figure 5-17 Stress-strain curves of RVE models with VM%=30% but different spatial (random) distributions.....	99

LIST OF SYMBOLS

α, β	Material constants of Wilkins, Streit, and Reaugh model
γ_s	Specific surface energy
$\delta\tilde{A}, \delta A$	Effective (remaining) area and total undamaged area
$\delta V_s, \delta V$	Void volume and total volume of RVE
ε	True strain
$\dot{\varepsilon}^*$	Non-dimensional plastic strain rate of Johson-Cook model
ε_f	Failure strain
$\bar{\varepsilon}^p$	Equivalent plastic strain
$\bar{\varepsilon}_S^{pl}, \bar{\varepsilon}_D^{pl}$	Equivalent plastic strain (S: shear; D: ductile)
$\bar{\varepsilon}_0^{pl}, \bar{\varepsilon}_f^{pl}$	Initial and failure values of the equivalent plastic strain, assumed to depend on the plastic strain rate $\dot{\bar{\varepsilon}}_f^{pl}$
$\Delta\bar{\varepsilon}^{pl}$	Increment of the equivalent plastic strain
$\dot{\bar{\varepsilon}}^{pl}, \dot{\bar{\varepsilon}}_{kk}^{pl}$	Equivalent plastic strain rate and equivalent principle plastic strain rate
η, σ^*	Triaxiality or dimensionless pressure-stress ratio
θ_s	Shear stress ratio
σ	True stress
$\tilde{\sigma}, \tilde{\varepsilon}$	Effective stress and effective strain
σ_c	Fracture strength
σ_{eq}	Equivalent tensile stress or Von Mises stress
σ_m	Average stress or hydrostatic stress
σ_N, ε_N	Mean nucleating stress and strain
σ_y	Engineering yield stress at 0.2% offset
ψ	Continuum parameter of damage
ω_S, ω_D	State variables that increase monotonically with plastic deformation proportional to the incremental change in equivalent plastic strain
A	Loading condition parameter of Wilkins, Streit, and Reaugh model

C	Constant value of Von Mises and Tresca criteria
C%	Clearance
C_1, C_2	Coefficients of criterion proposed by Adamczyk and Michal
$C_3, C_4, C_5, C'_3, C'_4, C'_5$	Coefficients of criteria proposed by Comstock, Scherrer, and Adamczyk
C_6, C_7, C_D	Coefficients of criterion proposed in this dissertation
D	Overall damage
D_1, D_2	Damage at atomic scale
D_3, D_4, D_5, D_6, D_7	Material constants of Johnson-Cook model
d_0, d_f	Original (or initial) hole diameter and hole diameter at failure
E	Young's (Elastic) modulus
\tilde{E}	Elasticity modulus of the damaged material
e	Engineering (nominal) strain
e_u, e_t	Uniform elongation (UE) and total elongation (TE)
e_w, e_T	True width strain and true thickness strains
f	Void volume fraction in an RVE
f_c	Critical void fraction for void coalescence
f_f	Void volume fraction at fracture
$\dot{f}_{\text{nucleation}}$	Volume change rate due to voids nucleation
\dot{f}_{growth}	Volume change rate due to voids growth
f_N^n, f_N^s	Volume fractions of void nucleating particles (n: strain-controlled, s: stress-controlled)
h_r	Averaged rollover zone height
h_b	Averaged burnish zone height
h_f	Averaged fracture zone height
h_0	Summary of averaged height of rollover, burnish, and fracture zones
H_M, H_F	Hardnesses of martensite and ferrite phases
$H_1, H_2, H_3, H_4, H_5, H_6$	Material constants of Hill yield criterion
K	Strength coefficient

n	Work hardening exponent
n_t	Work hardening rate
q_1, q_2, q_3	Material constants of GTN model
r	Plastic strain ratio or Lankford value
r_m	Mean plastic strain ratio of criterion proposed by Adamczyk and Michal
S	Engineering (nominal) stress
S_N^n, S_N^s	Standard deviations (n: strain-controlled, s: stress-controlled)
t, t_o, t_f	Thickness, original thickness, and final thickness
$T, T_{melt}, T_{transition}, T^*$	Current, melting, transition, and homologous temperatures
$V_M\%$	Volume fraction of martensite phase of DP steel
w_1, w_2	Hydrostatic-pressure term and Asymmetric strain weighting term of Wilkins, Streit, and Reaugh model
w_o, w_f	Original width and final width

ABBREVIATIONS

AHSS	Advanced High Strength Steels
AOI	Areas of Interest
ASTM	American Society for Testing and Materials
CR	Cold Rolling
DP780, DP980	Dual Phase steels with Ultimate Tensile Strength (UTS) at least 780 MPa and 980 MPa
DIS	Damage Initiation Strain
FEM, FEA	Finite Element Method, Finite Element Analysis
FLC	Forming Limit Curve
GA	Galvanization
GI	Galvanized Iron
GTN	Gurson, Tvergaard, and Needleman damage model
HE	Hole Expansion test
HER	Hole Expansion Ratio
HSS	High Strength Steels
OD1, OD2	Observation Direction 1 (normal) and 2 (tangential)
PEEQ	Equivalent Plastic Strain
RD, TD	Rolling Direction, Transverse Direction
RBH	Relative Height of Burnish zone, which equals to h_b/h_0
RFH	Relative Height of Fracture zone, which equals to h_f/h_0
RRH	Relative Height of Rollover zone, which equals to h_r/h_0
RVE	Represent Volume Element
S1, S2	Supplier 1 and Supplier 2
SEM	Scanning Electron Microscope
TE	Total Elongation
UE	Uniform Elongation

UTS

Ultimate Tensile Strength

YPE

Yield Point Elongation

CHAPTER 1 INTRODUCTION

In this chapter, research related conceptions, objectives, and approaches are introduced.

1.1 Classification of steels

There are many ways to classify automotive steels, the most commonly used classification are by metallurgical designation, strength, mechanical properties, or forming parameters, as shown in Table 1-1.

Table 1-1 Classification of steels [1,2,3]

Metallurgical Designation	Strength	Mechanical Properties or forming parameters
Low-strength steels	High-Strength Steels(HSS) Yield Strength: 210 ~ 550 MPa Tensile Strength: 270 ~ 700 MPa	Total elongation (TE or e_t)
Conventional HSS		Work hardening exponent (n-value)
Newer types of AHSS	Ultra-High-Strength Steels (UHSS) Yield Strength > 550 MPa Tensile Strength > 700 MPa	Hole expansion ratio (HER)
Higher strength steels		

For the first column the Table 1-1, steels are classified according to metallurgical designations into four categories: low-strength steels, including Interstitial-Free (IF) steel and Mild steel; conventional HSS including Carbon-Manganese (CM) steel, Bake Hardenable (BH) steel, High-Strength Interstitial-Free (HSIF) steel, and High-strength low-alloy (HSLA) steel; Newer types of AHSS, including Dual Phase (DP) steel, Transformation-Induced Plasticity (TRIP) steel, Complex Phase (CP) steel, and Martensitic (MS) steel; Higher strength steels, including Ferritic-Bainitic (FB) steel, TWinning-Induced Plasticity (TWIP) steel, Nano steels, Hot-Formed (HF) steel, and Post-Forming Heat-Treated (PFHT) steel.

Conventional High Strength Steels (HSS) have been widely used in the automotive industry with solid technology base, while Advanced High Strength Steels (AHSS) are a relatively new category and with relatively less accumulation of technical experience.

As shown in Figure 1-1, for conventional HSS, the general trend can be summarized as: with the increase of tensile strength, Total Elongation (TE) decrease, but this trend may not apply to AHSS.

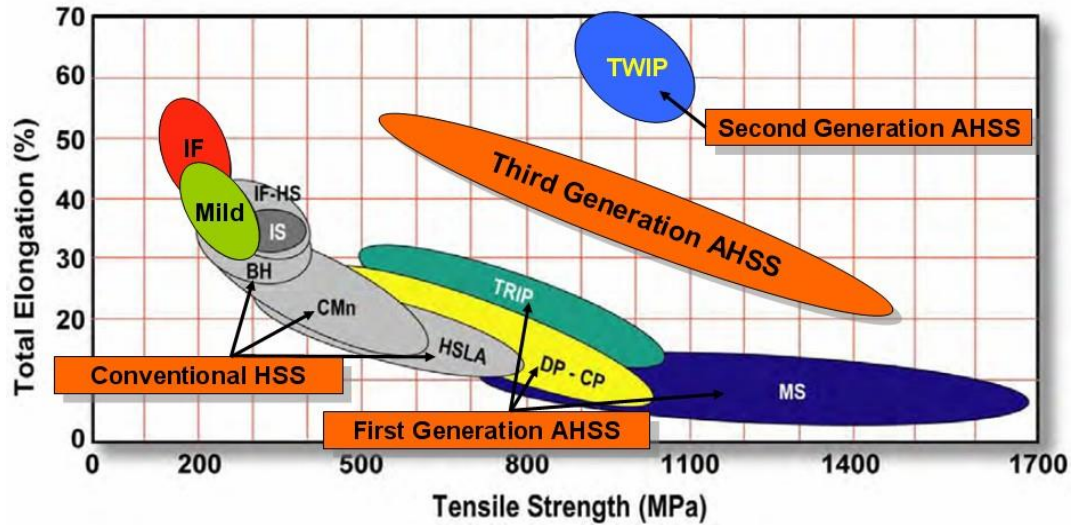


Figure 1-1 Three generations AHSS [1]

The first generation AHSS

The first generation AHSS mainly includes Dual Phase (DP) steels, Complex Phase (CP) steels, Transformation Induced Plasticity (TRIP) steels, and Martensitic (MS) steels. Comparing with conventional HSS, they have improved tensile strength but lower total elongation.

The second generation AHSS

“Comparing with the first generation AHSS, the second generation has a “major jump” in forming capability, obtained via the austenite-based products, such as TWinning Induced Plasticity (TWIP) steels that are just now beginning preproduction experimentation. While these steels claim 60-percent total elongation and very high n-values, they are costly due to the high cost of alloying elements. Many researchers believe that most parts do not require the mechanical properties of the second generation AHSS grades [4].”

The third generation AHSS

The third generation steels are in development to meet the increased design requirements for automotive industry. The third generation steels have higher elongation ratio and similar strength range as compared with the first generation steels; have lower elongation ratio, less complex compositions, but wider strength range as compared with the second generation.

It's worth mentioning that, different steel companies produce the same grade steels with different chemical composition and manufacturing processes; for this reason, steels marked with the same grade code but from different suppliers often show different mechanical performance in the same forming processes. For automotive companies, it is critical to choose the suitable steel, which can meet design requirements at minimum cost.

1.2 Dual Phase (DP) steels

Research in this dissertation focuses on DP steels, which belong to the first generation AHSS and featured with dual phase grain structures.

1.2.1 Mechanical properties of DP steels

Tensile test is the most widely used method to measure mechanical properties of steels, according to ASTM E646-07 [5], tensile specimens are machined according to the dimensions in Figure 1-2 and tested under controlled conditions:

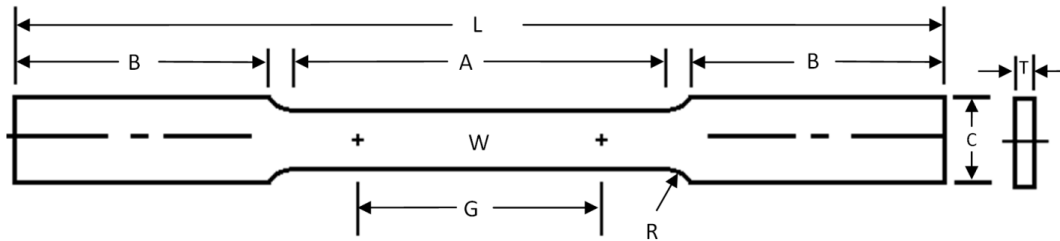


Figure 1-2 Dimensions of tensile test specimen [18]

Test specimen geometrical parameters and test condition are listed in Table 1-2

Table 1-2 Tensile test specimen geometrical parameters and test conditions

Tensile test specimen geometrical parameters	
G: Gage length. 50.0 ± 0.10 (mm)	W: Width. 12.5 ± 0.25 (mm)
T: Thickness. Thickness of material	R: Radius of fillet, min. 13 (mm)
L: Overall length, min. 200 (mm)	A: Length of reduced section, min. 60 (mm)
B: Length of grip section, min. 50 (mm)	
The uniaxial tensile test condition	
1. Strain rate is of the order of 10^{-2} to 10^{-4} /sec.	
2. Temperature is between 20 and 30 °C.	
3. Measurements are restricted to a gage section that experiences a state of uniaxial tensile stress during uniform deformation.	

For the test condition listed in Table 1-2, for a standard uniaxial tensile test, the strain-stress relationship beyond uniform deformation are ignored. In this dissertation, the strain-stress relationship beyond uniform deformation to fracture is of interest.

In tensile test, data of force and displacement were obtained from test system, such as Instron 8801, by processing force and displacement data, stress-strain curve is obtained, as shown in Figure 1-3.

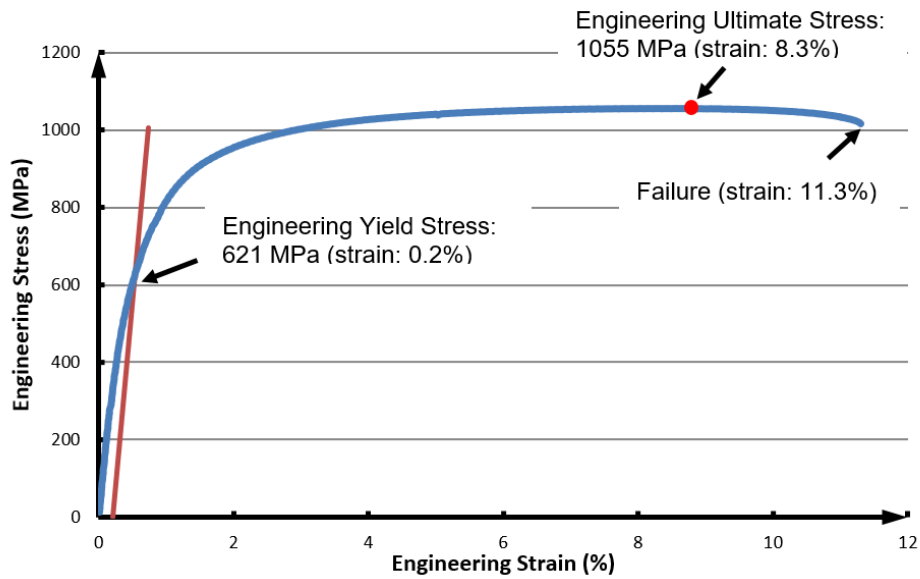


Figure 1-3 Engineering stress-strain curve of DP980

Figure 1-3 is the engineering (nominal) stress-strain curve of a DP980 steel. By analyzing the stress-strain curve, characterize parameters, such as elastic modulus, E , engineering yield stress at 0.2% offset, σ_{yield} , engineering ultimate stress, UTS, failure strain, ϵ_f , work hardening exponent, n value, uniform elongation (UE) and total elongation (TE) were obtained.

Engineering stress, S , and Engineering strain, e , can be converted to true stress and true strain according to following definitions:

$$\text{True strain, } d\epsilon = \frac{d\ell}{\ell}, \text{ or } \epsilon = \ln(1 + e) \quad (1.1)$$

$$\text{True stress, } \sigma = \frac{F}{A}, \text{ or } \sigma = S(1 + e) \quad (1.2)$$

The true stress-strain curve of DP980 were obtained using Equation (1.1) and (1.2), as shown in Figure 1-4.

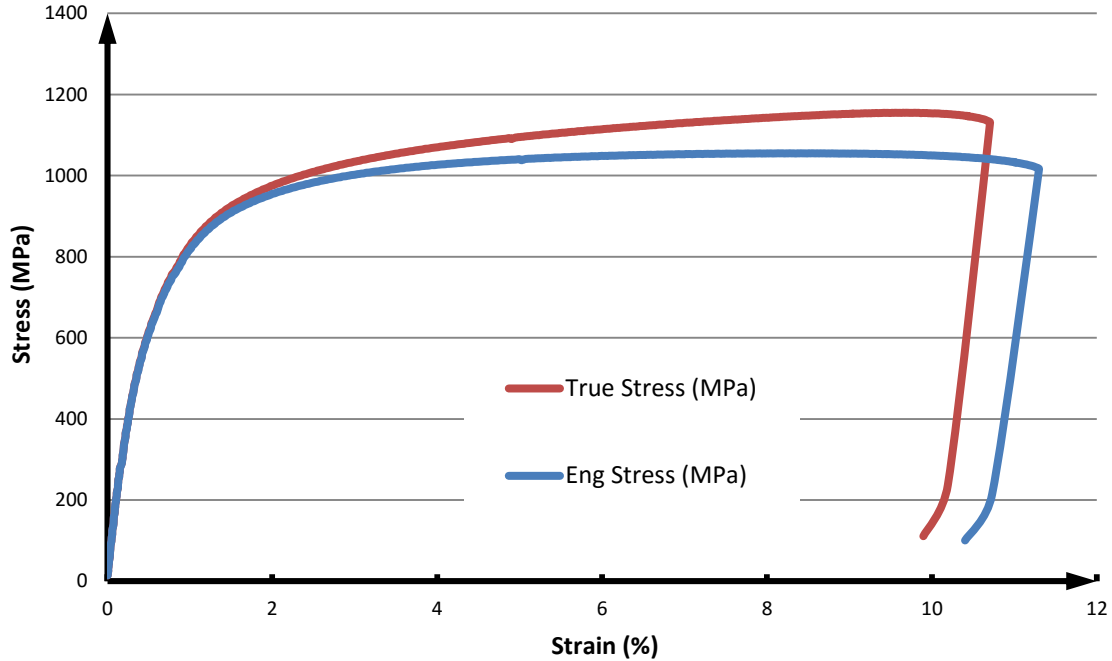


Figure 1-4 Typical true and engineering stress-strain curves of tested DP980

It is worth mentioning that, Equation (1.1) is useful only up to the ultimate tensile strength (UTS) point, which is the onset point of necking. In the engineering stress-strain curve, as shown in Figure 1-3, after the UTS point the length changes are localized in the necked zone, so the engineering strain, which involves a measurement using the entire gage section, cannot be used to calculate the true strain.

In Figure 1-5 and Figure 1-6, true stress-strains and engineering stress-strain curves of DP600, DP780, DP980, and HSLA 50 are presented respectively. For technical parameters of DP steels please reference Appendix A.

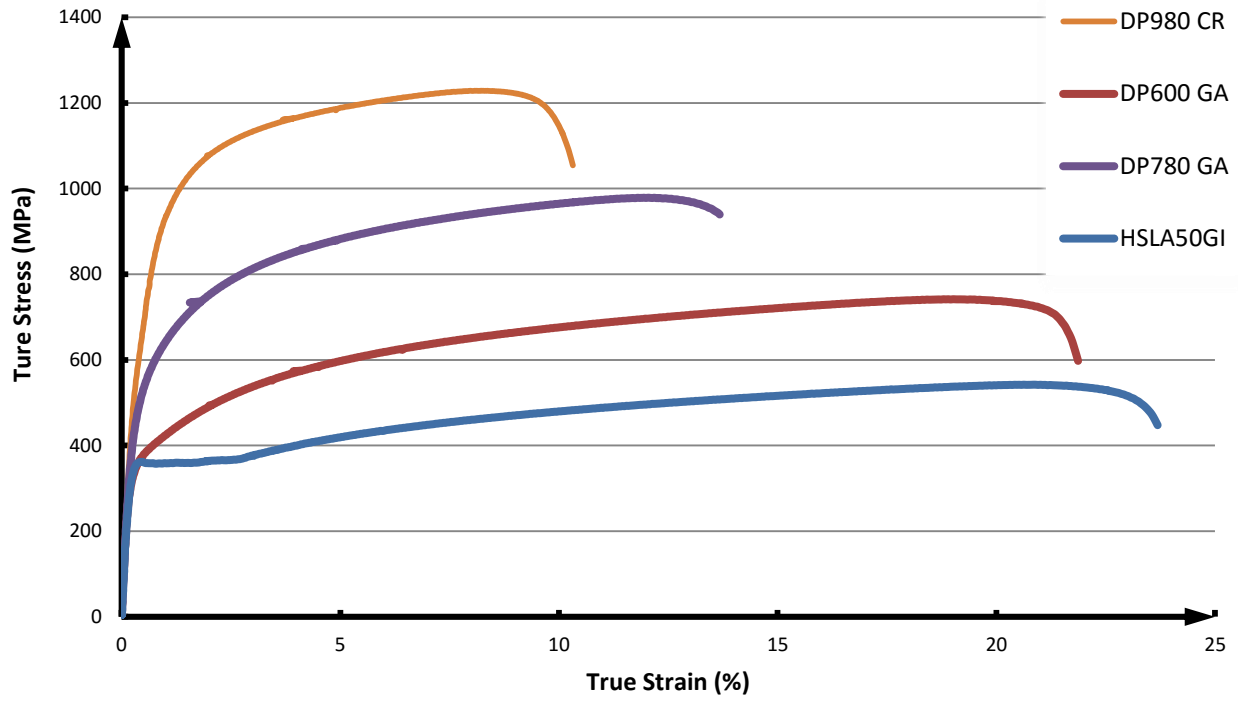


Figure 1-5 True stress-strain curves of different steels (provided by a US automaker)

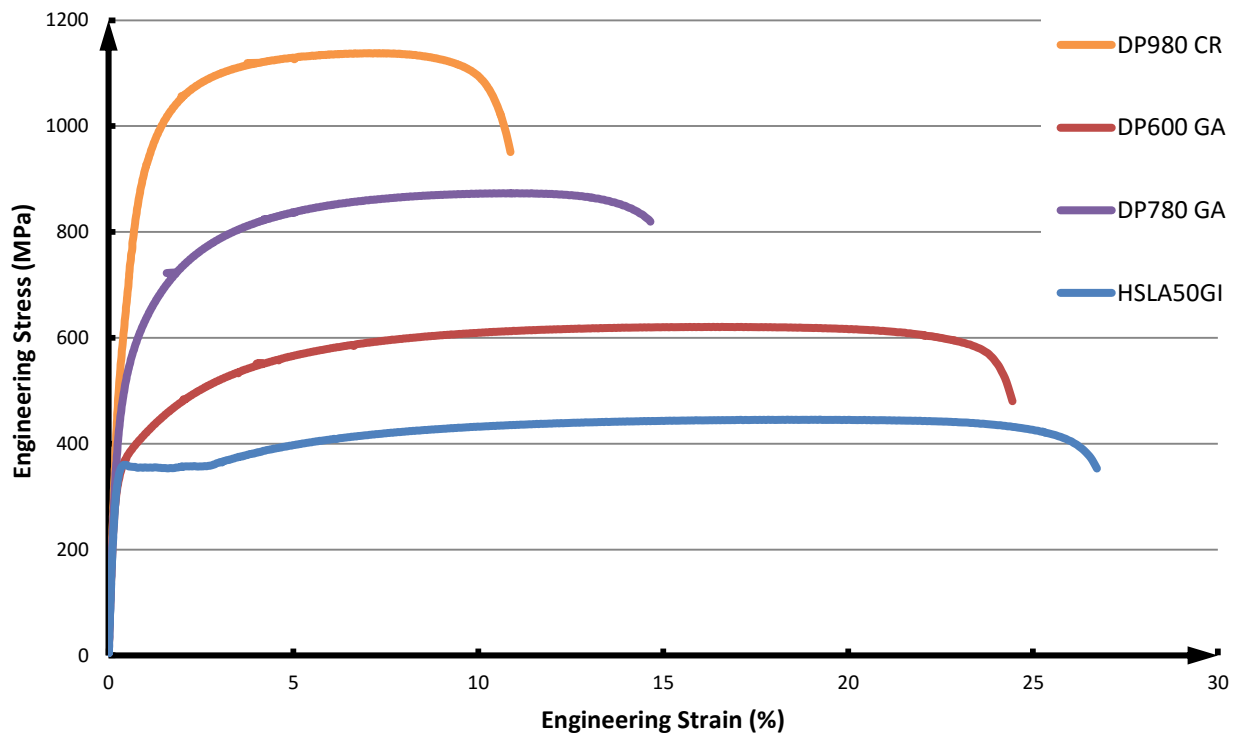


Figure 1-6 Engineering stress-strain curves of different steels (provided by a US automaker)

In Figure 1-5 and Figure 1-6, for steel codes, “CR” stands for cold rolling; “GA” stands for galvanization, “GI” stands for galvanized iron. Comparing stress-strain curves of presented DP600, DP780, DP980, as the increase of UTS, the plastic deformation zone decreases. In comparing HSLA with DP steels, DP steels show no obvious yield point elongation (YPE) phenomenon.

Tensile strain hardening exponent, n-value [5]

The mathematical representation used in the method is a power law curve of the form:

$$\sigma = K\varepsilon^n \quad (1.3)$$

K: strength coefficient.

n: strain-hardening exponent.

Plastic strain ratio, r-value, or Lankford value

The plastic strain ratio is considered a direct measure of sheet metal's drawability and is useful for evaluating materials intended for forming shapes by deep drawing. Determining the plastic strain ratio is governed by ASTM E517 [6].

$$r = \frac{\varepsilon_w}{\varepsilon_t}, \text{ or } \frac{\varepsilon_{22}}{\varepsilon_{33}} \quad (1.4)$$

$\varepsilon_w = \ln(w_f/w_o)$, true width strain; w_o and w_f are original and final widths of the specimen, respectively.

$\varepsilon_t = \ln(t_f/t_o)$, true thickness strain; t_o and t_f are original and final thicknesses.

1.2.2 Grain structures of DP steels

A polycrystalline material consists of many crystals or grains, each of which has the same crystal lattice orientation. Grains form as a result of solidification or other phase transformation processes, grain structure of a solid is an arrangement of differently oriented grains, surrounded by grain boundaries. Grains shape and size change in the course of manufacturing process and thermal treatment processes, for example in rolling process and in recrystallization annealing. For common engineering metals, the normal grain size varies between 1 μ m to 1000 μ m [7].

DP steels are characterized by a grain structure consisting of dispersion of harder martensite particles in softer, ductile ferrite matrix [8]. Figure 1-7 are metallographic images of DP780 and DP980, observing using an optical microscope. In both images, brighter particles are martensite grains, darker areas are ferrite matrix.

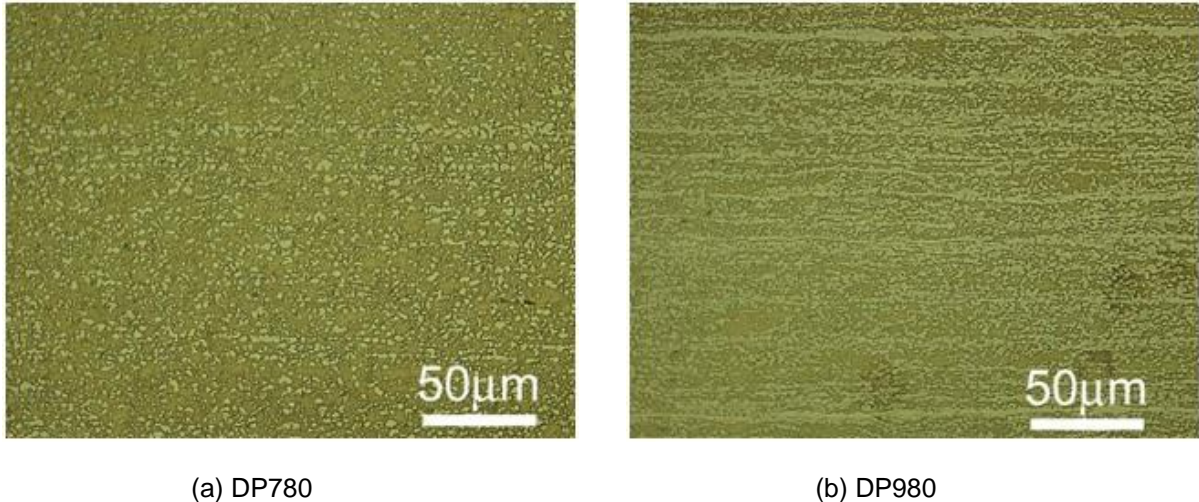


Figure 1-7 Grain structures of DP780 and DP980

DP steels are produced by controlled cooling from the austenite phase (in hot-rolled products) or from the two-phase ferrite plus austenite phase temperature region (for continuously annealed cold-rolled and hot-dip coated products) to transform some austenite to ferrite before a rapid cooling transforms the remaining austenite to martensite [1].

"In DP steels, carbon enables the formation of martensite at practical cooling rates by increasing the hardenability of the steel. Manganese, chromium, molybdenum, vanadium, and nickel, added individually or in combination, also help increase hardenability. Carbon also strengthens the martensite as a ferrite solute strengthener, as do silicon and phosphorus. These additions are carefully balanced, not only to produce unique mechanical properties, but also to maintain the generally good resistance spot welding capability. However, when welding the highest strength grade (DP700/1000) to itself, the spot weldability may require adjustments to the welding practice [1]".

1.3 Fracture modes and types

The deformation of a crack can be classified into three modes, and its fractographies can be classified into three types, as described below.

1.3.1 Fracture modes

In fracture mechanics, a crack is considered, or simplified, as a cut in a body. Its opposite boundaries are the crack surfaces, also called crack faces or crack flanks, which are assumed traction free. There are three types of crack opening mode, as shown in Figure 1-8.

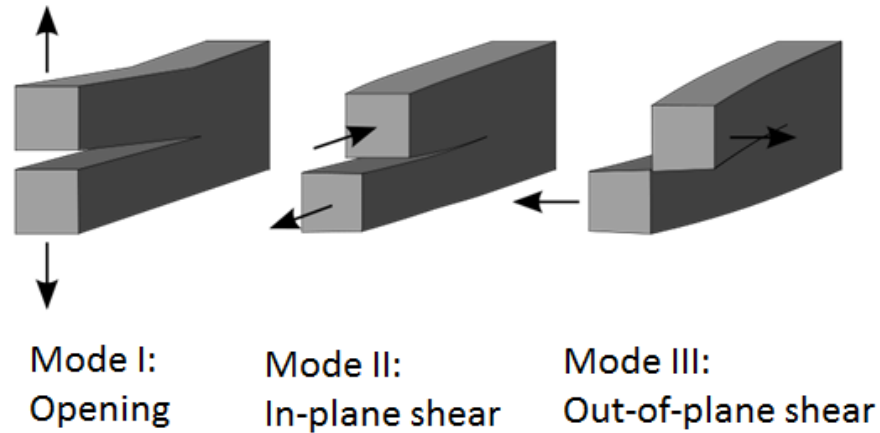


Figure 1-8 Fracture modes [9]

Figure 1-8 demonstrates three ways of applying a force to enable a crack to propagate:

Mode I crack (opening mode): a tensile stress normal to the plane of the crack;

Mode II crack (sliding mode): a shear stress acting parallel to the plane of the crack and perpendicular to the crack front;

Mode III crack (tearing mode): a shear stress acting parallel to the plane of the crack and parallel to the crack front.

In this dissertation, for crack propagation processes, the punching process can be simplified as mode II crack case, and the hole expansion can be simplified as mode I crack case.

1.3.2 Fracture types

Fracture types can be classified into three types, as shown in Figure 1-9.

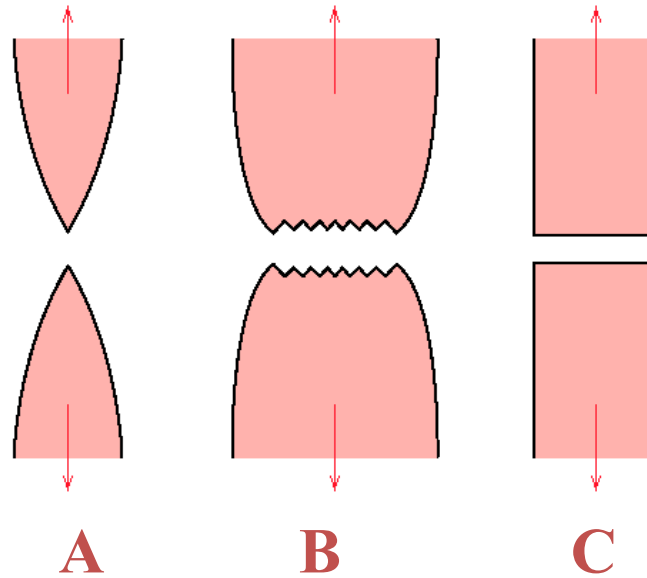


Figure 1-9 Fracture types [10]

Figure 1-9 demonstrates three fracture types:

- A. Highly ductile fracture, in which the specimen necks down to a point. It happens for soft metals (e.g. Pb, Au) at room temperature, polymers, and glasses at high temperatures.
- B. Moderately ductile fracture after necking, it is typical for metals.
- C. Brittle fracture without showing any plastic deformation. It happens in ceramics, and in cold metals below the brittle-to-ductile transition temperature.

It is notable that the classification of fracture types is relatively arbitrary, different industries have different preferences to classify whether the material is brittle or ductile, as shown in Figure 1-10 and Figure 1-11.

1) Ductile fracture

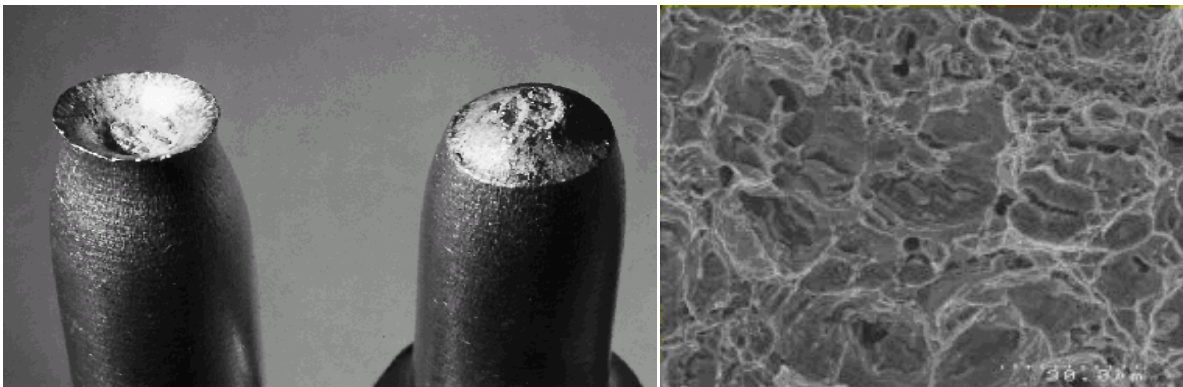


Figure 1-10 Typical ductile fracture [8]

From the viewpoint of energy, the ductile fracture involves a large amount of plastic deformation, as micro voids coalescence absorbs high energy during ductile failure. Thus, this is a high-energy fracture mode.

In microscale, ductile fracture of metals are essentially from atomic de-cohesions following dislocations piling up in metals or growth and coalescence of cavities induced by large deformation in the vicinity of inclusions [1]. In the micromechanics framework, this process can be simplified as the growth of a spherical or elliptic hole in a plastic medium subjected to large strains and the problem can be solved analytically or numerically. From the continuum damage mechanics point of view, this process is a reduction of the resisting area in any plane of a Representative Volume Element (RVE) that is governed by the elastic energy and the accumulated plastic strain [11].

In practical, for ductile crack the formation and growth process is usually stable and can be detected before the final fracture, so it is less catastrophic. As a structure is loaded, under the effect of local strain and stress, various micro-defects such as microvoids and microcracks may grow and coalesce, forming macro crack(s). As the load increases or material deteriorates, voids nucleate at crack tip, and these voids grow and finally link to the main crack. The deteriorate of the structure accelerate as the process of crack propagates, till the whole structure fail.

2) Brittle fracture

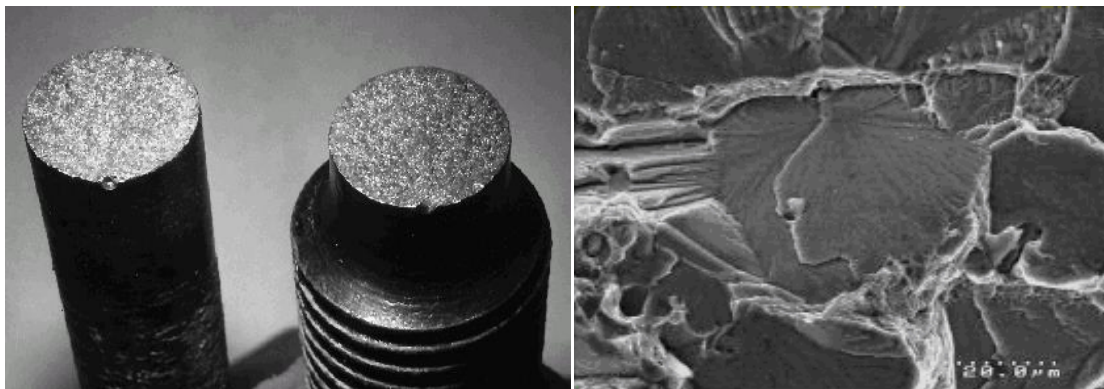


Figure 1-11 Typical brittle fracture [10]

A material is considered brittle when it breaks without a large amount of plastic strain and any dissipation prior to cracking (e.g., glass and some ceramics). It is considered as quasi-brittle when the

dissipation prior to cracking exists with no or negligible permanent strains (e.g., concrete and some ceramics) [12]. From the viewpoint of energy, the brittle fracture involves little plastic deformation and low energy absorption before fracture, so that it can also be classified as low energy mode. Brittle metals usually fail by transgranular (transcrystalline) cleavage. In most cases metals do not fail along grain boundaries, but under special circumstances, cracks can form and propagate along grain boundaries forming intergranular (intercrystalline) cracks [10].

The ductile and brittle fracture are transferable under different conditions. For example, at low temperature (below a critical value), the fracture type of steel is brittle, but at high temperature (above the critical value), the fracture type becomes ductile.

Griffith (1921, 1924) was the first to explain the fracture strength of glass using the fact that glassy materials can harbor crack-like flaws [12], introduced the concept of energy of de-cohesion used in linear elastic fracture mechanics by cracking through the strain energy release rate variable G , but the study contained nothing about damage prior to crack initiation. The mathematical equation and a non-mathematical explanation of the main concepts of Griffith theory are quoted here:

$$\sigma_c = \sqrt{\frac{2 \cdot E \cdot \gamma_s}{\pi \cdot a}} \quad (1.5)$$

E : elasticity modulus.

γ_s : specific surface energy.

a : flaw length.

In brittle fracture, cleavage mode failure defined as the rapid propagation of a crack normal to particular crystallographic plane, and involves breaking bonds (atomic de-cohesions), the local stress reach to a certain level which sufficient to overcome the cohesive strength (debonding) of the material, but lower than the lever which could produce slips (plastic deformation) [13]. The cleavage forces are higher than the debonding forces but are below the forces that could produce slips. In microscale level, usually a sharp microcrack could lead to sufficient local stress concentration and initiate the cleavage fracture [9].

In practical, brittle fracture in materials are more catastrophic, because it happens without any obvious outsider indicator and hard to be detected before the final fracture, so it is critical to develop criteria for predicting the brittle fracture for materials.

1.4 Damage initiation and evolution

Fracture mechanic mainly used to analyze the crack propagation, while damage mechanics used to analyze the process before macro-crack formation.

Figure 1-12, damage initiation point and evolution process on DP980 curve.

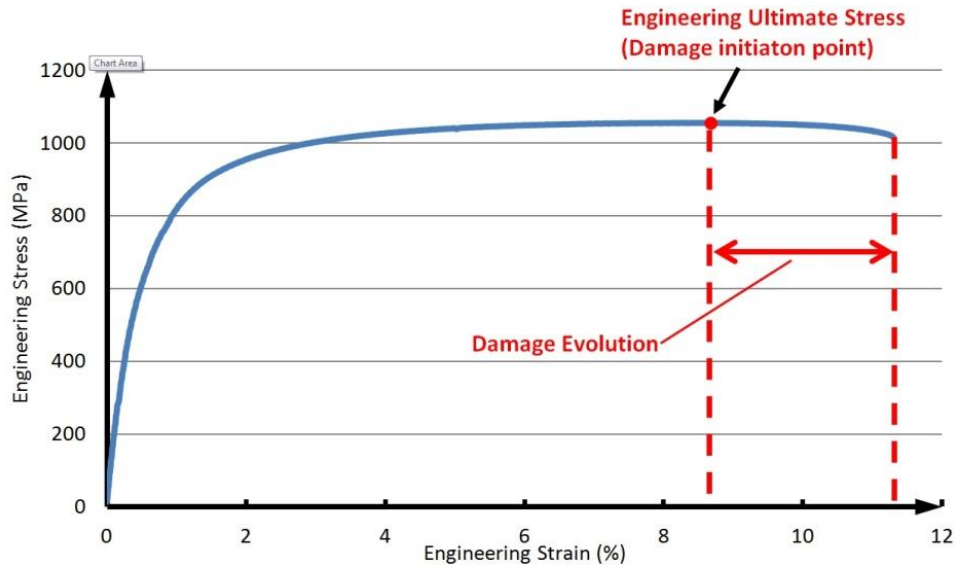
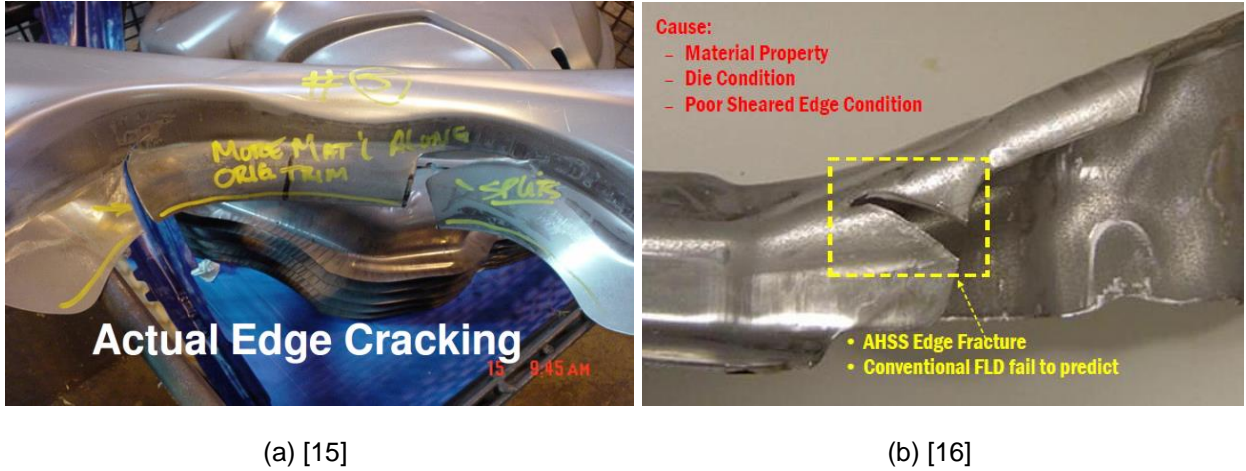


Figure 1-12 Definition of damage initiation point and evolution process for DP980

In Figure 1-12, during the tensile test, after the engineering ultimate stress, the necking phenomenon start. According to ABAQUS Manual [14] and “A Course on Damage Mechanics” by Lemaitre [13], the start point of material weakening is defined as the damage initiation point, after the point the process until fracture is defined as damage evolution process. In damage evolution process, Young’s modulus of the material starts to decrease gradually to zero, which implies the material completely failed and has no load carrying capacity.

1.5 Edge fracture phenomenon of AHSS

During forming steel parts, the phenomenon crack(s) initiate and propagate at the sheet metal edge is called "edge fracture", "edge split", or "edge cracking", as shown in Figure 1-13. The mechanisms of edge fracture phenomenon of AHSS is unclear and no effective way to predict this phenomenon, which limits the application of AHSS.



(a) [15]

(b) [16]

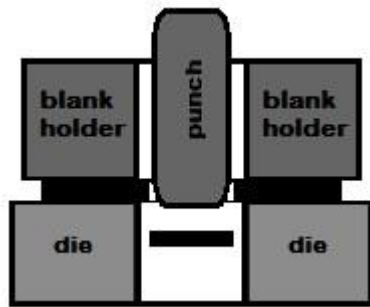
Figure 1-13 AHSS edge fracture phenomena

Figure 1-13 shows the failed AHSS workpieces with edge cracking phenomenon. For DP steels, edge cracking is hard to predict using the method apply to traditional steels. Studies show cracking occurs at strain lower than those predicted by the forming limit curves (FLC) [16], and is not restricted to specific strength level, supplier, or stamping planet [17]. Based on experience engineers in automotive industry have speculated that the edge fracture is affected by edge quality, material property, and die condition.

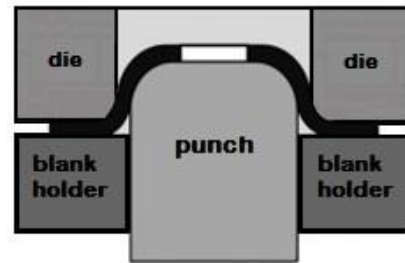
Among these three categories of possible root causes, the material property and sheared edge condition are directly related to microstructures of steels, so the research on the correlation between microstructure parameters and the edge fracture is necessary.

1.6 Punching process and hole expansion test

Hole expansion (HE) test with controlled parameters is used to investigate the effects of controlled parameters on edge fracture. The hole expansion tests include two major technical steps, punching and hole expanding, as shown in Figure 1-14 (a) and (b).



(a) Punching process



(b) Hole expanding process

Figure 1-14 Punching and hole expanding processes

Two major technical steps, or processes, of hole expansion test are:

Step 1: Hole punching process, as shown in Figure 1-14 (a), a tool punches through the sheet metal removes unwanted material and creates a hole. In this process, metal sheet fracture occurs within the clearance zone (the space between the punch and the die), creates the sheared edge, which can be divided into four zones: rollover, burnish, fracture, and burr zones, as shown in Figure 3-1. Details about this process will be discussed in Chapter 3.

Step 2: Hole expansion process, as illustrated in Figure 1-14 (b). During this process, the flat punch pushes one side of the sheet metal and expands the punched hole until a macro crack is observed with the naked eye, formed at the sheared edge of the hole. Details about this process will be discussed in Chapter 4.

The parameters affecting the edge fracture phenomenon are classified into two categories related to the engineering process and material properties, as listed in Table 1-3.

Table 1-3 Parameters affecting the edge fracture

Engineering Process parameters		Material parameters	
Hole diameters (d_0)	20, 40, 60, 80	Total and uniform elongations	e_t, e_u
Clearances (C%)	10%, 20%, 30%	Yield and ultimate strengths	σ_y, UTS
Thickness	0.96, 1.0, 1.4, 1.8	Suppliers	S1, S2
Tool conditions	material, tip geometry, wear-out state	Martensite volume fraction	$V_M\%$
Punching speed	strain rate effect, temperature	Martensite and ferrite phase hardnesses	H_M, H_F
Boundary conditions	Holders pressure	Anisotropic	Rolling, Transverse

For Table 1-3, as more experiments be conducted and knowledge about this topic advances, additional rows can be added to the table. Engineering processing parameters here refer to the operation parameters in the punching process, which influence fracture mechanisms in punching process, and the output of the punching process is the input condition, affecting the results of hole expansion test. Material parameters, which are mainly determined by microstructures of steels, are attributed to strength, toughness, and ductility. Steels with different material parameters not only showed different mechanical response in both punching and hole expansion processes at macroscale, showed different fracture mechanisms at microscale.

Figure 1-15 is the flow chart of factors influencing the edge fracture.

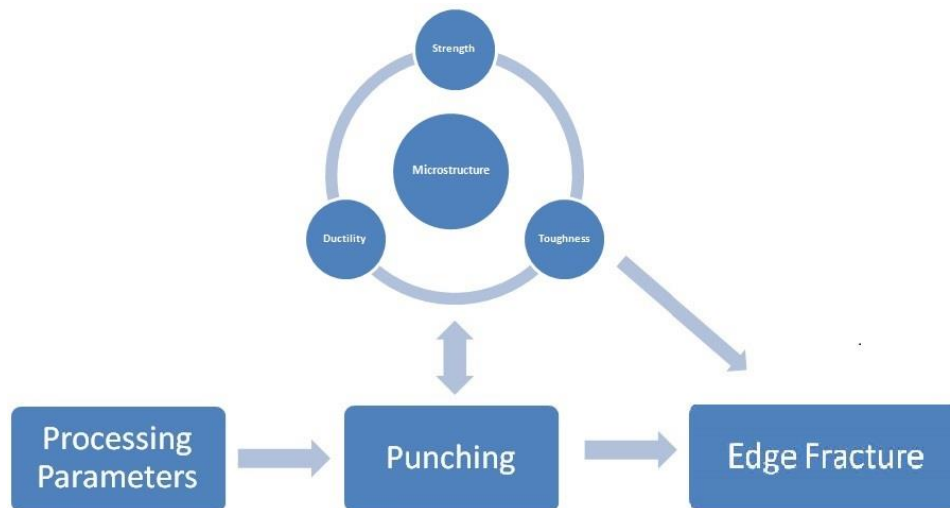


Figure 1-15 The flow chart of the critical factors influencing the edge fracture

It is worth mentioning that the result of hole expansion is controlled by a web of interlocking relationships of parameters listed in Table 1-3 or Figure 1-15, there is no single parameter can be considered as the only cause of the edge fracture phenomenon of AHSS.

1.7 Research objectives and approaches

The objective of this dissertation is to investigate the failure mechanism and develop a predictive method for edge fracture. The object are decomposed into the following three tasks:

1. Investigating effects of processing and material parameters on fractured edges in the punching process.
2. Evaluating the influence of punching process and effects of material parameters on the hole expansion test results.

3. Investigating the effects of microstructures on plasticity and fracture of DP steels.

Research approaches include both experimental and numerical analysis methods, as detailed below:

Experimental analysis methods include tensile test, metallographic analysis, Optical Microscope (OM) observation, Scanning Electron Microscope (SEM) observation, and image analysis.

Uniaxial tensile test is used to evaluate the macro mechanical properties, specifically the strength and ductility of DP steels. Metallographic analysis is applied to reveal the grain structures and "flow lines" within sheared edges of DP steels. Martensite volume ($V_M\%$) fraction and distribution pattern are obtained by analyzing metallographic images photographed by OM. Sheared edges are photographed in radial and tangential directions, to analyze the relative heights of four sheared edges zones and "flow lines", which recorded the deformation history of sheared edges. SEM is applied to photograph morphologies of crack surfaces after hole expansion test, and to investigate fracture mechanisms of DP steels at the microscale level.

The numerical analysis includes Finite Element Method (FEM) and model fitting.

Punching and hole expansion processes are simulated at macroscale level. Simulation results are correlated to experimental results as a guide. By combining experiment and simulation, fracture mechanisms in punching and hole expansion processes are deduced.

An RVE model is built in Abaqus. The RVE model includes the microstructure characters of DP steels, aiming at investigating the microstructures' influence on crack initiation and propagation at mesoscale level. By combining the results from SEM observation and finite element analysis, the effects of microstructures on the edge fracture phenomenon are deduced.

An empirical model is proposed. The model includes processing parameters, mechanical properties, and microstructure parameters of DP steels, with the aim at evaluating the hole expansion test results of DP steels with different grades and from various suppliers.

1.8 Outline of the dissertation

Chapter 1 introduces basic conceptions and research methodologies to investigate the edge fracture phenomenon of DP steels.

Chapter 2 introduces the conceptions of damage mechanics, which is the theory base for investigating and simulating all failure processes in this dissertation.

Chapter 3 focus on the study of hole punching process. This chapter introduces the hole punching process, and investigates the influence of the engineering process parameters on the crack initiation and propagation during the punching process at macroscale.

Chapter 4 focuses on the study of hole expanding process with the emphasis on edge fracture. This chapter introduces the hole expansion process, investigates edge fracture phenomenon in both macro and mesoscales. A microstructure based failure criterion has been proposed and applied to predict the failure of materials that are classified at the same grade but from different suppliers.

Chapter 5 introduces the influence of microstructures on the mechanical properties and fractographies of RVE models at mesoscale.

Chapter 6 are conclusions of this dissertation and suggestions for future work.

CHAPTER 2 LITERATURE REVIEW OF FAILURE HYPOTHESIS

In this chapter focusing on reviewing different failure hypothesis, among reviewed models, damage models are used in simulations in following chapters.

2.1 Basics of failure hypotheses

At early stage of deformation, all materials show certain elastic behavior, as strain increases brittle materials fail without obvious inelastic deformation, while ductile materials show large inelastic deformation before failure. To prevent the failure of structure, it is necessary to set criteria usually based on simple experiments to quantify a material's failure conditions.

Classical fracture and failure criteria, which were built when materials under static loading, present the current strain or stress state in the following forms:

$$f(\sigma_{ij})=0 \text{ or } g(\epsilon_{ij})=0 \quad (2.1)$$

In six-dimensional space of principal stresses, the failure criterion $f(\sigma_{ij})=0$ can be interpreted as a failure surface. The stress state σ_{ij} on the surface $f=0$, indicates failure due to yielding or fracture; the failure criteria for strain is, when strain ϵ_{ij} meet the condition $g=0$ failure occurs.

In the failure criteria (2.1) materials are considered as continuum, the influence of deformation history or defects on the behavior of materials are ignored. These failure criteria are widely used in industry because they are convenient for application and accurate enough to predict the onset of plastic yielding of ductile materials and fracture of brittle materials [18].

For plastically deformable materials, at specific stress states, after reaching the yield point, flow rule are used to describe the relationship between strain-rate and deviatoric stress. However, this kind of statements are often not capable of dealing with large deformation involving ductile fracture [19], because in late stage of ductile fracture process stress will gradually decrease as the increase of strain.

Damage mechanics is an approach to describe ductile fracture involved problems; the material deterioration process is described as the decrease area to resist loading. According to damage mechanics, during the ductile fracture process, voids, or cracks within the structure increase, area to resistance pressure decrease, in this maneuver, the damage affects the behavior of a material.

2.2 Definition of damage at different scales

In damage mechanics, authors of different books classify the research scope into micro, meso, and macro scales or atom, micro, and macro scales.

According to Jean Lemaitre [20], the damage are studied at micro, meso, and macro scales.

At the microscale level, damage is defined as the accumulation of micro stress in the neighborhood of defects or interfaces and the breaking of bonds; at the mesoscale level, damage is the growth and the coalescence of microcracks or microvoids initiation of crack; at the macroscale level, damage is the growth of that crack.

The first two stages can be studied using damage variables of the mechanics of continuous media defined at the mesoscale level. The third stage, a structural failure due to the growth of one or more macro cracks, the geometry (size, shape) and location of cracks are explicitly represented in the fracturing process with variables defined at the macroscale level, it is worth noting that at macro level, fracture mechanics can be applied to research the crack propagation phenomenon.

J. Skrzypek and A. Ganczarski [21] studied at atomic, micro, and macro scales, as discussed in 2.2.1, 2.2.2, and 2.2.3.

2.2.1. Damage at the atomicscale

At the atomicscale, C.W. Woo and D.L. Li [22] proposed a physically consistent definition of material damage. According to this definition, damage is evaluated at the atomicscale by breaking of the interatomic bonds, as listed in Table 2-1.

Table 2-1 Formulas of damage at the atomicscale

Considering the inter-atomic energy, based on the reduction of the inter-atomic energy	Considering the actual configuration of the atomic bonds, depending on the number of broken bonds
$D_1 = \frac{\sum_{i=1}^n [b^i(\Delta G_0^s) - b^i(\Delta G^s)] N}{\sum_{i=1}^n b^i(\Delta G_0^s) N}$ $= 1 - \frac{\sum_{i=1}^n b^i(\Delta G^s) L_b^i N}{\sum_{i=1}^n b^i(\Delta G_0^s) L_b^i N}, \quad (2.2)$	$D_2 = \frac{\sum_{i=1}^n s[b^i(\Delta G^s)] L_b^i N}{\sum_{i=1}^n \Delta G_0^s L_b^i N} \quad (4.3)$ $s[b^i(\Delta G^s)] = \begin{cases} 1, & \text{when } b^i(\Delta G^s) = b^i(0) = 0 \\ 0, & \text{otherwise} \end{cases}, \quad (2.3)$ <p style="text-align: center;">(i = 1, 2, ..., n),</p>

$b^i(\Delta G^s)$: indicates that the intensity of cohesion inter-atom between two atoms is dependent on the energy;

L_b^i : is the characteristic direction vector;

ΔG^s : denotes the single inter-atomic energy;

$b^i(\Delta G^s)$: comparing with $b^i(\Delta G_0^s)$ as a measure of damage;

n : the number of bonds through the plane considered and the selection function;

$L_b^i \cdot N$: the projection of the direction vector of bond along the normal direction of the plane considered, and acted as the variable of orientation of bonds on damage;

$b^i(\Delta G^s)$: the i -th order bond force between two atoms of the direction vector L_b^i of the intensity b^i in terms of the single inter-atomic energy ΔG^s (for broken i -th bond $b^i(0)=0$);

ΔG_0^s : the inter-atomic energy of the undamaged materials.

The influence of the orientation of bonds is included through the scalar product of the unit direction vector L_b^i of i -th bond and the unit normal vector to the plane considered N .

S : a selector factor introduced to distinguish the broken bonds, $s(b^i = 0) = 1$, from the active ones $s = 0$, and n denotes the total number of bonds through the plane considered.

2.2.2. Damage at microscale

a. One-dimensional surface damage parameter

L.M. Kachanov (1958) [23] introduced the continuum parameter ψ to characterize a gradual deterioration process of a microstructure, through micro crack and microvoid nucleation and evolution, the surface area δA of intersection of the plane of normal n with the RVE surrounding a material point:

$$\psi = \frac{\delta \tilde{A}}{\delta A}, \psi \in [0,1], \quad (2.4)$$

$\psi = 1$: corresponding to the initial moment (no damage).

$\psi = 0$: corresponding to the moment of brittle rupture.

$\delta \tilde{A} = \delta A - \delta A_D$: effective (remaining) area.

δA : total undamaged area.

b. Void volume fraction or porosity in ductile materials

According to A. L. Gurson [24], Viggo Tvergaard [25], ductile fracture in polycrystalline metals and porous materials is the result of nucleation, growth, and coalescence of voids and cavities as the increase

of large (visco) plastic deformation. Void volume fraction in an RVE is defined as the ratio of the void volume to the volume of the RVE.

$$f = \frac{\delta V - \delta V_s}{\delta V} \quad (2.5)$$

f : void volume fraction in a RVE.

δV_s : volume of the solid constituents of material element.

δV : volume of the RVE.

2.2.3 Damage at macroscale

On the macroscale, material damage can be evaluated by the nondestructive measurement of the change of physical quantities, such as elasticity modulus, microhardness, acoustic wave speed, etc. A fictive pseudo-undamaged and quasi-continuous body concept allows for homogenization of the physical quantities of a heterogeneous and discontinuous damage solid, such that the effective state variables and the effective physical properties may be defined in terms of the current damage state [20].

Consider a one-dimensional volume element (a bar) of cross-sectional area A with a distribution of micro defects represented by the damaged surface portion A_D , loaded by the applied uniaxial stress σ . This current physical state (\tilde{E}, D) can be mapped to the fictive pseudo-undamaged state $(E, D=0)$ submitted to the effective stress $\tilde{\sigma}$, such that the response remains the same, $\tilde{\varepsilon} = \varepsilon$, hence, when the elasticity equation is furnished for both the damage and the pseudo-undamaged material [20]:

$$\sigma = \tilde{E}\varepsilon, \tilde{\sigma} = E\tilde{\varepsilon} \quad (2.6)$$

Moreover, the effective stress $\tilde{\sigma}$ is defined by the cross-sectional area reduction in the damaged state:

$$\tilde{\sigma} = \frac{F}{A-A_D} = \frac{\sigma}{1-D}, \tilde{\varepsilon} = \varepsilon \quad (2.7)$$

Where $\sigma = F/A$, the following surface damage measure through the effective elasticity modulus drop with the material deterioration holds:

$$D = 1 - \frac{\tilde{E}}{E}, \tilde{E} = E(1 - D) \quad (2.8)$$

Any strain constitutive equation for a damaged material should be derived in the same way as for a virgin material except that effective stress replaces the usual stress.

The classification of scales for damage are relative and not explicit, as our understanding of the deterioration process of material continuously advance, especially in atomic and micro level in material science, the significance of damage (or damage per se) will be richer.

2.3 Yield criteria and damage models

Any yield criterion is a postulated mathematical expression of the states of stress that will induce yielding or the onset of plastic deformation.

2.3.1 Yield criteria

The approach of building a yield criterion is based on the generalization of experimental observations, and mathematical express results in a phenomenological manner.

Von Mises and Tresca criteria

This kind of criteria postulate that yielding will occur when values of the stress components reaches a constant value.

Von Mises	Tresca
$\left[\frac{(\sigma_1 - \sigma_2)^2 + (\sigma_2 - \sigma_3)^2 + (\sigma_3 - \sigma_1)^2}{3} \right]^{1/2} = C$	$\sigma_1 - \sigma_3 = C$
$\sigma_1 > \sigma_2 > \sigma_3$	

Hill yield criterion

This anisotropic yield criterion proposed by Hill in 1948 [26], is still widely used in industrial applications, because it is simple in mathematical and parameters with direct physical meaning.

$$2f(\sigma_{ij}) = H_1(\sigma_{22} - \sigma_{33})^2 + H_2(\sigma_{33} - \sigma_{11})^2 + H_3(\sigma_{11} - \sigma_{22})^2 + 2H_4\sigma_{23}^2 + 2H_5\sigma_{31}^2 + 2H_6\sigma_{12}^2 = 1 \quad (2.9)$$

1, 2, 3: rolling, transverse, and normal directions.

$H_1, H_2, H_3, H_4, H_5, H_6$: material constants.

The identification procedure of this yield criterion uses only four mechanical parameters. As a consequence, it cannot accurately describe the planar distribution of both the uniaxial yield stress and the uniaxial coefficient of plastic anisotropy. In addition, it cannot capture the biaxial yield stress [27]. R. Hill improved the model to generalized Hill yield criterion [28] in 1979 and Hill 1993 yield criterion [29].

Johnson and Cook constitutive model [30]

Johson-Cook is an empirical equation or representative material constitutive model. The strength model of the Von Mises tensile flow stress, σ , is expressed as:

$$\sigma = [A + B\varepsilon^n][1 + C \ln(\dot{\varepsilon}^*)][1 - (T^*)^m] \quad (2.10)$$

$$\dot{\varepsilon} = \sqrt{\frac{2}{9} [(\dot{\varepsilon}_1 - \dot{\varepsilon}_2)^2 + (\dot{\varepsilon}_2 - \dot{\varepsilon}_3)^2 + (\dot{\varepsilon}_3 - \dot{\varepsilon}_1)^2]}.$$

$$\dot{\varepsilon}^* = \dot{\varepsilon} / \dot{\varepsilon}_0, \dot{\varepsilon}_0: \text{plastic strain rate} = 1.0 \text{ s}^{-1}.$$

$$\varepsilon = \sum \dot{\varepsilon} \Delta t: \text{equivalent plastic strain.}$$

$$T^* = \frac{T - T_0}{T_{melt} - T_0}: \text{homologous temperature, } T_0: \text{room temperature.}$$

O, P, Q, R, S: material constants.

2.3.2 Damage models

Generally, to account the damage accumulated in structure there are uncoupled and coupled methods. The uncoupled method takes D as a state variable which independent with plastic strain, in this case damage will not influence the stress during the plastic deformation. So this method didn't attempt to physically describe the process as a gradually weakening phenomena. The onset of fracture is predicted when the damage reached a value, and described as a cut-off (or cliff-like) drop in strain stress curve. The coupled method, damage is coupled with plastic strain and stress, in this case the process from onset of fracture till complete loss of loading carrying capacity, is described as the gradually decrease of stress as the increase of plastic strain. This method try to physically depict the material deterioration phenomena [31].

Johnson and Cook cumulative damage model [30]

In this cumulative damage fracture model, critical parameters, such as stress triaxiality, strain rate, and temperature, are included in the “associated failure function”.

This fracture model attempts to show the relative effect of various parameters and to account for path dependency by accumulating damage as the deformation proceeds. Essentially, it is a weighted integral with respect to the effective strain. The damage to an element is defined as:

$$D = \sum \frac{\Delta \bar{\varepsilon}^{Pl}}{\varepsilon^f}, \text{ or } \int_0^{\varepsilon_c} \frac{d\bar{\varepsilon}^{Pl}}{\varepsilon^f(\sigma^*, \dot{\varepsilon}^*, T^*)} \quad (2.11)$$

$$\varepsilon^f = \left\{ \begin{array}{ll} [D_3 + D_4 \exp(D_5 \sigma^*)][1 + D_6 \ln \dot{\varepsilon}^*][1 + D_7 T^*] & \text{for } \sigma^* \leq 1.5 \\ (\varepsilon_{\sigma^*=1.5}^f - \varepsilon_{\min}^f) / (\sigma_{\text{spall}}^* - 1.5) & \text{for } 1.5 < \sigma^* < \sigma_{\text{spall}}^* \\ \varepsilon_{\min}^f & \text{for } \sigma^* \geq \sigma_{\text{spall}}^* \end{array} \right\} \quad (2.12)$$

$\Delta \bar{\varepsilon}^{\text{pl}}$: the increment of equivalent plastic strain which occurs during an integration cycle.

ε^f : equivalent strain to fracture, under the current conditions of strain rate, temperature, pressure, equivalent stress.

$\dot{\varepsilon}^* = \dot{\varepsilon}^{\text{pl}} / \dot{\varepsilon}_0$: non-dimensional plastic strain rate; $\dot{\varepsilon}^{\text{pl}}$ is equivalent plastic strain rate, $\dot{\varepsilon}_0$ is reference strain rate.

$\sigma^* = \sigma_m / \sigma_{\text{eq}}$: dimensionless pressure-stress ratio or stress triaxiality-pressure dependence.

$\sigma_m = (\sigma_1 + \sigma_2 + \sigma_3) / 3$: the average of the three normal stresses.

σ_{eq} : Von Mises equivalent stress.

For $\sigma^* \leq 1.5$. Fracture is the allowed to occur when $D=1.0$.

D_3, D_4, D_5, D_6 , and D_7 : material constants or failure parameters.

T^* is the non-dimensional temperature, which is defined as:

$$T^* \equiv \left\{ \begin{array}{ll} 0 & \text{for } T < T_{\text{transition}} \\ (T - T_{\text{transition}}) / (T_{\text{melt}} - T_{\text{transition}}) & \text{for } T_{\text{transition}} \leq T \leq T_{\text{melt}} \\ 1 & \text{for } T > T_{\text{melt}} \end{array} \right\} \quad (2.13)$$

T, T_{melt} , and $T_{\text{transition}}$: current temperature, melting temperature, and transition temperature. The material parameters must be measured at or below the transition temperature.

In Abaqus/ Explicit [32], the expression differs from the original formula published by Johnson and Cook in the sign of D_3 , which a negative sign is added before the coefficient. This difference is motivated by the fact that most material experience a decrease in ε^f with the increasing stress triaxiality, therefore, in the above expression D_3 will usually take positive value.

Wilkins, Streit, and Reaugh cumulative damage model [33]

M.L. Wilkins, R.D. Streit, and J.E. Reaugh proposed a cumulative strain damage criterion to predict the initiation and propagation of fracture in ductile materials. Fracture begins when the damage exceeds a critical value over a critical distance and proceeds as the critical damage state is reached elsewhere. The cumulative damage parameter D is defined as:

$$D = \int w_1 w_2 d\bar{\varepsilon}^{\text{pl}} \quad (2.14)$$

$\bar{\epsilon}^P$: equivalent plastic strain.

$w_1 = \frac{1}{(1+ap)^\alpha}$: hydrostatic-pressure weighting term, P is the hydrostatic pressure, a , α are material constants.

$w_2 = (2 - A)^\beta$: asymmetric strain weighting term, β is material constant.

$A = \max \left\{ \frac{s_2}{s_1}, \frac{s_2}{s_3} \right\}$, s_1 , s_2 and s_3 are the principle stress deviators.

The parameter, A , ranges from 0 to 1; the stress is called field symmetric when $A=1$ and asymmetric when $A=0$. These limits correspond to the loading conditions for the simple tension test and the torsion test respectively.

Gurson, Tvergaard, and Needleman (GTN) damage model

GTN model adopts mechanistic approach, which derives theories from elements of fracture at the microscopic scale. The model first propose by Gurson in 1977 [24], modified by Tvergaard [25] and Needleman [34].

Gurson proposed the approximate yield criteria and flow rules for porous (dilatant) ductile materials, showing the role of hydrostatic stress in plastic yield and void growth, obtained the pressure dependent yield function for an isolated cylindrical or spherical void in a continuum [24]. In the paper, it states that, void nucleation and growth (and thus bulk dilatancy) are commonly observed in some processes which are characterized by large local plastic flow, such as ductile fracture. The void-containing solid is considered as a dilatation, pressure-sensitive elasto-plastic continuum. The macroscopic strength of material depends on the matrix strength, the void volume fraction and the applied hydrostatic tension. The yield function for spherical void in rigid-perfectly plastic body is:

$$\Phi = \left(\frac{\sigma_{eq}}{\sigma_{yield}} \right)^2 + 2f \cosh \left(\frac{3\sigma_m}{2\sigma_{yield}} \right) - [1 + f^2] = 0 \quad (2.15)$$

σ_{eq} : equivalent stress or Von Mises stress.

σ_M : material yield stress or matrix strength.

σ_m : average stress or hydrostatic stress.

f : void volume.

In 1981, Tvergaard [25] proposed modifying the yield condition, the void volume change rate was introduced into the original model:

$$\Phi = \left(\frac{\sigma_{eq}}{\sigma_{yield}}\right)^2 + 2q_1 f \cosh\left(\frac{3q_2 \sigma_m}{2\sigma_{yield}}\right) - [1 + q_3 f^2] = 0 \quad (2.16)$$

q_1 , q_2 , and q_3 : material constants.

And the void volume change rate were defined as:

$$\dot{f} = \dot{f}_{nucleation} + \dot{f}_{growth} \quad (2.17)$$

The nucleation of voids is controlled by strain or stress as listed in Table 2-2:

Table 2-2 Strain and stress controlled voids nucleation law

Strain-controlled	Stress-controlled
$\dot{f}_{nucleation} = \frac{f_N^n}{S_N^n \sqrt{2\pi}} \exp\left[-\frac{1}{2} \left(\frac{\bar{\epsilon} - \epsilon_N}{S_N^n}\right)^2\right]$ (2.18)	$\dot{f}_{nucleation} = \frac{f_N^s}{S_N^s \sqrt{2\pi}} \exp\left\{-\frac{1}{2} \left[\frac{(\bar{\sigma} + \sigma_m) - \sigma_N}{S_N^s}\right]^2\right\}$ (2.19)
f_N^n, f_N^s : volume fractions of void nucleating particles (n: strain-controlled, s: stress-controlled); S_N^n, S_N^s : standard deviations; ϵ_N, σ_N : mean nucleating strain and mean nucleating stress.	

The growth of existing voids is based on the law of conservation of mass:

$$\dot{f}_{growth} = (1 - f) \dot{\epsilon}_{kk}^p \quad (2.20)$$

In 1984, Tvergaard and Needleman [34] introduced the void coalescence and fracture criteria into the model:

$$\Phi = \left(\frac{\sigma_{eq}}{\sigma_{yield}}\right)^2 + 2q_1 f^* \cosh\left(\frac{3q_2 \sigma_m}{2\sigma_{yield}}\right) - [1 + (q_1 f^*)^2] = 0 \quad (2.21)$$

The definition of the evolution process of void become more rich, as when f reaches a value, the coalescence process will start, material will gradually loss stress carry capacity as the increase of f :

$$f^*(f) = \begin{cases} f & \text{for } f \leq f_c \\ f_c + \frac{1/q_1 - f_c}{f_f - f_c} (f - f_c) & \text{for } f_c < f \leq f_f \end{cases} \quad (2.22)$$

f_c : critical void fraction.

f_f : void volume fraction at fracture.

The void coalescence is considered to take place when the void volume fraction researches a critical value f_c and the material fractures when the void volume fraction reaches f_f .

However, there are limitations when applying Gurson model. Firstly, because no term about stress triaxiality in the evolution process (void volume change) in the model, so in pure shear condition, in which

materials show the lowest ductility, the growth rate of voids is zero due to constant fracture void fraction, so according to the model material will not fail, which is obviously not true. To address this problem, Xue [31] by introducing the void shearing mechanism to incorporate the effect of Lode angle into Gurson model. Secondly, the theoretical work by Gurson shows such dependence in the positive range of mean stresses. It can't be used in case of compression. Thirdly, the Gurson model does not include terms to describe the strain hardening phenomenon.

CHAPTER 3 HOLE PUNCHING PROCESS

Figure 3-1, in punching process a tool punches through the metal sheet, removes unwanted material, and creates a hole (or other desired geometry feature). During punching process, material fractures within the clearance (space between die and tool) zone, creates sheared edge, which includes 4 zones (rollover, burnish, fracture and burr zones) in the thickness direction of metal sheet, see Figure 3-1 circled area.

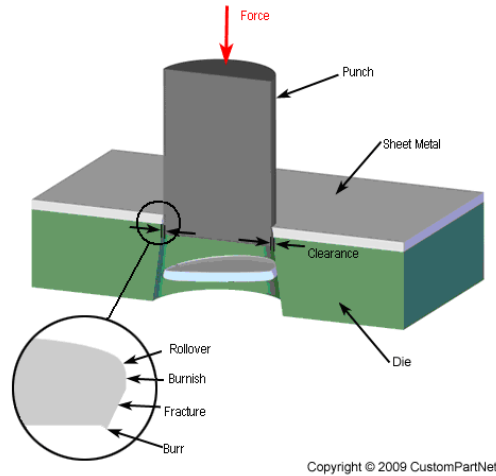


Figure 3-1 Hole punching process [35]

For the punching process, parameters affecting the surface morphologies of the sheared edges are listed in Table 3-1. For the sheared edges, higher stretchability in the hole expansion test is considered to have a better “quality”.

Table 3-1 Investigated parameters for punching process

Engineering Process parameters		Material parameters	
Hole diameters (d_0)	20, 40, 60, 80	Ultimate strength (UTS)	780, 980
Clearances (C%)	10%, 20%, 30%	Anisotropic	Rolling (RD), Transverse (TD)

This chapter mainly focus on researching the effects of clearances, thicknesses, hole diameters, and material properties, on morphologies of sheared edges.

It is worth mentioning, in practice, the punch tool wear out state also influence the hole expansion test results. Upon observing experiment results, it was found that in some cases when the tools for punching were worn out, after the process, some through-thickness scratch-like notches were observed with the naked eye on the sheared surfaces. The notch (process introduced defects) damages the integrity of the

sheared edge, and creates stress concentration site, resulting in significant lower stretchability in hole expanding test.

3.1 Literature review of shearing fracture dominant processes

Researching the fracture mechanism of metal sheet in the area of interest (AOI) will not only benefit to punching process but also to other forming processes similar to punching, such as blanking, trimming, cropping, and shearing, for those processes are different in fabrication equipment or only in technical terms, essentially are similar in fracture mechanism. For these listed shear fracture dominant processes, geometry and quality of sheared edge after processing are of interest.

Chang and Swift [36] researched stresses, metal flow, and crack propagation in shearing of thick bars of lead, tin, aluminum, copper, brass, and mild steel, with clearance ranging from 0% to 30%; found two modes of fracture under zero clearance condition; made an attempt to correlate the stresses in shearing and tensile tests. Golovashchenko and Ilinich [37] studied the mechanisms of burr generation and their influence on AHSS formability in stretch flanging; part cross-section of sheared surface (or fractured edge profile) of samples trimmed by conventional trimming process and robust trimming process, with clearance ranging from 10% to 40%, were presented and compared. Huang et al. [38, 39] investigated processing and testing variations; and tried to standardize the new testing tools, setups, and procedure for AHSS. Shih and Hsiung [40, 41] by using optimal production trimming process improved 60% TE (or stretchability) of AHSS; recommended 15% die-tool clearance for trimming AHSS sheets.

To estimate the force in punching-like processes, Atkins [42] analyzed the maximum punching force caused by plastic instability; the initiation, propagation of cracks after the onset of plastic flow; proposed a shear plane model. Based on Atkins's model and by assuming the ratio of normal stress to shear stress applied on a shear band is constant, Zhou and Wierzbiki [43] developed an tension zone model to predict the plastic resistance and the plastic work in blanking or tearing of ductile metal plates. From the viewpoint of industry application, estimating the maximum punching force will benefit to the choosing of proper tool for optimal serving life.

To measure the failure strain in punching process. Stegeman et al. [44] developed a digital image correlation technique to analyze the displacement and strain fields of 13% Cr Steel in blanking process. Hu et al. [45] through measuring grain aspect ratio near the fracture surface to estimate damage parameters

for simulation for AA6111-T4 aluminum sheets in trimming process. Wu et al. [46] measured strain distribution of sheared edge of DP600, 780 and 980 of punching process, with clearance from 0 to 10%, by processing images of "flow lines", which compose by martensite particles. Estimating the shear failure strain will benefit to the quantitatively analysis of sheared edge.

3.2 Observing sheared edge from normal and tangential directions

To analyze the fracture edges after punching process, fractured edges is photographed in 2 directions, as shown in Figure 3-2 (b). Observing direction 1 is denoted by OD1, Figure 3-2 (a), is fractured edge observed in normal direction (OD1); observing direction 2 is denoted by OD2, Figure 3-2 (c), is observing fracture edge in tangential (azimuth) direction. RD and TD denotes rolling and transverse directions, respectively.

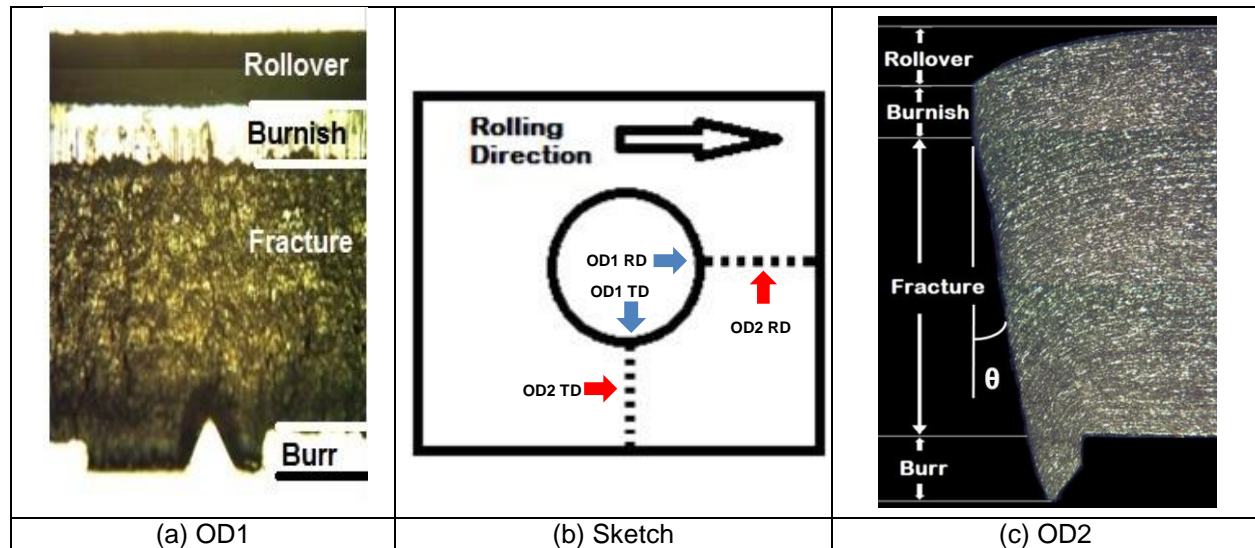


Figure 3-2 Observation Direction (OD) 1 and 2

Observing the fractured edge in OD1, as shown in Figure 3-2 (a), the shining band is burnish zone, above it is the rollover zone, below it is the fracture and burr zones. In order to distinguish burr zone and fracture zone, an inverted "V" shape notch was made with a filer to reach the surface, so that the depth of the notch equals to the height of the burr zone.

Observing the fractured edge in OD2, as shown in Figure 3-2 (c), from top to bottom: 1. The rollover zone is denoted by the height of the curve at the top of the sheet metal; 2. The burnish zone is denoted by the height of the following straight line; 3. fracture zone denotes the height of the section after the burnish

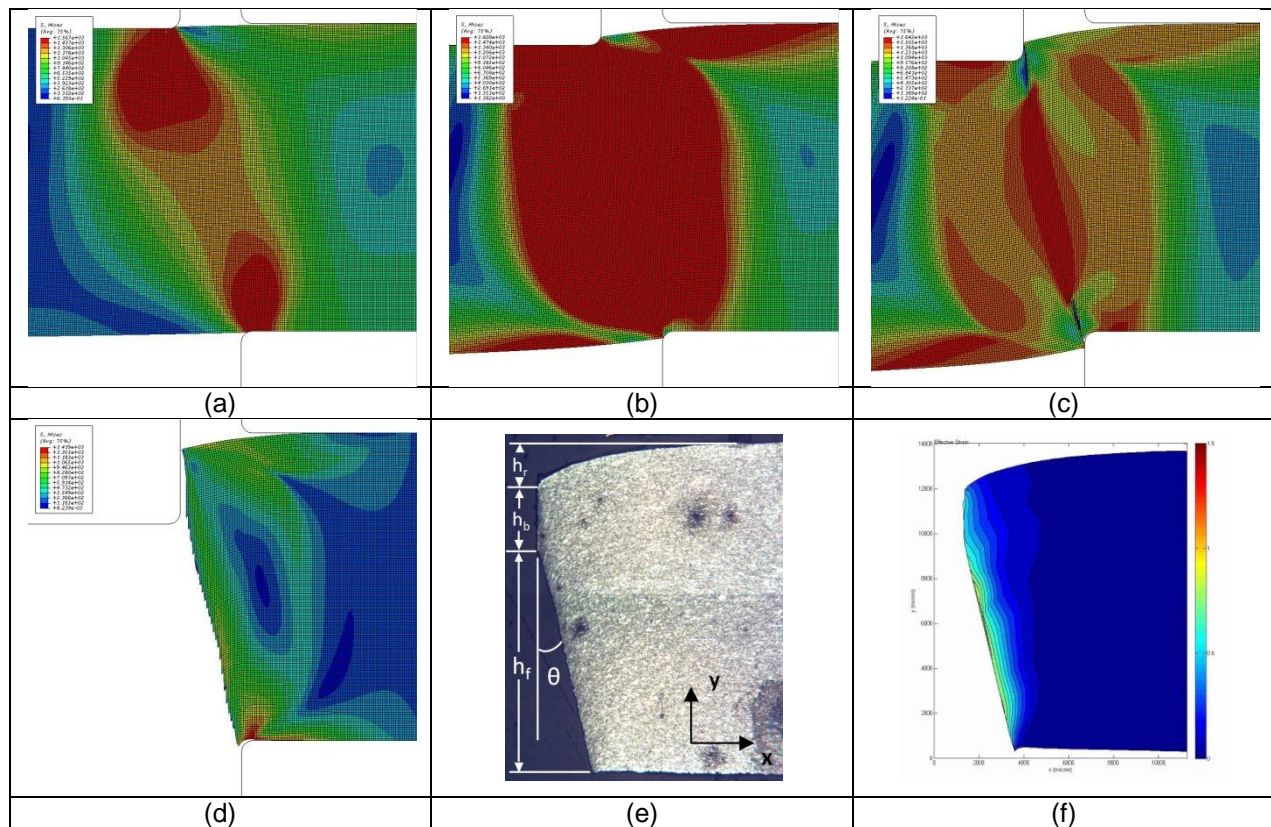
zone, which deflects from the vertical direction; The deflection inclined angle of the fracture zone is denoted by θ ; 4. burr zone denotes the height of burr which below the lower side of sheet metal.

3.3 The effects of investigated parameters on morphologies of sheared edges

In order to observe the sheared edge in tangential direction, OD2, as shown in Figure 3-2 (c), samples were first cut according to the steps in Appendix B and then were mounted in epoxy holders with target position and orientation properly placed (as shown in Appendix B (h)). After polishing and etching the metal "flow lines" are revealed and observable using optical microscope. These flow lines provide the information of strain distribution in the edge deformation zone.

Table 3-2 (a) to (d) are simulated crack initiation and propagation in punching process, combining observed images of sheared edge, Table 3-2 (e), material failure process in punching process can be deduced. Table 3-2 (f) is strain distribution within the sheared edge, by processing image in Table 3-2 (e). For details of punching process simulation, please reference section 3.4.2 of this dissertation.

Table 3-2 DP780 (simulated) sheared edge formation process, experimental observation, and "flow-line" analysis



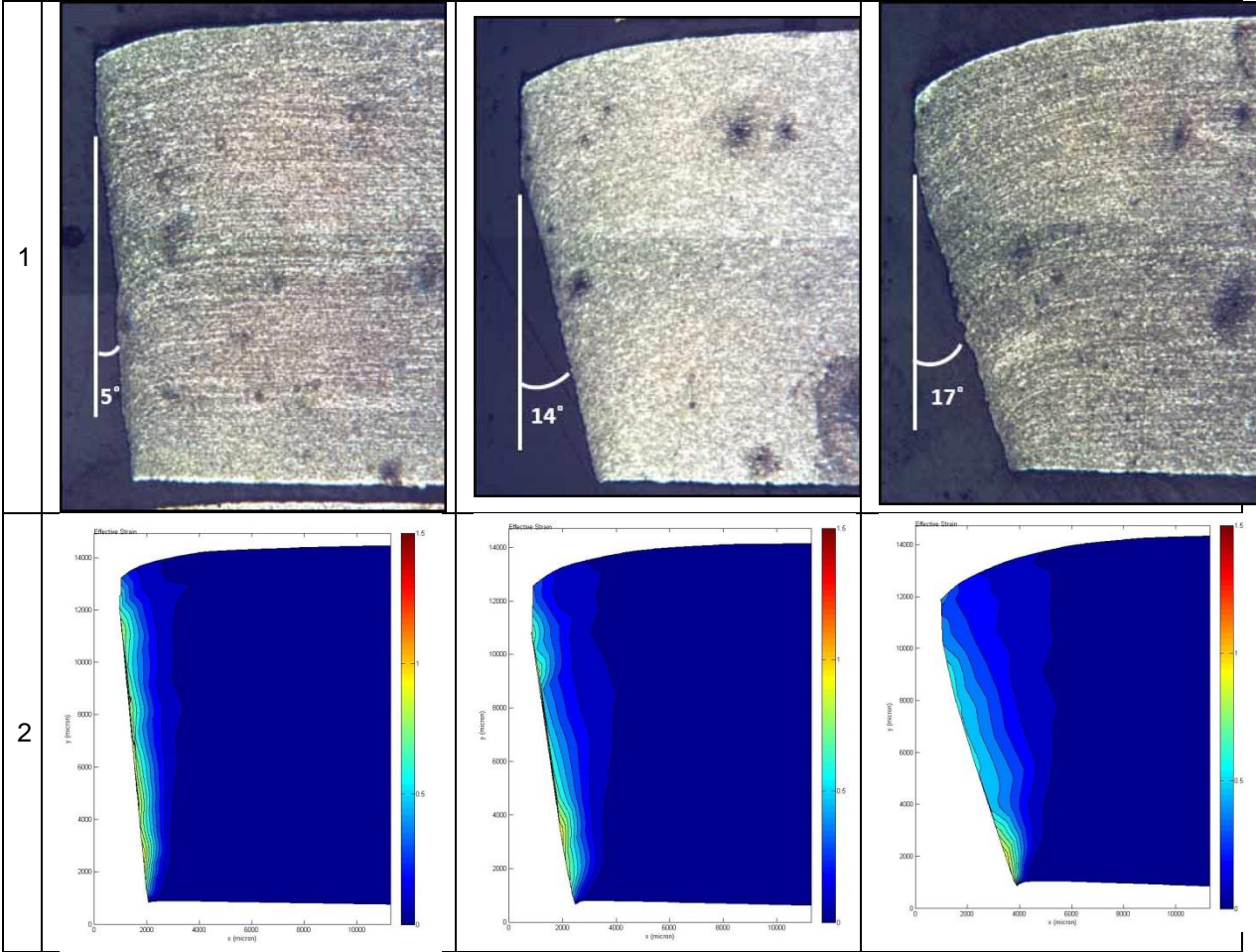
Through simulation the crack initiation and propagation process in punching process, as shown in Table 3-2 (a) to (d), the formation of rollover, burnish, and fracture zones are deduced: 1. rollover zone is created by the yield of the material after tool exerting pressure on the sheet metal but before the initiation of macro crack; 2. burnish zone is created by the friction between the sheet metal and the tool after the initiation of shear fraction; 3. fracture zone is created by the instable crack propagation of the material, and the fractured surface has no contact with the punch (in contrast to the burnish zone), within the clearance between punch and die; 4. burr zone in Table 3-2 (e) is not as obvious as in Figure 3-2 (c), is create by material flow within the clearance zone but out of the plan of the metal sheet, its height is irregular.

3.3.1 Effect of clearance

In Table 3-3, DP780 samples were punched with 10%, 20%, and 30% clearances, by comparing images of samples punched with different clearance, the differences in morphologies can be observed. "Flow lines" within sheared edge are composed by martensite particles, before punching process, martensite particles were aligned in straight lines along the rolling direction, after punching process, as the joint effect of deformation and fracture, original straight lines were bended and ended up with irregular curves, which looks like "flow lines" of fluid. "Flow lines" record the deformation history of the metal in area of interest (AOI) during punching process. Through image processing of flow lines, strain distribution within the sheared edge is revealed, and the differences in strain distribution patterns provides an approach to research the fracture process.

Table 3-3 Analysis of sheared edge images of DP780 with C%=10%, 20%, and 30% (observed in OD2)

	10%	20%	30%



In Table 3-3, following trends are observed:

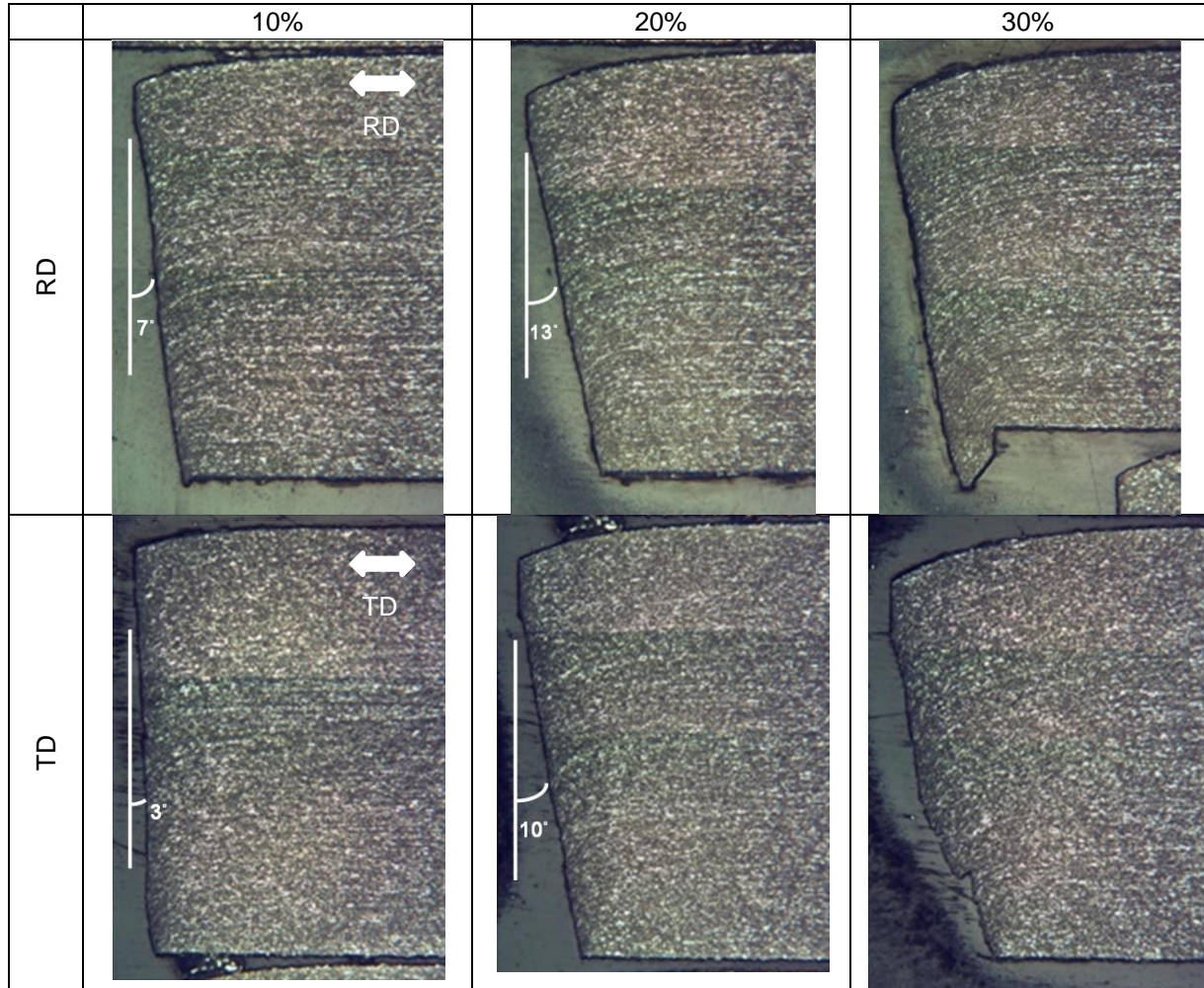
1. From left to right, as the clearance increases, the inclined angle of fracture zone, θ , increases; the area of “shear-affected zone” increases.

2. From top to bottom of each sheared edge, the “shear-affected zone” is shrinking in its width, which implies the gradient of strain increases.

3.3.2 Effect of material anisotropic

In Table 3-4, two group samples observed from different material processing directions are compared. The first row shows sheared edges observed from rolling direction (RD), which is the direction steel have been rolled to sheet; second row are sheared edges observed from transverse direction (TD), which is perpendicular to the rolling direction in the same plane. For more sheared edge images of DP 980 (observed in OD2), please reference Appendix D.

Table 3-4 Sheared edge images of DP 980 GA (1.4) 20 with different orientations and C%
(observed in OD2)



In Table 3-4, following phenomena are observed:

For 10% and 20% clearances (column 1 and 2), the inclined angle of sheared edge outlines for observing from rolling direction is larger than that from transverse direction.

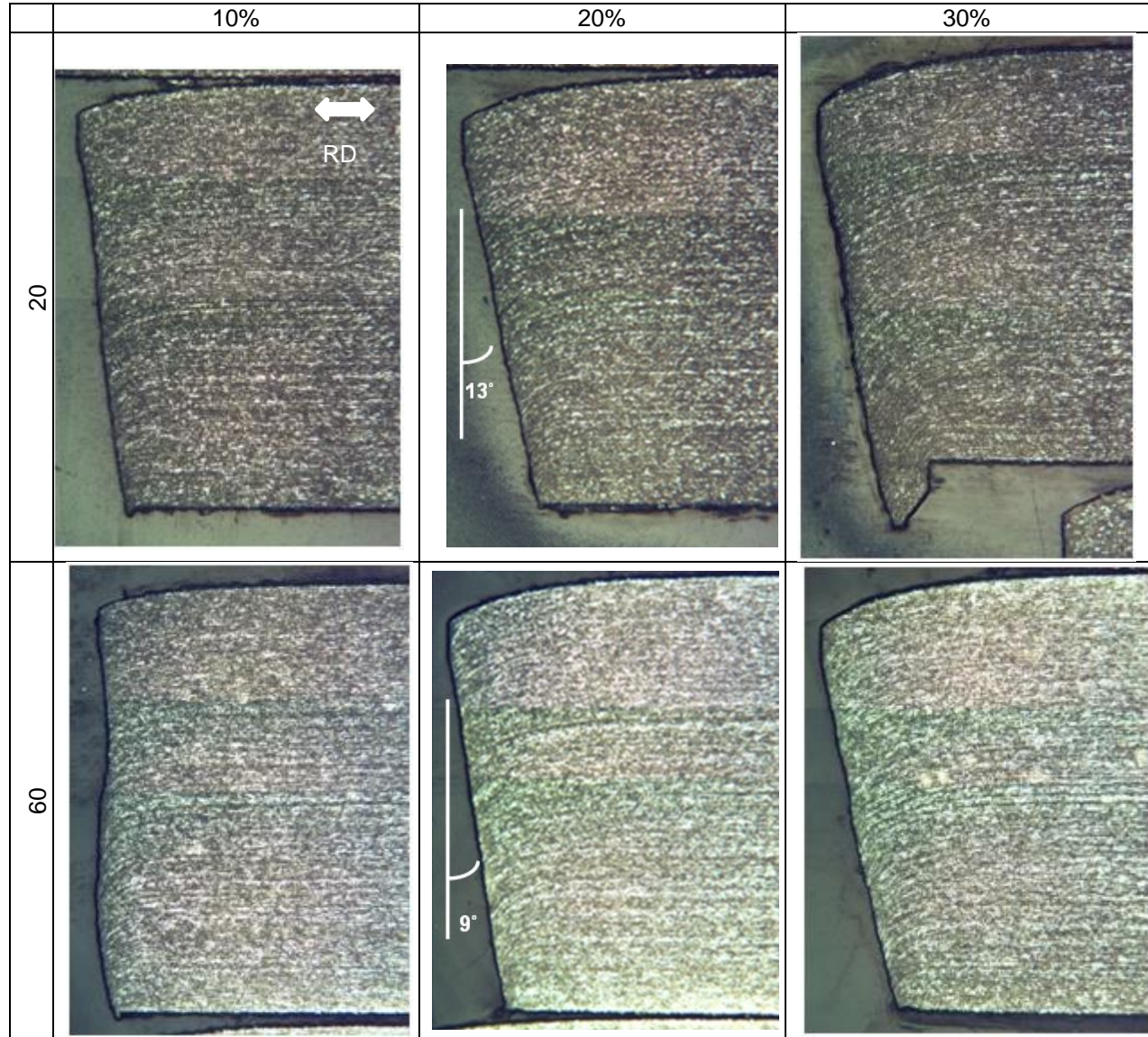
For 30% clearance (column 3), observing the sheared edge outline from rolling direction, very large burr is formed.

By comparing the inclined angle of fracture zone outlines in column 1 and 2, it can be observed, material showed different sheared edge outline characters, which can be attributed to the different properties of researched steels in rolling and transverse directions.

3.3.3 Effect of initial hole diameter

In Table 3-5, two group samples with same material, but different in (initial or original) diameters of punched holes ($d_o = 20$ and 60 mm):

Table 3-5 Sheared edge images of DP980 GA (1.4) RD with different d_o (observed in OD2)



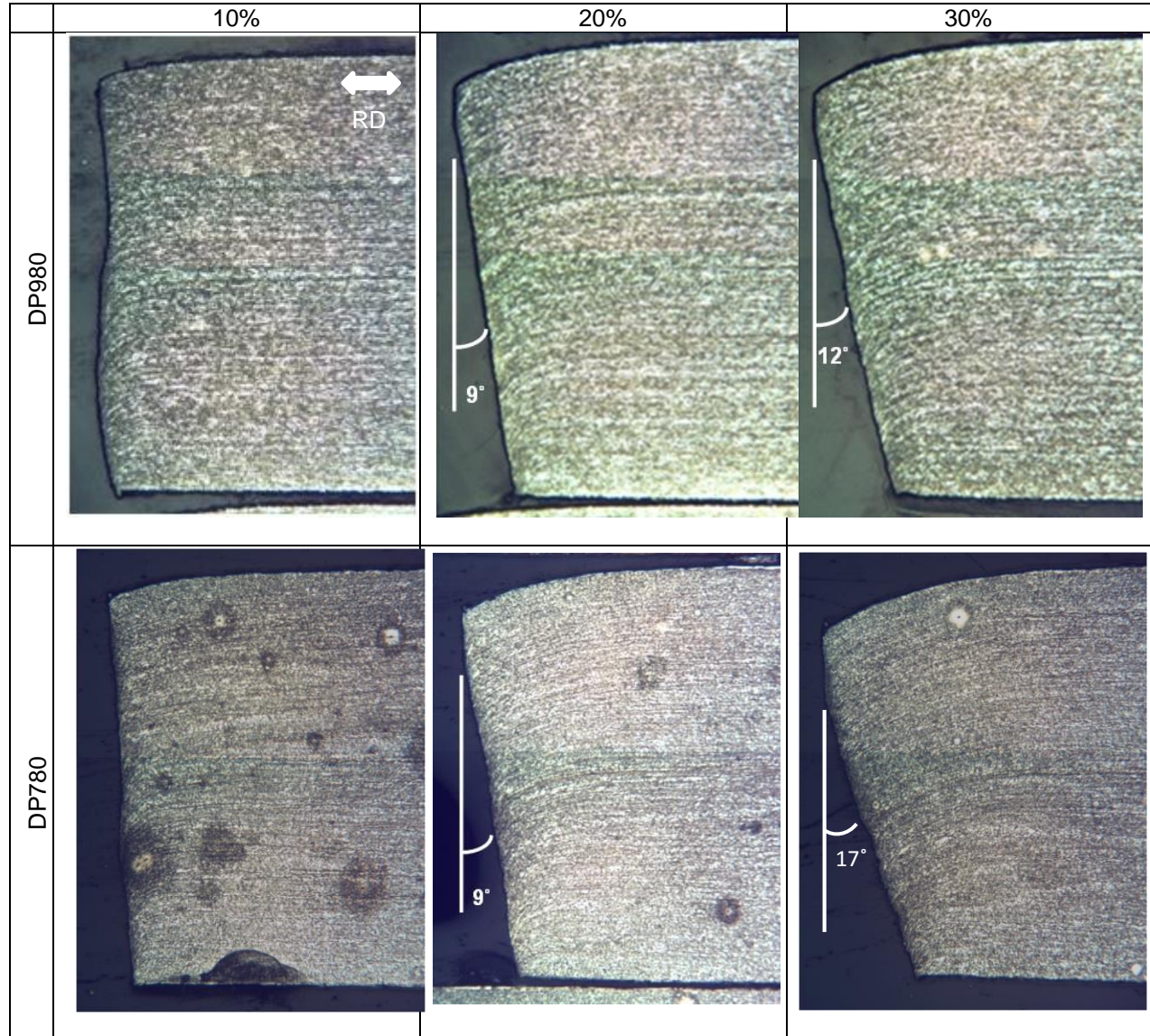
In Table 3-5, following phenomena are observed:

1. For 10% clearance, the fracture zone outline of the sample with 60 mm diameter is a curve, while for the sample with 20 mm diameter the outline of fracture zone is more close to a straight line.
2. For 30% clearance, sample with 60 mm diameter shows no obvious burr, while sample with 20 mm diameter has obvious burr.

3.3.4 Effect of steel grade

In Table 3-6, two groups sample with same initial hole diameters ($d_o=60$ mm) and direction (Rolling), but different steel grades, DP980 and DP780.

Table 3-6 Sheared edge images of DP980 GA 1.4 and DP780 CR 1.0, 60, RD (observed in OD2)



In Table 3-6, following phenomena are observed:

1. For 10% clearance condition, first column, the fracture zone outlines of both samples are curved, but their radiuses of curvature are different.

2. For 30% clearance condition, third column, by observing inclined angle of fracture zone outlines, DP780 sample shows larger inclined angle compare with DP980 sample.

3.4 Relative heights of rollover, burnish, and fracture zones

Using optical microscope to observe Rolling (R) and Transverse (T) directions in normal direction (OD1) of a sample, the morphology of the sheared edge can be observed.

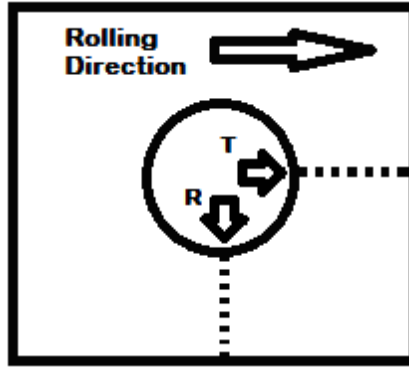


Figure 3-3 Sheared edge observation direction 1 (OD1), Rolling (R) and Transverse (T) directions

In Table 3-7, for an image, the shining band is burnish zone, wave-like patterns are observed; above the burnish zone is the rollover zone, below it is the fracture zone and burr zone, the height of "V" shaped notch equal to the height of burr zone.

Table 3-7 Sheared edge images of DP780 and DP980 with different C% (observed in OD1)

	(a) 10%	(b) 20%	(c) 30%
DP980			
DP780			

Table 3-7, are images of OD1 observation results of sheared edges of DP780 and DP980 steels, it can be observed, as the increase of clearance the height of rollover zone increases. In order to quantitatively analyze fracture edges, imaging processing method applied to measure rollover, burnish, fracture, and burr zones' relative heights.

Figure 3-4, the 4 zones were painted with different colors, in which red represents the rollover zone, green represents the burnish zone, blue represents the fracture zone, black represents the burr zone. Through image processing method averaged height of each zone is measured.

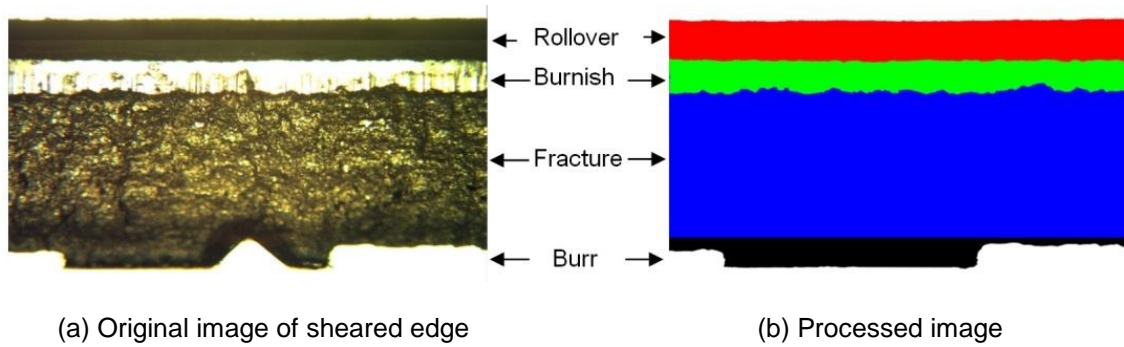


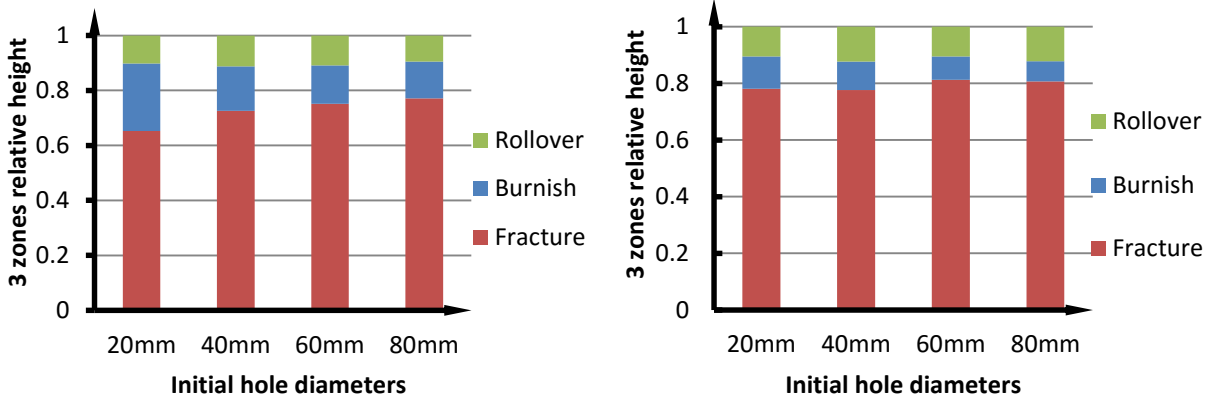
Figure 3-4 Original and processed images for four zones of sheared edge (observed in OD1)

Because the absolute value of height of each zone may significantly be influenced by the focus of optical microscope, the following formula were used to obtain relative height of each zone:

Relative height= measured average height /total height (rollover + burnish + fracture)

$$\text{Relative height} = (h_r, h_b, \text{ or } h_f) / (h_r + h_b + h_f) \quad (3.1)$$

Mechanism of formation of burr zone is complex and its height changed without obvious trend, so the height of burr zone was not in data for analyzing. For convenient, relative height of rollover zone, or h_r/h_0 , is denoted by RRH; relative height of burnish zone, or h_b/h_0 , is denoted by RBH; relative height of fracture zone, or h_f/h_0 , is denoted by RFH.



(a) DP780 EG 20% RD 3 zones relative heights (b) DP980 GA 20% RD 3 zones relative heights

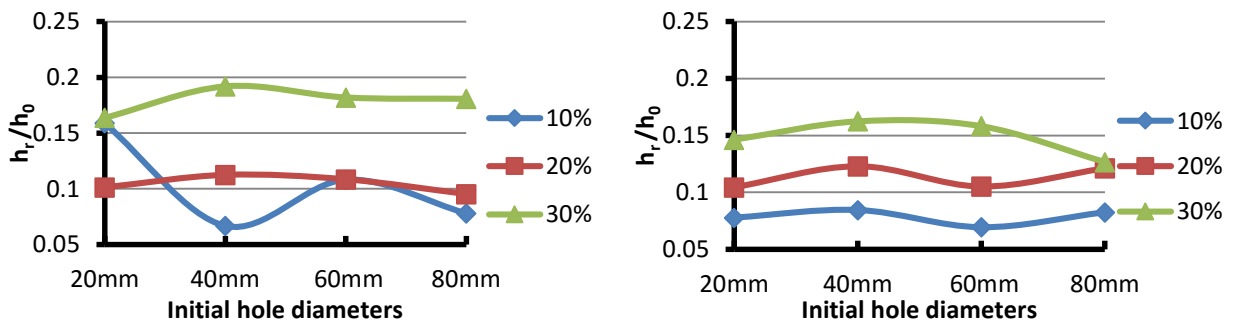
Figure 3-5 Analysis of relative heights for rollover, burnish, and fracture zones of sheared edge

Figure 3-5, are measured 3 zones' height data with respect to d_o . Through this kind of analysis the trend of the 3 zones' height with respect to different parameters are presented. For raw data please reference Appendix C.

Section 3.4.1, 3.4.2, and 3.4.3 are detailed analysis of rollover, burnish, and fracture zones' height change versus to parameters such as clearance (C%), ultimate tensile strength (UTS), initial hole diameter (d_o), and orientation (RD, TD).

3.4.1 Rollover zone relative height (RRH)

In Figure 3-6 and Figure 3-7 measured rollover zone relative height (RRH or h_r/h_o) of DP780 and DP980 are presented versus to punched (initial) hole diameter, d_o , and clearance, C%.



(a) DP780 EG 1.4 RD

(b) DP980 GA 1.4 RD

Figure 3-6 RRH with respect to d_o , with different C%, for DP780 and DP980

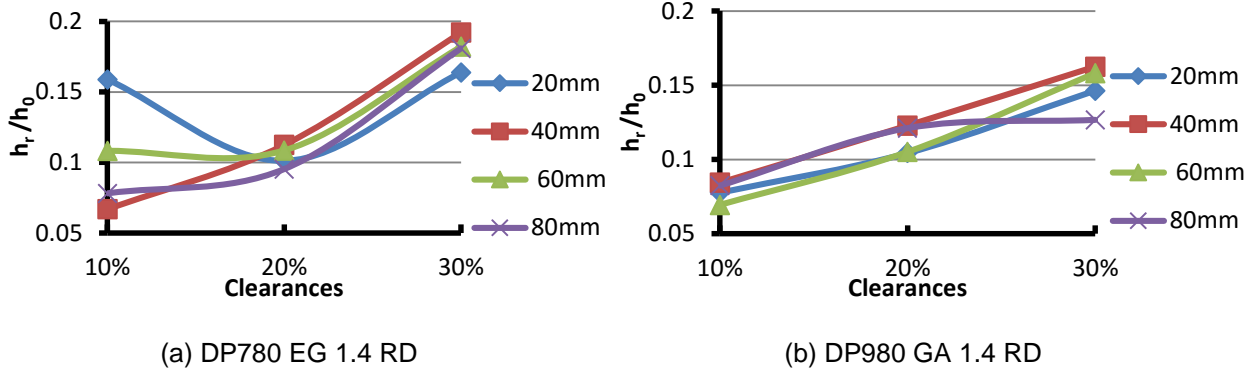


Figure 3-7 RRH with respect to C%, with different d_o , for DP780 and DP980

Figure 3-7, with the increase of clearance (C%), value of RRH increases, which implies the strain at fracture initiation increases. The same trend also showed Table 3-3 row 1, combine images observed in OD1 and OD2, it can be concluded that, as the clearance increases, the deflection of upper boundary of the sheet metal increases.

In Figure 3-8, measured rollover zone relative height of DP780 and DP980 are presented versus to ultimate tensile strength (UTS).

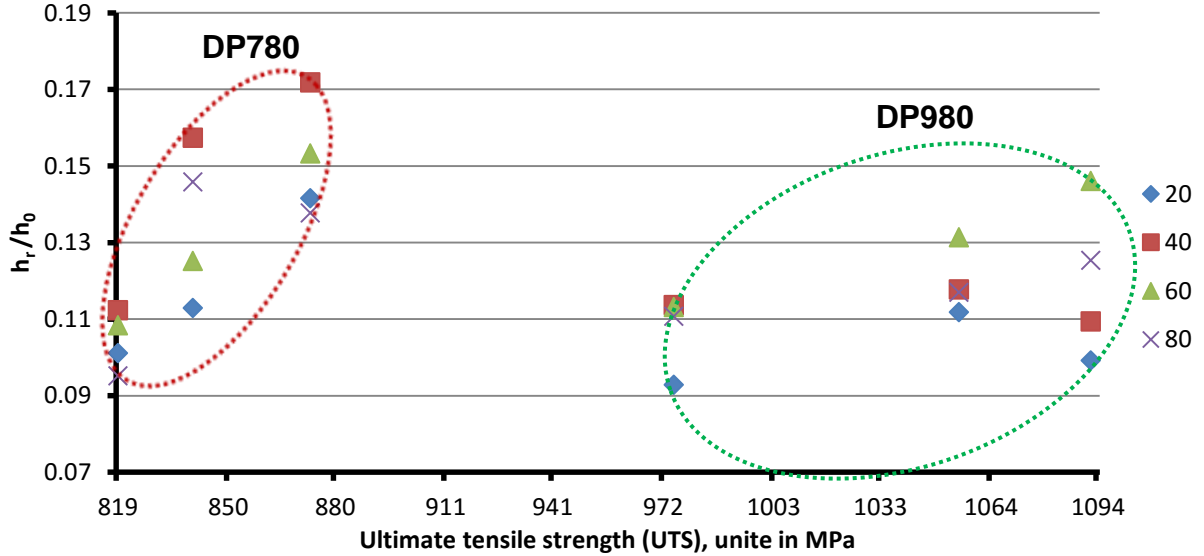


Figure 3-8 RRH with respect to UTS, with C%= 20% RD different d_o

Figure 3-8, from left to right, the first 3 data points are DP 780 steels with different thickness (1.4, 1.8, and 1.0 mm) (see Figure 1-5 and Figure 1-6 for corresponding tensile stress-strain curves in tensile test), their TE are 16.7%, 15.9%, and 14.6%; the last 3 data for DP 980 steels with thickness equal to 1.4 mm,

1.4 mm, and 1.8 mm, TE are 13.3%, 11.3%, and 13.7%; with the premise of same clearance (C%=20%) and observed in Rolling Direction (RD).

In Appendix C, by observing plots of other cases with different C% (10%, 20%, 30%) and different orientation (RD, TD), trend of h_r/h_0 as the increase of UTS can be observed.

It is known that, DP steels with higher UTS is lower in TE in tensile test, it is logical to deduce that the initiation of crack in DP980s should be earlier than DP 780s, which showed rollover zone height of DP980 are less than DP780, is because of relative lower TE in tensile test.

3.4.2 Burnish zone relative height (RBH)

In Figure 3-9 and Figure 3-10, the measured burnish zone relative height (RBH or h_b/h_0) of DP780 and DP980 are presented to with respect to d_0 and C%.

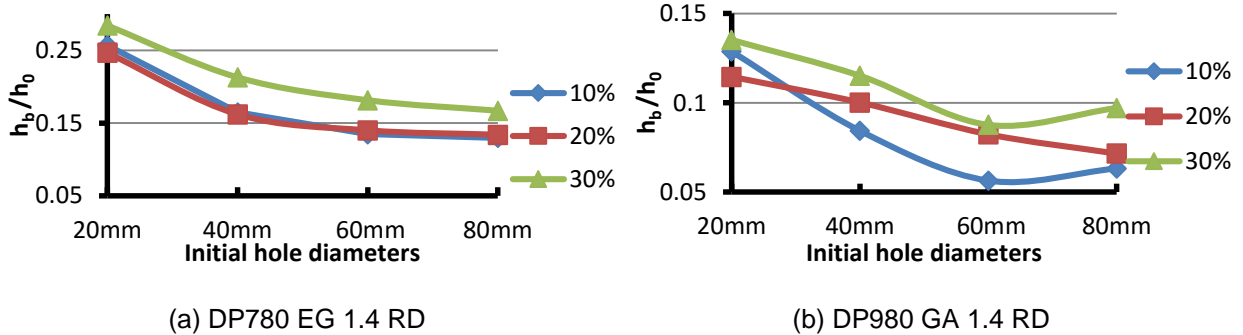


Figure 3-9 RBH with respect to d_0 , with different C%, for DP780 and DP980

In Figure 3-9, with the increase of d_0 , h_b/h_0 will decrease. This is because, the smaller the d_0 is, the elastic recovery (contract effect) is more significant.

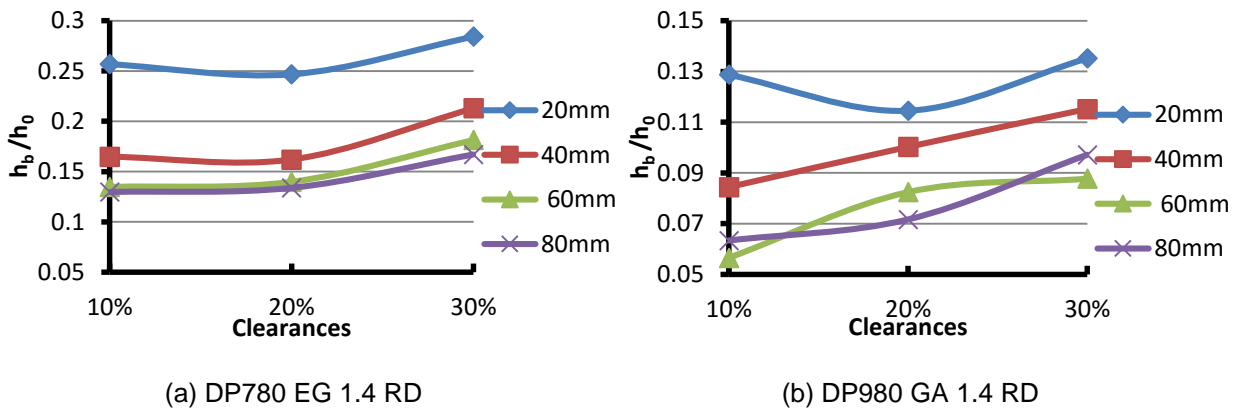


Figure 3-10 RBH with respect to C%, with different d_0 , for DP780 and DP980

Figure 3-10, the overall trend of relative height of burnish zone height (h_b/h_0) is not very obvious, the only trend can be observed is that comparing with C%=10%, 20% when C%=30% RBH are higher.

In Figure 3-11, measured burnish zone relative height of DP780 and DP980 are presented versus to ultimate tensile strength (UTS).

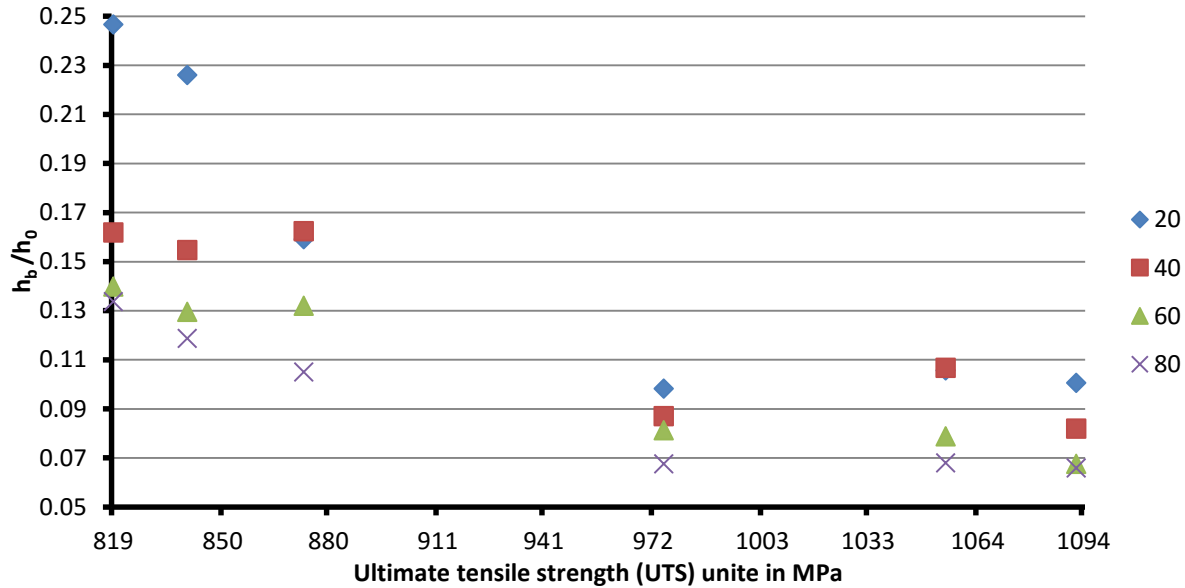


Figure 3-11 RBH with respect to UTS, with C%= 20% RD different d_0

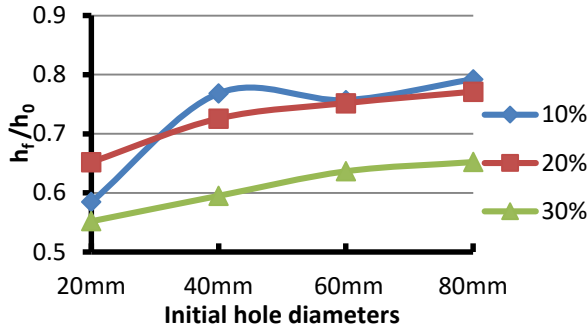
Figure 3-11, for the same C% (20%) and orientation (RD), the relative burnish zone height of DP780s are larger than DP980s due to less TE, as well as the "contraction" effect due to the elastic deformation, which related to difference in reverse strains, of steels after the punch removed.

In Appendix C, by observing plots of other cases with different C% (10%, 20%) and different orientation (RD, TD), the following trend can be observed:

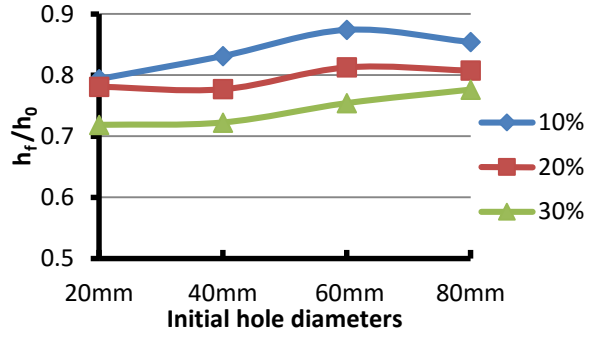
1. For all 3 cases, value of RBH of DP780 are higher than DP980, which implies as the increase of UTS the value of RBH decreases.
2. For only DP780, as the increase of UTS, the value decrease; for DP980 no obvious trend were found.

3.4.3 Fracture zone relative height (RFH)

In Figure 3-12 fracture zone relative heights (RFH or h_f/h_0) versus to d_0 are presented.



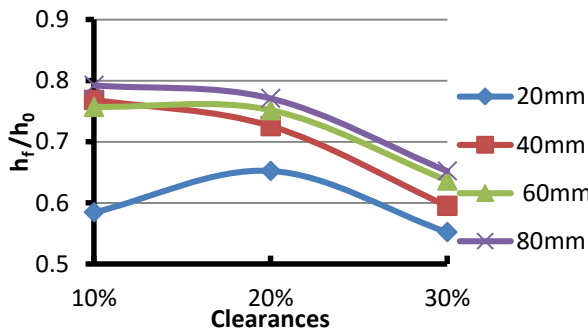
(a) DP780 EG 1.4 RD



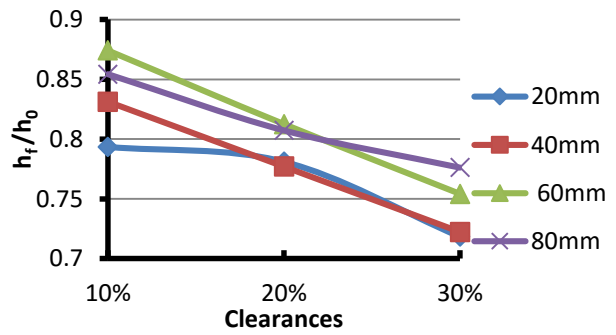
(b) DP980 GA 1.4 RD

Figure 3-12 RFH with respect to d_0 , with different C%, for DP780 and DP980

In Figure 3-13 fracture zone relative heights respect to clearance are presented.



(a) DP780 EG 1.4 RD



(b) DP980 GA 1.4 RD

Figure 3-13 RFH with respect to C%, with different d_0 , for DP780 and DP980

Figure 3-12 and Figure 3-13, for same materials, as the increase of D_0 , the value of RFH increases; as the increase of C% value of RFH decreases, this is because as the increase of gap between tool and die, the deflection of metal sheet become more severe, thus the portion of outline represents the fracture zone divert from the vertical direction with more degrees, and the length projected in the vertical direction is shorter.

In Figure 3-14, measured fracture zone relative height of DP780 and DP980 are presented versus to ultimate tensile strength (UTS).

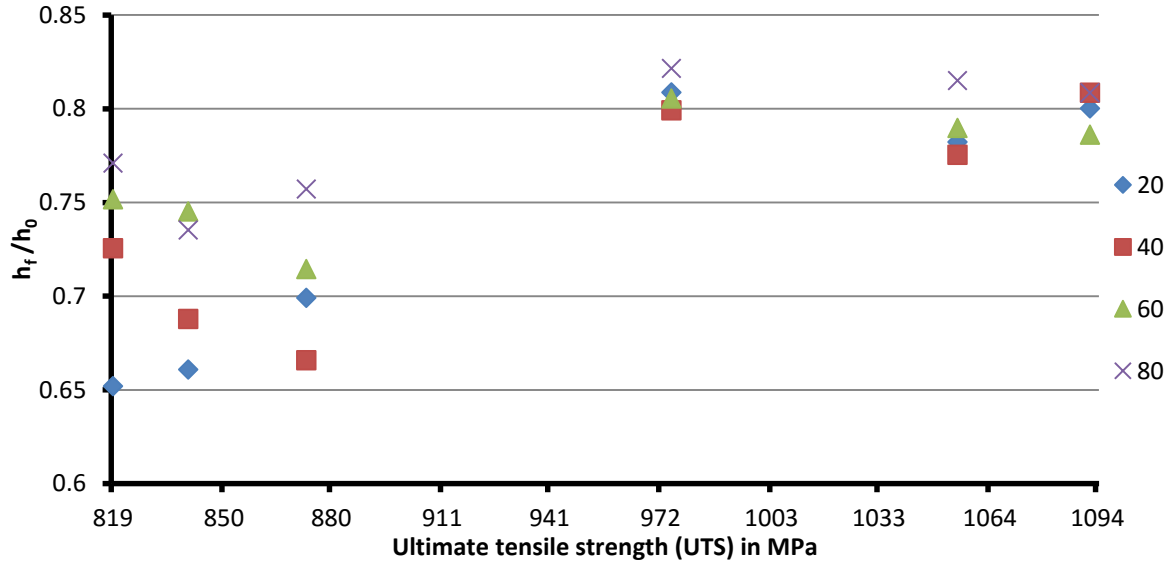


Figure 3-14 RFH with respect to UTS, with $C\%= 20\%$ RD, different d_0

Figure 3-14, for the same $C\%$ (20%) and orientation (RD). Values of h_f/h_0 for DP980s are higher than DP780s, this may due to lesser TE.

Appendix C, by observing plots of other cases with different $C\%$ (10%, 20%) and different orientation (RD, TD), the following trends can be observed:

1. For cases $C\%= 20\%$, and 30% both in RD and TD, values of h_f/h_0 for DP980 are higher than DP780. For $C\%= 10\%$, the differences between DP780 and DP980 are not obvious.

3.5 FE simulation of hole punching process

In punching process, the fracture within the clearance zone is a problem involves large strain, material nonlinear, and contact. FEA provides an approach to research the fracture process, which is beyond the range of human perception or hard to be observed in practice, in an intuitive way.

According to ABAQUS Manual [47], both implicit and explicit methods are capable to simulate the punching process. In ABAQUS Damage initiation and evolution law describe the failure process in the scenario: after reaching damage initiation criterion, displacement tolerance based damage evolution laws phenomenally describe the deterioration of material elasticity modulus (or load-carrying capacity), fracture initiation and propagation process are intuitively demonstrated by deleting elements. For using damage models to simulate punching-like processes, Shim et al. [48] and Söderberg [49] used ductile models;

Husson et al. [50] used a customized damage model; Dalloz et al. [51] and Marouani et al. [52] used Gurson-Tvergaard-Needleman (GTN) model; Hu et al. [53] used Rice-Tracy model.

ABAQUS/Explicit is used to simulate the punching process, damage parameters were decided by trial and error. For details of damage criteria, please reference Appendix E. Figure 3-15 is the sketch of the model to research the punching process.

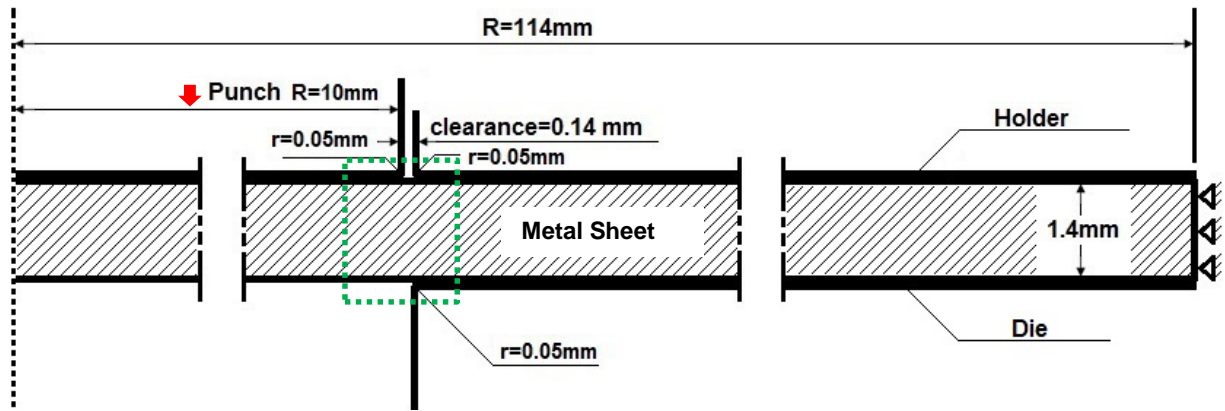


Figure 3-15 Sketch of the punching process model

Figure 3-15, the model is axisymmetric about y-axis, right side of the metal sheet are full constrained; punch and holders are assumed as rigid bodies, holders are full constrained, punch moves in negative y direction, marked with red arrow, to deform the metal sheet within the green box, which is the area of interest (AOI).

Figure 3-16 are stress distribution of DP780 steel sheets within the AOI under three different clearance conditions, C%=10%, 20%, and 30%, as shown in the area within the green box in Figure 3-15.

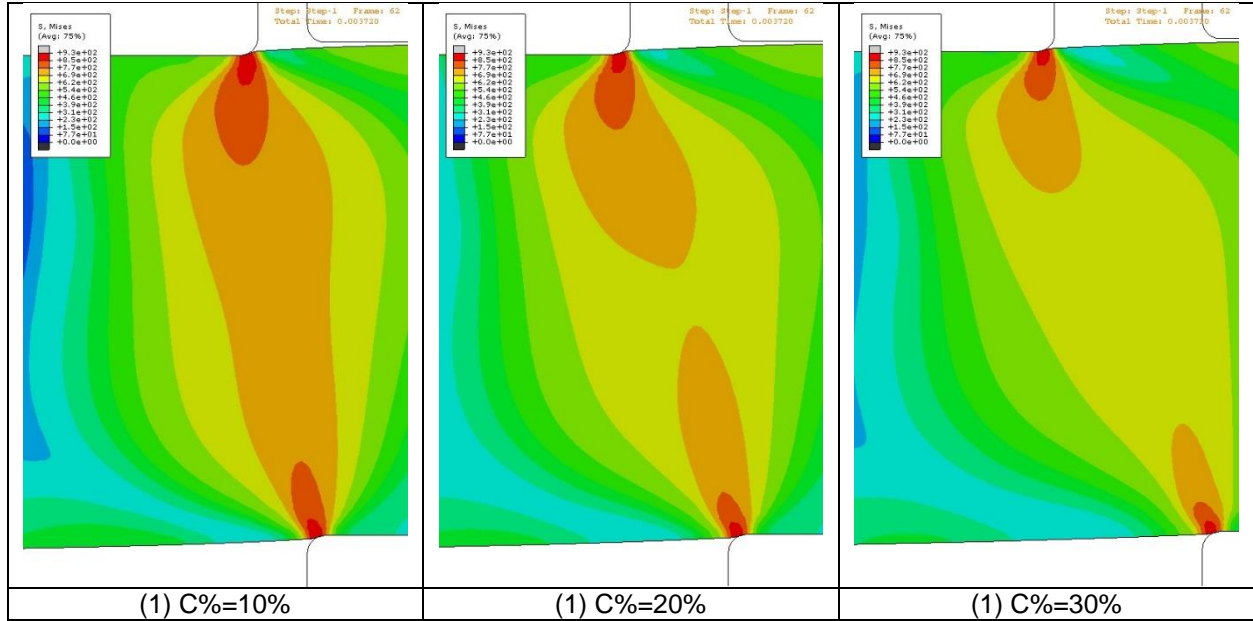


Figure 3-16 Von Mises contour of DP780 under C%=10%, 20%, and 30% conditions

In Figure 3-16, it can be observed contour sizes of Von Mises stress are different, and as the clearance increases, intensities of stress fields near to both punch and die tips decrease.

Based on the simulation results, it can be speculated that, as the increase of clearance from 10% to 30%, due to the decreasing of stress intensity, crack initiation at the upper side of metal sheet was delayed, and displayed higher rollover zone relative height upon observing the sheared edge in experiment, as discussed in 3.3.1.

Figure 3-17, are stress distribution of DP600, DP780, and DP980 steel sheets within the AOI. Models are with the same boundary conditions, failure criterion, and demonstrated with the same stress scale, only different in stress-strain curves.

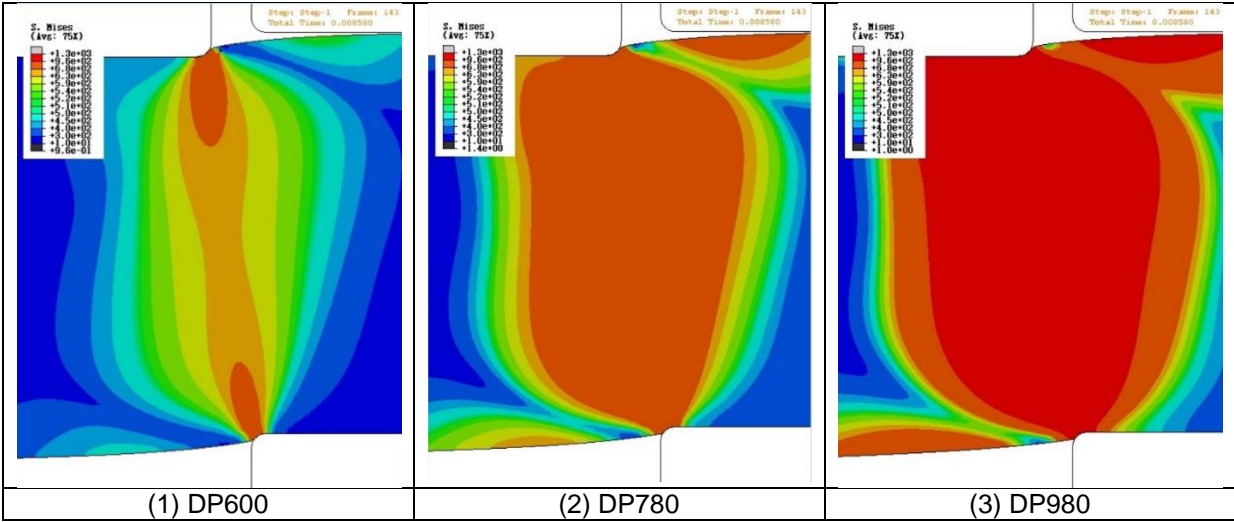


Figure 3-17 Von Mises contour within AOI of DP600, DP780, and DP980 under C%=10% condition

In Figure 3-17, it can be observed contour sizes of Von Mises stress are different, and as the increase of UTS of material the size of deformation affected zone increases. In practice, the shear deformation affected zone of DP600 may be wider than DP980, because DP600 is more ductile than DP980, in punching process crack starts in DP600 will be later than DP980, after the fracture process of DP980 metal sheet is completed, the crack may haven't initiate in DP600, and the size of shear deformation affected zone of DP600 continue increases, finally shows a wider shear deformation affected zone.

In Figure 3-18, in punching process reaction force of the punch are plotted, the simulation condition is C%=10%.

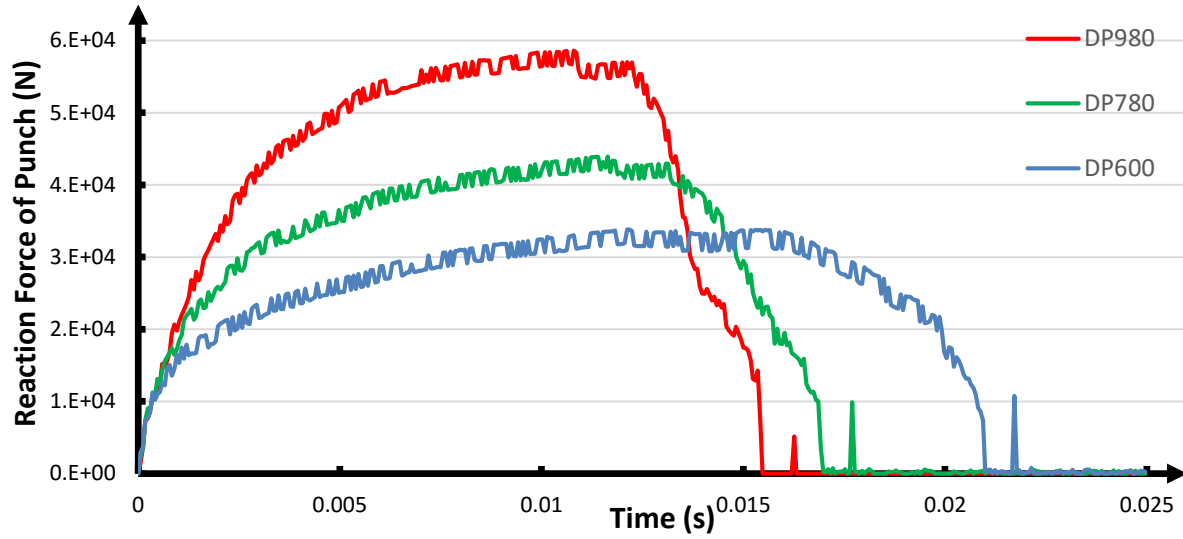


Figure 3-18 Reaction forces of punch in vertical direction under C%=10% condition

In Figure 3-18, it can be observed curve of DP980 shows the highest reaction forces but start to drop earlier than DP600 and DP780; DP600 curve shows the lowest peak reaction force, but the force last longer than DP780 and DP980.

In Figure 3-19 are external works to “break apart” the slug from the steel sheets of DP600, DP780, and DP980 in the punching process.

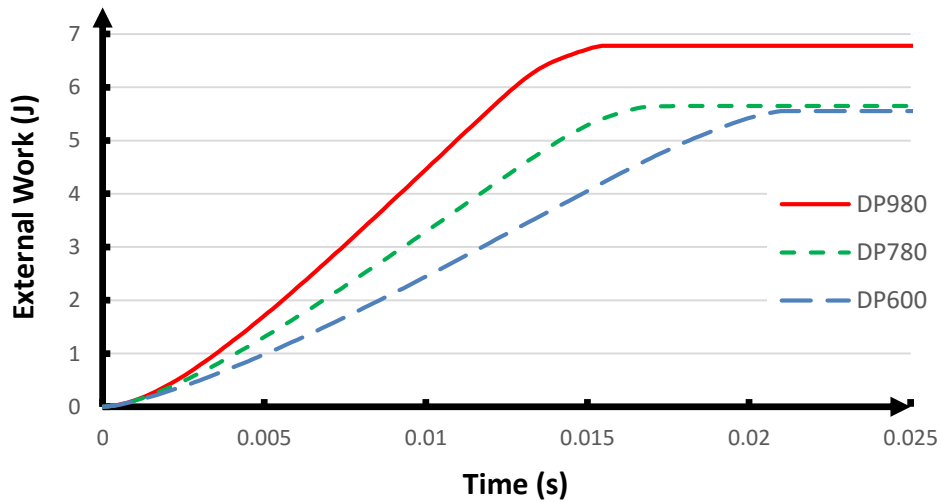


Figure 3-19 External work of punching process model with different steel grades under C%=10% condition

In Figure 3-19, for a curve the energy first increase, then gradually decrease in the increase rate, finally end up with a constant value, which is the total energy consumed (to cut off the slug) in the punching process. The process energy increase at decreasing rate until to a constant value, corresponding to the process from initiation of crack until the slug was completely broke off from the metal sheet, during this process reaction force decreases.

3.6 Conclusions

Based on the analysis of punching process, following conclusions are obtained:

1. Rollover zone height is corresponding to the initiation of crack during the punching process.
2. For the crack propagation process in the punching process, first it is shear mode dominant fracture and then changing to shear and tensile mixed mode fracture.
3. Clearance influence both the fracture initiation and propagation during the punching process.
4. DP780 showed larger rollover zone relative height value in comparing with DP980, as DP780 is more ductile than DP980.

CHAPTER 4 HOLE EXPANDING PROCESS

The hole expansion (HE) test is a widely used method to evaluate the stretchability of metal sheet. In practice, this property of metal sheet is also called sheared edge formability, stretch-flangeability, or stretch flange formability. As described previously the HE test includes two technical processing steps: punching and hole expanding. The punching process created holes of various sheared edge morphologies are the input of HE test. The higher radius the hole can be expanded before the first through-thickness crack appears implies the better “quality” of the metal sheet.

There are two types of hole expansion tests, which are only different in geometries of punches, as shown in Figure 4-1 called hole extrusion (a) and hole expansion (b). In this dissertation, hole expansion test was conducted using the punch with a flat head, as shown in Figure 4-1 (b).

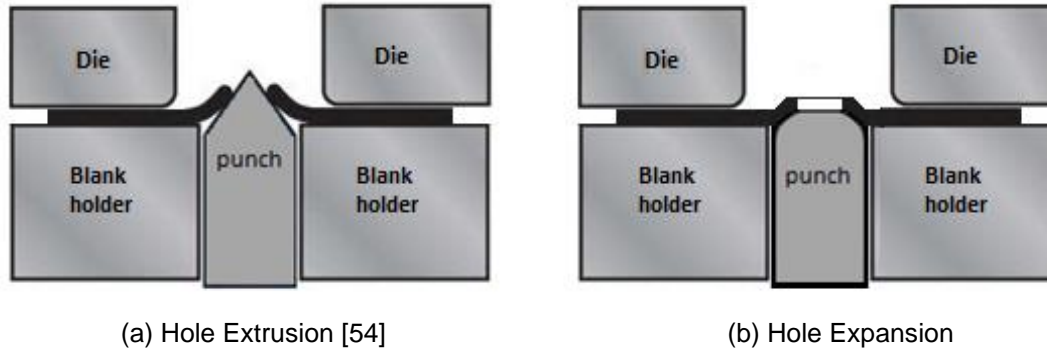


Figure 4-1 Two types hole expansion tests

The material's hole expandability is commonly measured by Hole Expansion Ratio (HER), which is calculated according to Eq. (4.1):

$$\text{Hole Expansion Ratio (HER)} = \left(\frac{d_f - d_o}{d_o} \right) \times 100\% \quad (4.1)$$

Where d_f is the hole diameter at failure, and d_o is the original (or initial) hole diameter.

In this dissertation, effects of selected engineering processing and material property parameters on HER were studied, as listed in Table 4-1. All HE test were performed with the burr (produced in hole punching process) facing up or “burr up” condition, while the flat expansion punch was moving upward from the bottom of the sheet, this prevented the burr from contacting the flat punch head. It is known that “burr up” often gives a lower HER than “burr down”, especially for using a conical punch in the test.

Table 4-1 Investigated parameters for hole expansion test

Engineering Process parameters		Material parameters	
Hole diameters	20, 40, 60, 80	Steel grades	DP780, DP980
Clearances	10%, 20%, 30%	Suppliers	S1, S2

For the hole expansion test, edge condition and material property put a joint effect on the HER. Fracture in the punching process determining geometries and integrities of sheared edges, which showed different HER in HE test; fracture-related mechanical properties of DP steels through influencing the process of crack initiation and propagation on the sheared edges to affect the HER when sheared edge under stretching in hole expanding process.

4.1 Literature review of sheared edge stretching processes

To investigate the sheared edge fracture phenomenon through experiments, Shih et al. [16, 55, 56] used shearing devices with the capability to adjust processing parameters, to study the effect of edge conditions on edge stretchability and proper production piercing or trimming processes for AHSS. Edge stretchability of the sheared specimen is evaluated using sheared edge tension, half dome, and hole expansion tests. According to the research, proposed optimal hole shearing condition and mechanical shearing process can delayed edge fracture in the forming process, result in significantly improved edge stretchability, which can be as good as laser, water jet cutting, and trim polishing processes created edges. Konieczny and Henderson [57] researched the influence of different hole making methods, i.e. ream, laser cutting, and punching with different clearances, on the hole expansion and extrusion results. Presented sheared edge failure modes in various loading modes. Discussed the influence of blanking clearance, various edge morphology parameters, and punch geometry on the formability of AHSS and HSLA. Provided practical recommendations for blanking and hole punching processes for AHSS based on experiment. Chen et al. [58] applied digital image correlation (DIC) method to research the change of strain distribution on surfaces of five AHSS sheets in hole expansion and extrusion tests. Hall et al. [17] reviewed various production case studies of edge fracture phenomenon in forming AHSS. Updated the definition for a well-trimmed edge based on sheared face analysis. Proposed optimal conditions for blanking and die trimming processes. Chiriac and Shi [59, 60, 61, 62] researched the effects of edge strain hardening and prestrain on the edge stretchability; found work hardening in multistage forming prior to trimming or punching processes has little or no effect on edge stretchability. Ilinich et al. [63] compared the hole expansion test

and tensile test of sheared edge; pointed out burr size for particular trimming conditions is more representative of real production trimming.

To simulate the hole expanding process using FEM, Sartkulvanich et al. [64, 65, 66, 67, 68] researched the influence of edge quality on edge stretchability, characterized the edge quality of different punch/die clearances through FEM. Ko et al. [69] researched hole expansion ratios by numerically and experimentally methods with various fracture criteria, including a proposed ductile fracture criterion. Butcher et al. [70] used GTN model to predict the failure of sheared edge in hole expansion test with conical punch, and proposed a novel strategy to account for work-hardening and initial damage near the hole edge for a punched/sheared edge condition. Uthaisangsuk et al. [71] researched stretch flangeability characterization of multiphase steel using microstructure-based failure model.

Various criteria were proposed to predict the edge fracture phenomenon, Shi and Chen [72] proposed a stretch flangeability limit or edge cracking limit, which include material and thickness and shear edge condition parameters, based on hole expansion experimental data. Zhou et al. [73, 74] proposed an "edge thinning limit" for evaluating edge stretching failure for different AHSS. Lou et al. [75] demonstrated the advantage of proposed Lou-Hub criterion in limit dome heights test for square-shaped specimens in comparing with various ductile fracture criteria.

4.2 Initiation of main and associated cracks on sheared edges

In the hole expansion (HE) test, as the hole expanding, minor crack(s) initiate on the sheared edge and gradually forming an observed macro crack under stretching. After HE test, on the sheared edge two kinds cracks can be found, they are: (1) the main crack, this type crack developed into the through-thickness crack, large enough to be seen with the naked eye, and indicated the failure of a metal sheet; (2) associated crack, this type crack failed to form a through-thickness crack, smaller than the main crack, hard to be seen with the naked eye in some cases, existing various locations on sheared edge, and influencing the HER.

4.2.1 Main crack and associated cracks on shear edges

Figure 4-2 is a main crack, it initiated and propagated on the sheared edge, the HE test was stopped as on the top surface of the metal sheet this crack was large enough to be seen with the naked eye.

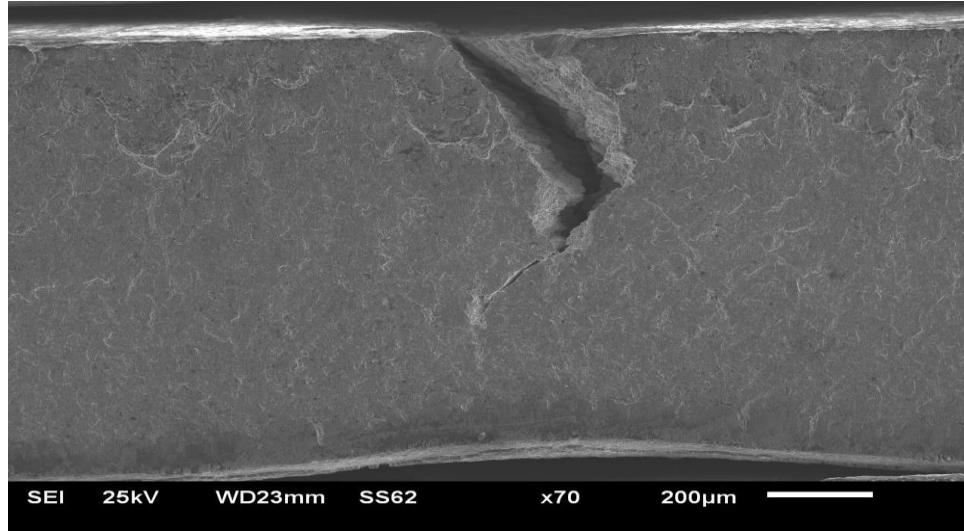


Figure 4-2 Main crack on sheared edge of DP780 GA 1.4, 10%, 80mm (Supplier 1)

In Figure 4-2, it can be deduced that the main crack initiated at the top side, which is the end of fracture zone, of the sample; then the crack propagated on the sheared surface towards rollover zone, as well as in the radial direction on the top side of the steel sheet. The crack propagates in a zig-zag path in around 45° , a direction with the maximum shear stress for this cornered edge line that is under a plane stress in both sheared plane and the top sheet plane, thus is under a uniaxial tension condition in theory. This also implies that the fracture belongs to ductile fracture type. On the sheared surface the crack goes toward the rollover zone, and on the top view is in the radial direction.

In Figure 4-3 and Figure 4-4, beside the mentioned crack initiation site at the top surface of the sheared edge, it has been observed that associated cracks initiated in the center (fracture zone) and bottom (burnish zone) of sheared edges. The burnish formation also provides a probability to develop the pre-notch on the sheared edge surface, causing stress concentration and crack initiation.

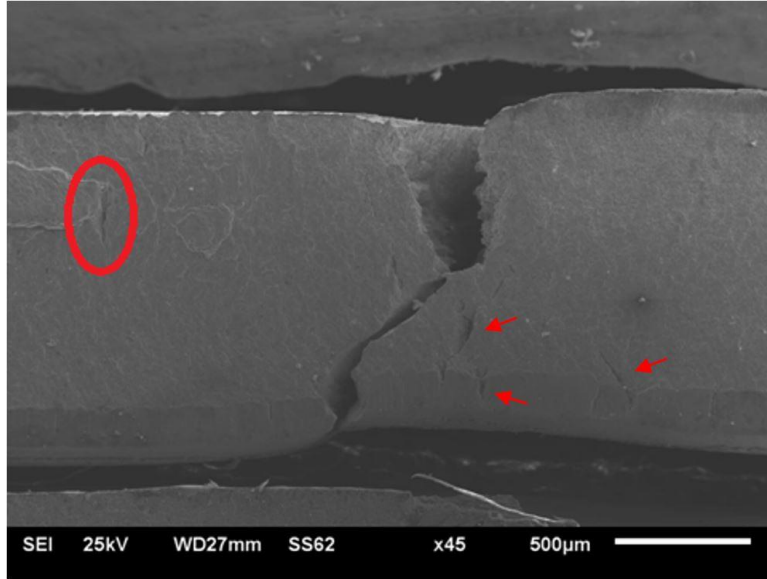


Figure 4-3 Associated crack on sheared edge of DP780, GA 1.4, Supplier 1

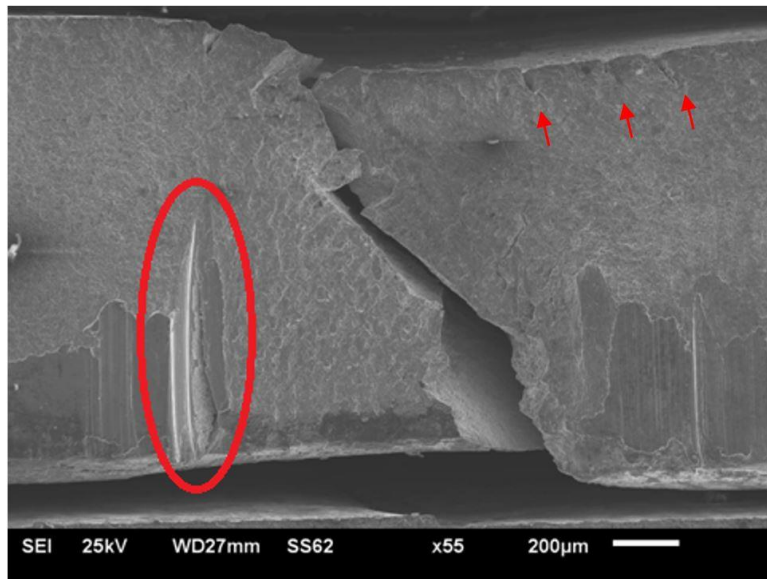


Figure 4-4 Associated cracks on sheared edge of DP980, GA 1.4, Supplier 2

In practice, the crack initiation condition is complex, which influencing by multiple factors such as geometry and material's response to punching process introduced damages, these features hardly to (explicitly) be described by FEM, so usually be "smeared" by a failure criterion in modeling. The kind of simplicity of features of sheared edge increasing the difficulty in predicting edge fracture using FEM.

4.2.2 FEM simulation of stress variation on sheared edges

Finite element models were built in ABAQUS to analyze variation of stress on the simplified sheared edges in hole expanding process. Figure 4-5 is the sketch of the model.

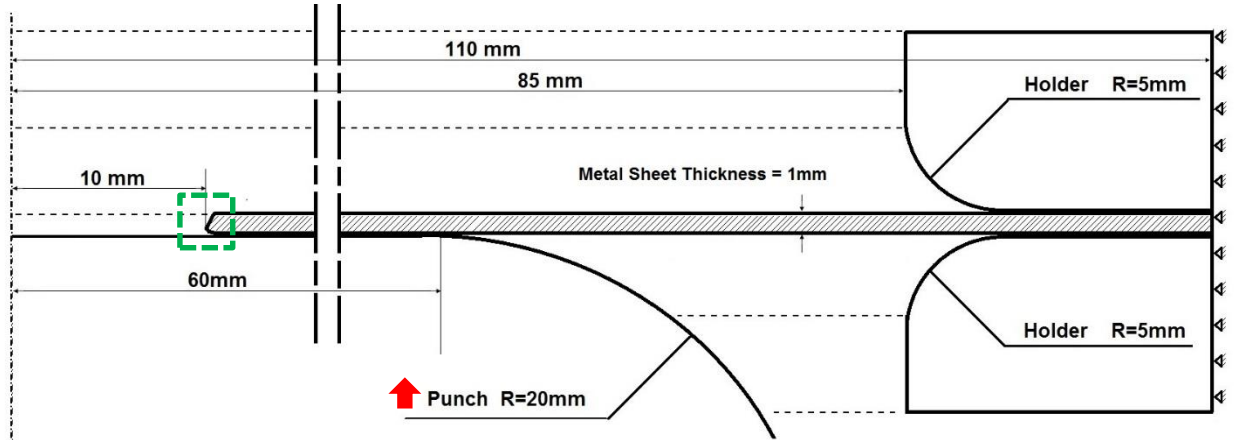


Figure 4-5 Sketch of hole expansion test model

In Figure 4-5, in the model, holders and punch are rigid bodies, metal sheet is the only deformable part. The outer side of the metal sheet and holders are fully constrained. AOI is marked with a green dash line rectangular, the movement direction of punch is marked with the red arrow. The simulated deformed (1/4) metal sheet are presented in Figure 4-6. The input of property of metal sheet was from true stress-strain curve of DP780 in uniaxial tensile test, no failure criterion was assigned to this model.

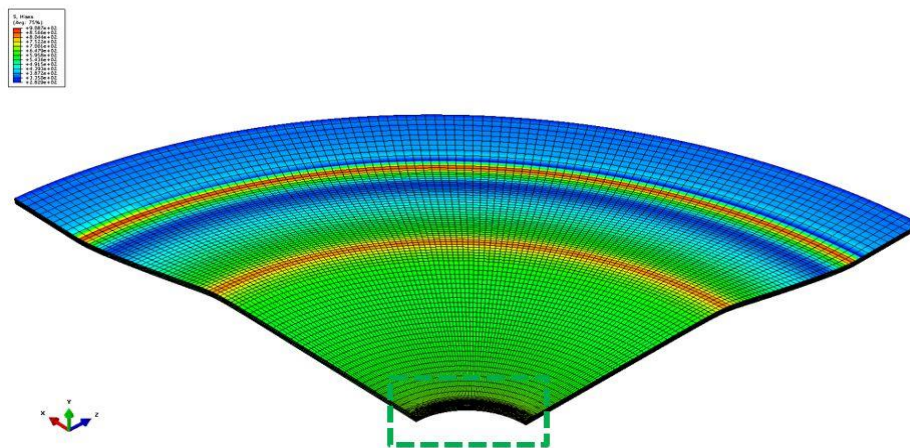


Figure 4-6 Deformed metal sheet in HE test (quart model)

In Figure 4-6, the sheet metal was simplified as a quart of full size in order to save the computing time. AOI is marked with a green dash line rectangular. Comparing with the 2D punching process model, the 3D model can be used to research the circumferential (or hoop) strain and stress on the sheared edge.

To investigate the influence of sheared edge geometries, the AOI in Figure 4-5 and Figure 4-6, sheared edges with different geometries were built, as shown in Figure 4-7, (a) and (b).

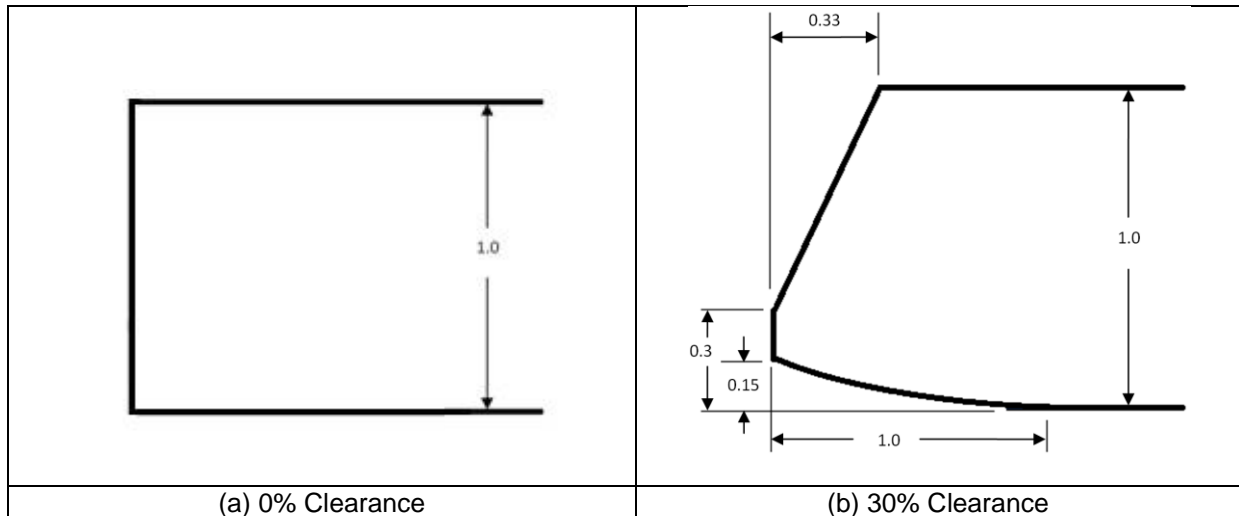
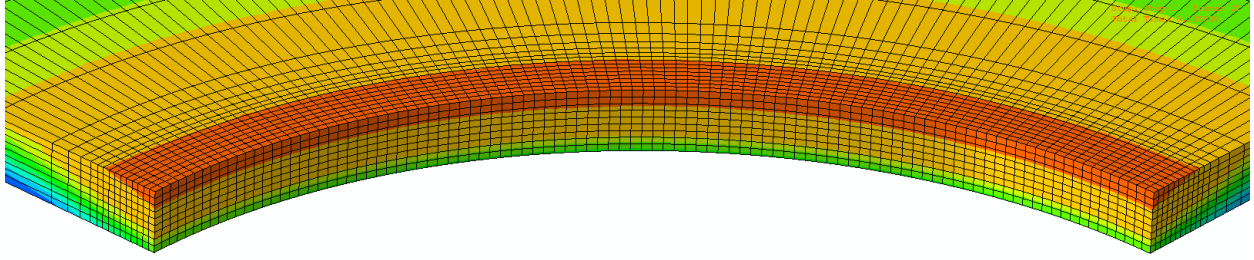


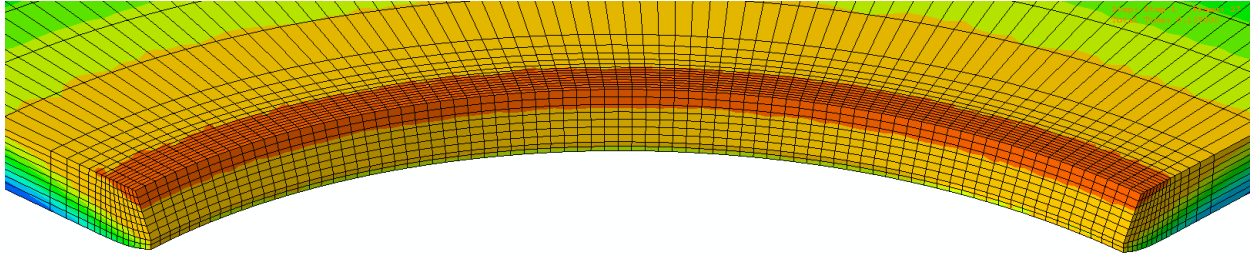
Figure 4-7 Sketches of sheared edge profiles

Figure 4-7, (a) and (b) are simplified (sheared) edge geometries, they represent two extreme conditions of sheared edge geometries. For (a) 0% clearance, the sheared edge was assumed with an ideal rectangular shape, without including the rollover, burnish, and fracture zones' geometric features. For (b) 30% clearance condition, the geometry of sheared edge is similar to experimentally observed sheared edge, which was punched under $C\%=30\%$ condition, with geometric features of rollover, burnish, and fracture zones.

Stress distributions on sheared edges were analyzed to deduce the cause of crack initiation. Simulation results are presented in Figure 4-8, (a) $C\%=0\%$ condition; (b) $C\%=30\%$ condition. The only differences between these two cases are the geometries of sheared edges, which correspond to (a) and (b) in Figure 4-7. In both cases, initial hole diameters were 20mm, the residual stress caused by shearing deformation in the punching process was not considered, and assumed surfaces of sheared edges are smooth, without fracture-caused rough surface features or punching process introduced damage.



(a) 0% Clearance



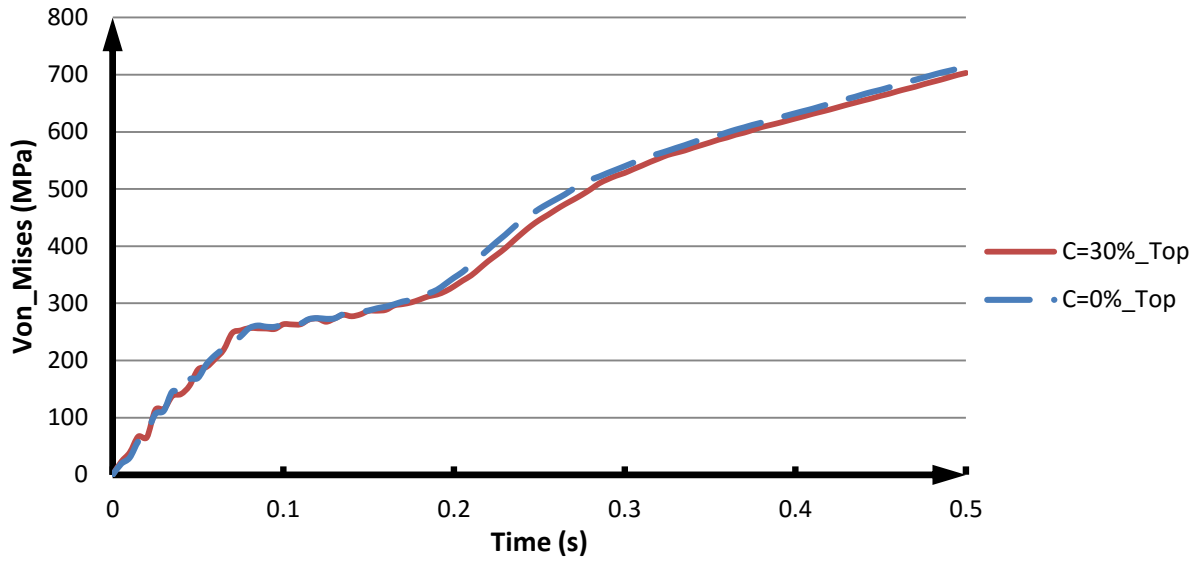
(b) 30% Clearance

Figure 4-8 Stress distribution on sheared edges, with $d_o=20\text{mm}$

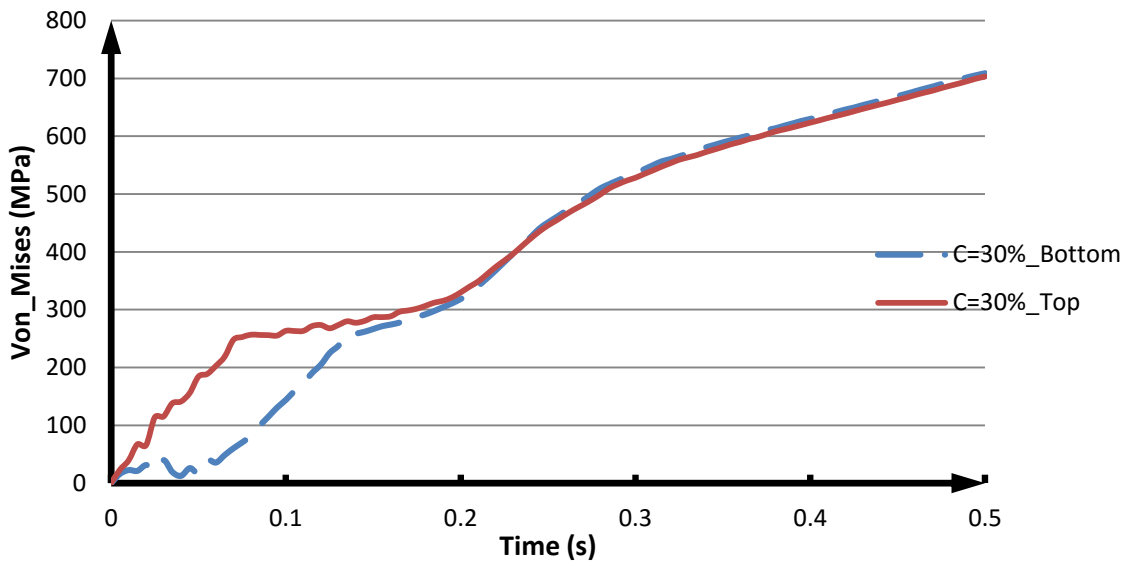
In Figure 4-8, it can be observed that a higher stress appeared at the upper edge of the hole, which matches to the observed crack initiation site (upper side of sheared edge), as shown in Figure 4-2.

From mechanics viewpoint an ideal in-plane hole expanding may not generate different through-thickness stress, in real hole expanding process with a flat punch the hole area has a tendency to lift up due to the punching induced sheet bulging away from the flat plane at the early state, resulting in the different through-thickness stress distribution.

In Figure 4-9 (a) and (b), variation of Von Mises stress with respect to time for different locations on sheared edges are presented. In (a), histories of Von Mises stresses of two nodes at upper side of sheared edges of $C\%=0\%$ and $C\%=30\%$ models are compared; In (b), histories of Von Mises stresses of two nodes at the top and bottom sides of sheared edge of $C\%=30\%$ model are compared.



(a) Histories of stresses at the upper side of sheared edges with C%=10% and 30%



(b) Histories of stresses at the top and bottom sides of sheared edge with C%=30%

Figure 4-9 Histories of Von Mises stresses at different locations of sheared edges

In Figure 4-9 (a), comparing Von Mises stress of two nodes at the top and bottom of C%=30% clearance condition, it can be deduced that the influence of sheared edge geometries on stress values are not obvious.

Figure 4-9 (b) comparing stresses at the top and bottom edges with C%=30% condition, the initial portion of the punch displacement (about 1/3 of the total displacement or time as shown) shows remarkably higher stress at the top than that at the bottom. This is consistent with the observed crack initiation site at

the top edge, as shown in Figure 4-2. Despite that this stress difference disappeared for the rest 2/3 total displacement (or time), the cumulated total crack propagation would still be larger at the top than at the bottom in both crack population and mean crack opening distance, as that observed in Figure 4-2.

For no failure criterion was assigned in these models, so the stress curves showed a monotonically increasing trend, in the real case, for a stress curve after researching the peak value, stress will decrease due to material weakening.

4.3 Experimental observation and data analysis of hole expansion test results

After HE test, samples with the same clearance but different initial hole diameters had been piled up and edge cracks were marked with red arrows, as shown in Figure 4-10.

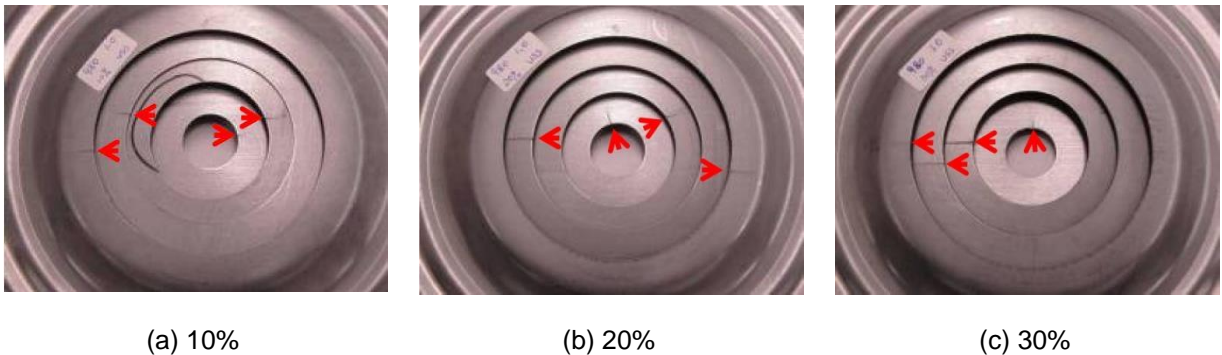


Figure 4-10 Hole expansion test results of DP980, GA 1.0, with different d_o and C%

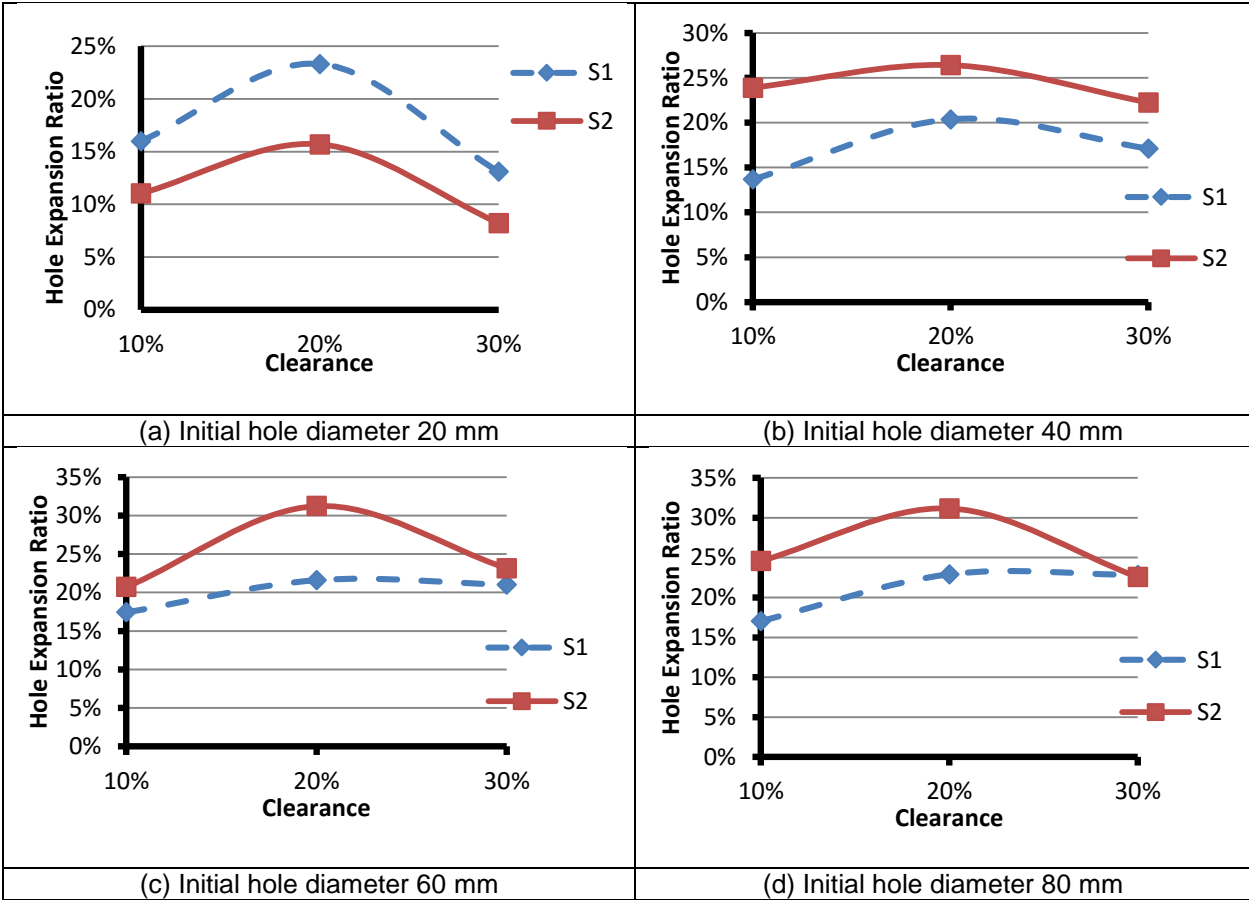
It can be seen in Figure 4-10 that all cracks were initiated at the sheared edge, with a high probability to initiate in rolling direction, for all three C% and for almost all d_o conditions, except for the smallest d_o at 20 mm. All cracks propagated in the radial direction.

After HE test the fractured samples were cut and examined with optical microscope and scanning electron microscope (SEM). A comparative study on different steel grades (DP780, DP980), initial hole diameters (d_o), and material sources (S1, S2, suppliers with different thermomechanical processing conditions) were used to reveal the fracture mechanisms.

4.3.1 Effects of investigated parameters on HER

In Table 4-2, HER data of DP780 from two suppliers, S1 (blue) and S2 (red), were compared, for details of these data, please reference appendix F.

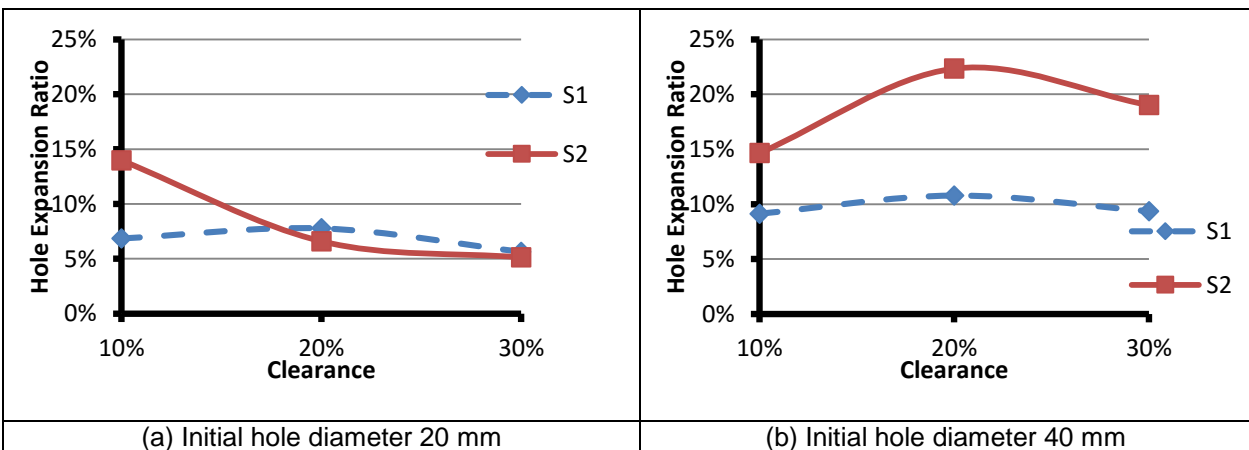
Table 4-2 Comparison of HER for DP780 1.4 from two suppliers (S1 and S2)

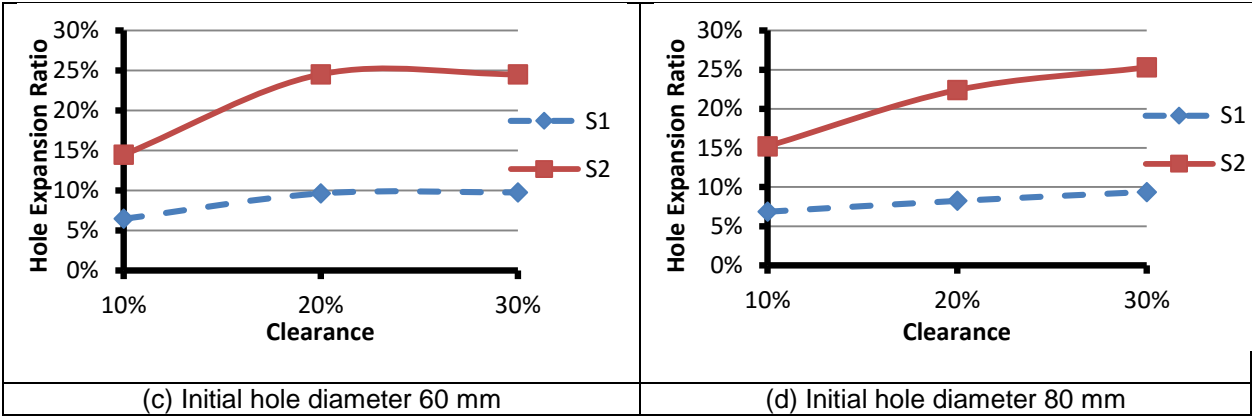


In Table 4-2, except for $d_o=20$ mm condition, Supplier 2 showed greater HER than supplier 1; HER reached the maximum values under $C\%=20\%$ condition.

In Table 4-3, HER data of DP980 from two suppliers, S1 (blue) and S2 (red), are compared, for raw data please reference appendix F.

Table 4-3 Comparison of HER for DP980 1.4 from two suppliers (S1 and S2)





In Table 4-3, except for $d_o=20$ mm condition, Supplier 2 showed greater HER than Supplier 1; for $d_o=20$ mm condition, curves represent Supplier 1 and 2 crossed; for $d_o=80$ mm condition for both suppliers, HER increased monotonically; for Supplier 2 under $d_o=40$ mm and 60mm and for Supplier 1 under $d_o=20$ mm and 40mm conditions, HER reach the maximum values under $C\%=20\%$ condition. Table 4-3

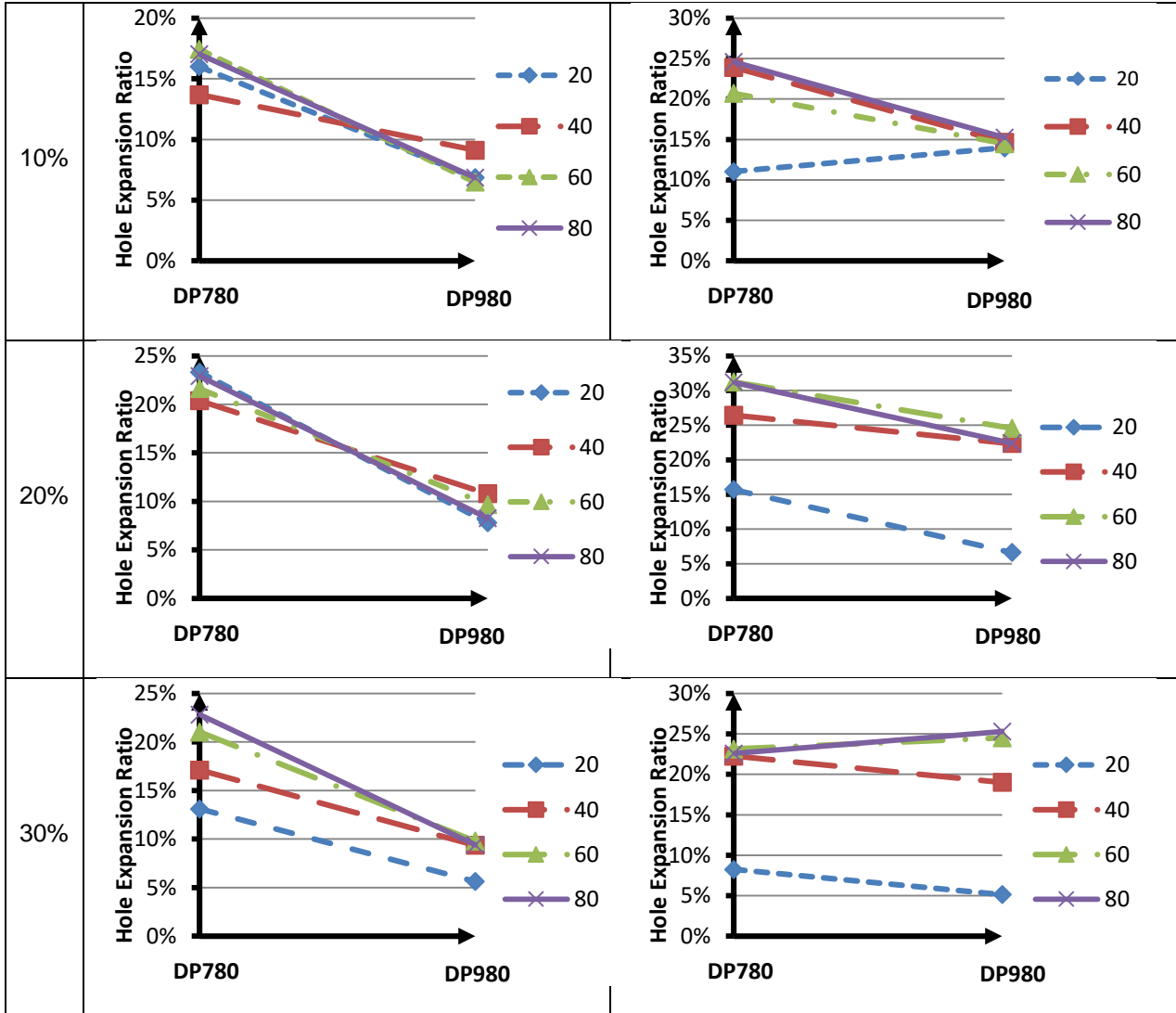
In Table 4-2 and Table 4-3, the observed phenomena revealing the dominant influence of clearances on stretchabilities of sheared edges and it is a nonlinear relationship between clearance and HER. The differences in HER values between two suppliers are determined by fracture-related mechanical properties, which might be caused by different manufacturing processes.

A hypothesis to explain the cause of differences in HER values is that under different clearance conditions, punching process introduced different severities of “damage” to sheared edges, which led to different HER. Base on this hypothesis and along with HE test results, it can be deduced that the relationship of clearance and punching process introduced damage is nonlinear: apparently for DP780 at 20% clearance condition punching process introduced the minimum damage to sheared edges, resulting in the highest HER.

In Table 4-4, HER data of DP780 and DP980 in Table 4-2 and Table 4-3 are presented with respect to steel grades.

Table 4-4 HER with respect to steel grade, with different suppliers, d_o and $C\%$

C%	Supplier 1	Supplier 2
----	------------	------------



In Table 4-4, following phenomena were observed:

1. For both suppliers, under C%=10% and 20%, d_o greater than 20mm conditions, HER values were not sensitive to the d_o. Under this conditions, the HER is predictable, and obtained data have the potential to be applied to cases with even greater d_o.
2. For Supplier 1, in all clearance condition DP780 results are greater than DP980, this trend only applying for Supplier 2, under C%=10% and 20%, d_o greater than 20mm conditions.
3. For Supplier 2, under C%= 30%, d_o= 60, 80mm, and C%=10%, d_o= 20 mm conditions, HER of DP980 are greater than DP780.

Observed phenomena revealed that for both suppliers, HER values are not sensitive to d_o when d_o were greater than 20 mm.

4.3.2 Observing edge cracks using optical microscope

Figure 4-11 and Figure 4-12, by observing edge cracks using optical microscope it has been found that there existed multiple edge cracks at various crack growth stage, allowing discover the crack initiation and propagation processes: cracks initiated from the top (burr side) on the sheared edges, then propagated through the thickness, finally formed macro edge cracks.

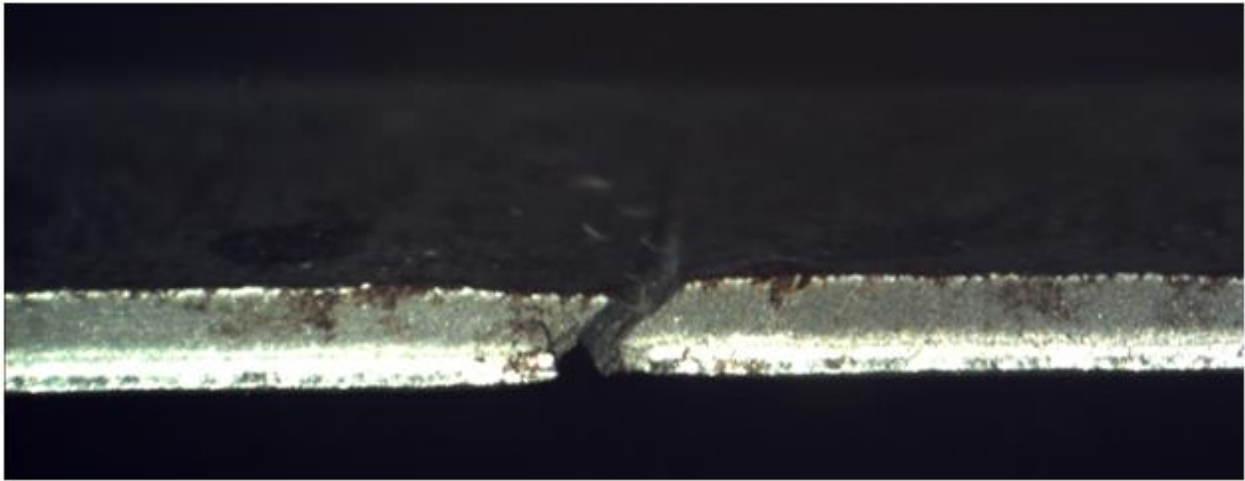


Figure 4-11 Typical edge crack phenomenon of steel sheet from Supplier 1, DP980 0.96

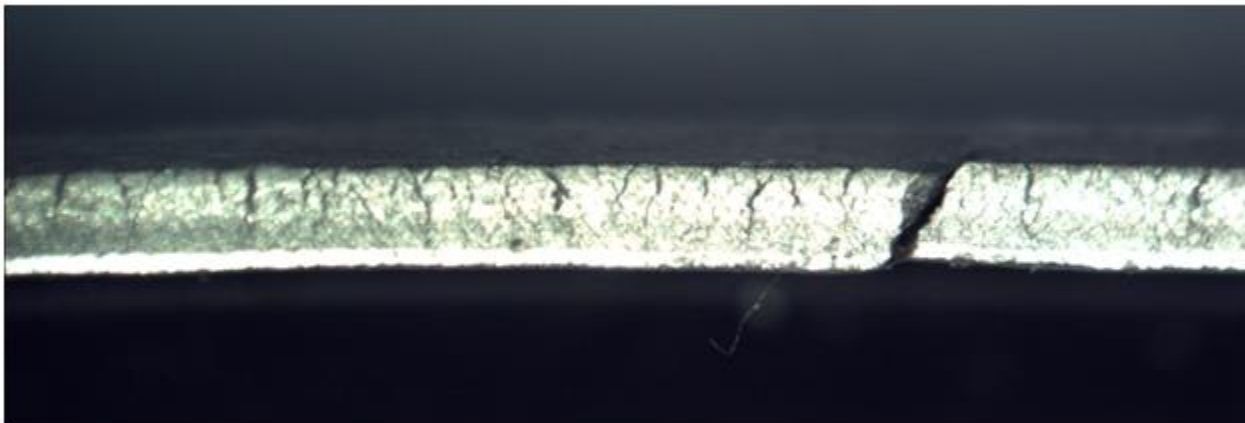


Figure 4-12 Typical edge crack phenomenon of steel sheet from Supplier 2, DP780 EG 1.4

Figure 4-11 and Figure 4-12 the edge fracture morphologies from two suppliers show distinct features:

1. For Supplier 1, except for the through-thickness main crack, no other obvious associated crack was observed on the sheared edge.

2. For sample from Supplier 2, besides the main crack, many smaller associated cracks were observed. These cracks initiated at the top (burr zone or end of fracture zone), propagated toward the bottom (burnish zone) at different stages of development when the main crack penetrated the entire thickness.

Based on observed phenomenon and combine data analysis in in Table 4-2 and Table 4-3, it can be speculated that, the HER values of steel sheets from Supplier 2 are greater than from Supplier 1 is because of the initiation of associated cracks at top side of sheared edges releasing the strain created by stretching, by dispersing stress concentration sites the formation of through-thickness main crack was postponed; while for samples from Supplier 1, main crack was the only place of stress concentration and the stretching deformation in hole expanding process promoted the crack propagated in both thickness direction (on the sheared edge) and radial direction (top surface of the metal sheet). The differences in crack initiation mechanisms caused the main crack initiated and propagated at different time and rates, reached to the size could be seen with the naked eye at different time, and showed as different HER values.

It is worth mentioning, similar conclusion were obtained according to experiments conducted by Wang et al. [76]. For Aluminum sheet 6111-T4 processed using different shearing devices, sheared edges showed different fracture mechanisms. So in practice, using the suitable pre-processing technique will lead to more favorable fracture process and better stretchability of sheared edge.

4.3.3 Observing edge cracks using scanning electron microscope

To investigate the failure mechanism of steels from two supplier, edge cracks were observed using SEM, more comparison of the edge cracking of DP980 from two material sources were made in Figure 4-13.

Supplier 1	Supplier 2
------------	------------

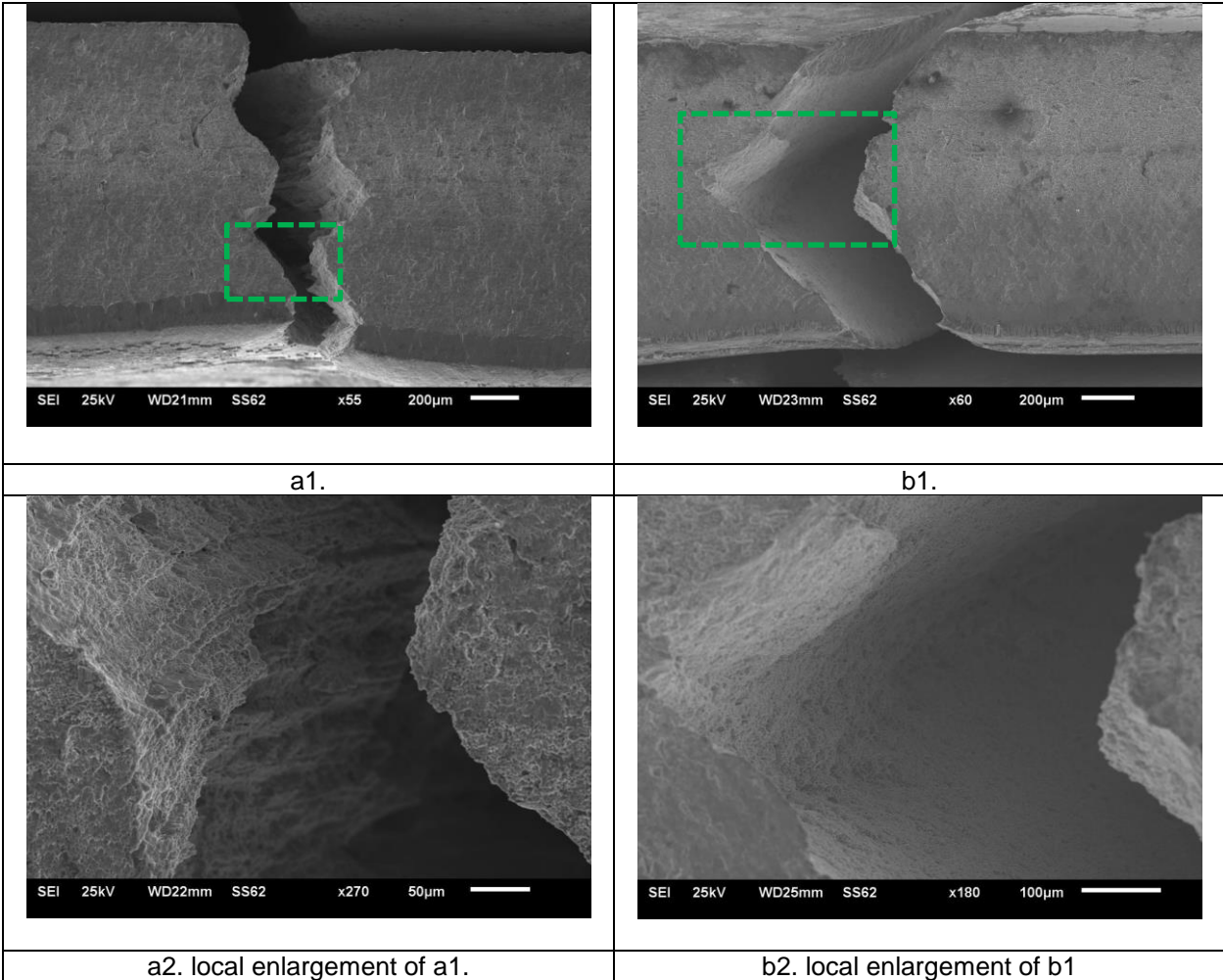


Figure 4-13 Edge cracks on sheared edges of DP980 from two suppliers

In Figure 4-13, in examining fracture surfaces of edge cracks for steel sheets from the two material sources, it has been found that material of Supplier 1 (on left) has rougher fracture surfaces, material from Supplier 2 (on right) has smoother fracture surfaces. It is commonly recognized that the rough fracture is formed from the formation of dimples, micro conical “cups”, or “honeycombs”, a local ductile fracture process involving cavity nucleation from original material inclusions or defects (grain boundary triple junction, dislocation concentration etc.), followed by ductile plastic deformation and finally local necking. Thus, the rougher fracture surface from Supplier 1 suggests that this material is more ductile than that from Supplier 2. The difference in fractographies can be attributed to the differences in microstructures.

This observation is rather surprising because it is in conflict with the hole expansion results, that Supplier 1 steel sheets with more ductile fracture morphology showed lower HER than Supplier 2. An

explanation for this conflict between conclusions been deduced based on experimental observation at microscale and test result at macroscale is that: the initiation of multiple associated cracks on sheared edge of steel sheets from Supplier 2 (less ductile) putting a positive effect in increasing HER at the macroscale.

4.3.4 Interaction of two parallel cracks in crack propagation process

An FE model was built to show the interference between two parallel cracks in their propagation processes, as shown in Figure 4-14. Two pre-defined cracks at the top edge with 0.7 spacing were named as crack "a" and crack "b", respectively; two sides of the model are stretching with pressure equals to 800; the left lower corner of the model was fully constrained; y-direction movement of the right lower corner was constrained. The damage initiates when value maximum principal stress is larger than 1000; damage evolution is energy type, the value of fracture energy is 50.

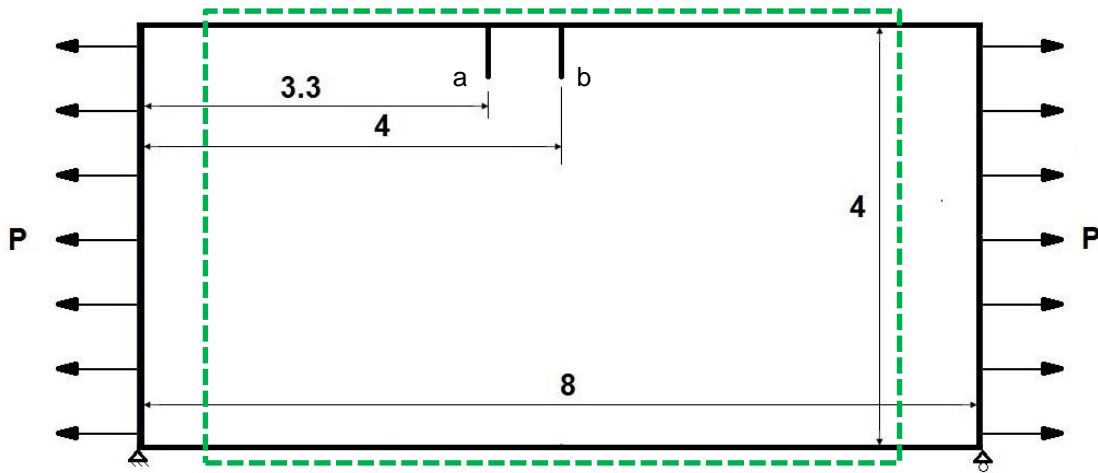
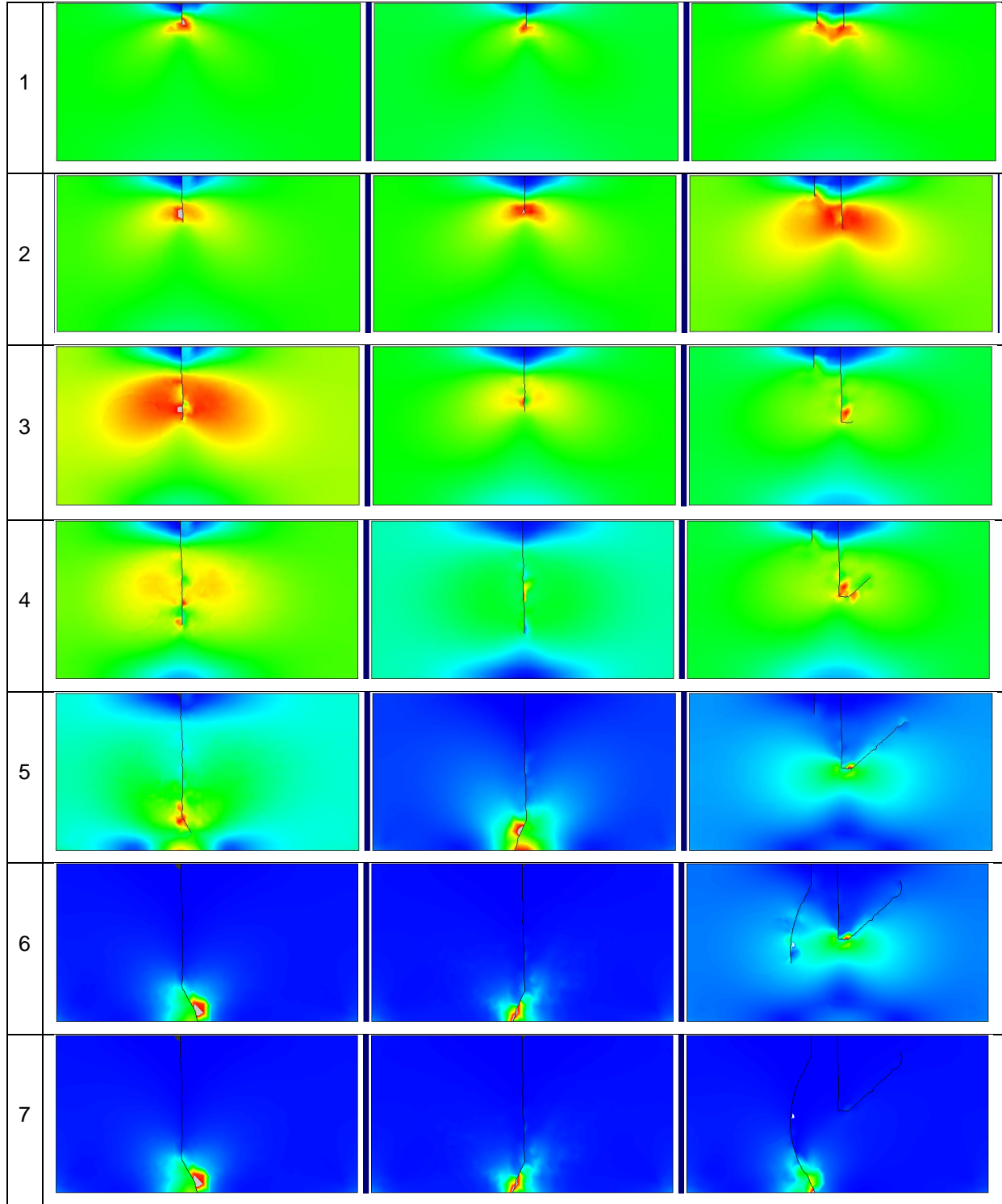


Figure 4-14 Sketch of dual-crack model

In Table 4-5 are crack propagation histories of models with single crack and dual cracks. First and second columns are single edge crack cases, only a crack "a" and "b" was pre-defined on the top edge, respectively; the third column is the dual-crack case, two cracks exist on the top edge, this case can be considered as a superimpose of previous two single-crack cases, as shown as shown in Figure 4-14.

Table 4-5 Simulation of crack propagation and interference

	Crack a	Crack b	Dual cracks



Comparing simulation results of single crack and dual-crack cases, following phenomena were observed:

For the first and second columns (single edge crack cases):

Row 1: the sizes of stress fields under single crack conditions are smaller than that under dual-crack condition;

Row 2-3: as the lower stress intensity of the single crack it grows slower, as compared with the superimposed crack tip stress field of the dual crack case;

Row 4-5: without the influence of a neighboring crack as that occurred in the dual crack case, cracks propagate straight downward at a higher speed, in the latter case, crack propagation path deflect;

Row 6-7: continuous growth of the single crack reaching the bottom with limited path change, except at the end close to the through-thickness the stress state changes to a plane stress condition, requesting the crack to develop in a 45 shear direction for a ductile material, which also applied to dual crack case.

For the third column (dual edge crack case): when there are two cracks in a sample, the evolution of the cracks can be described as the following progressive events:

Row 1: initially each crack generates a stress intensity zone and leaves a released stress zone behind the crack tip. The two high stress fields in front of the crack tips are overlapped and superimposed, shows a symmetric pattern;

Row 1-3: then the crack "b" (right) advanced faster than the crack "a" (left), inhibits the propagation of the crack "a", resulting in increased difference in crack length and shows the asymmetric stress field pattern. This situation continues to develop up to a certain stage;

Row 3-5: the crack "b" diverts its propagation path from the original vertical direction to the side direction away from the crack "a", so in terms of its propagation the crack has been arrested. In this period, the crack a has limited growth, but the deflection of crack "b" suggests that effect of the crack "a" on the stress field starts to be realized;

Row 6-7: after the crack "b" deflected aside it has no more important contribution to the total displacement or summed crack opening, resulting in the crack "a" to re-start to propagate and becomes the major crack. Under the effect of crack "b", crack "a" propagates with the path slightly tilted away from the crack "b", apparently to avoid development within the stress hardened region caused by the crack "b". Finally, this originally inhibited crack a developed into a through-thickness main crack.

Above simulation results revealed the complexity of crack propagation under the dual crack condition, showed the effect of crack under on the failure process of the whole sample, and implies the interaction of

dual cracks delayed the “break off” of the whole sample. In a similar manner, multiple cracks (Figure 4-12) are initiating simultaneously with the increasing of circumferential displacement, their mutual interactions delayed the development of through-thickness crack during the hole expanding process, enhanced the failure hole diameter at the macroscale and resulting in a higher HER as compared with that of single crack case (Figure 4-11). It can be said, initiation of multiple cracks on sheared edge positively influencing the HE test result. In this regard, sheared edges of metal sheets from Supplier 2 (Figure 4-12) showed higher HER, for all C% and almost all d_o , except the $d_o=20\text{mm}$ case, in which the total circumferential length of the hole is too small to provide sufficient number of cracks under simultaneous development and to show this crack interaction effect.

It's worth mentioning that simulation results have only limited similarity to the experimental observation, the interaction of cracks in real cases are far more complex, which may beyond the capability to be explicitly described by FEM.

4.4 Criteria for edge fracture at macroscale

Based on previous works, HE test results and observed DP steel grain structures, an empirical criteria to predict edge fracture was proposed. This criterion includes mesoscale grain structure features of DP steels, and it can be applied to predict the HE test results of DP steels.

4.4.1 Previous works

Adamczyk and Michal [77] proposed a criterion Eq.(4.2) to predict the failure of hole expansion for sheared plus deburred holes, with hole expansion ration (HER) to be the linear function of TE of the material:

$$\text{HER} = C_1(r_m)(e_t) + C_2 \quad (4.2)$$

e_t : total elongation.

$r_m = \frac{r_0 + 2r_{45} + r_{90}}{4}$, 0, 45, and 90 indicate the number of degrees from the rolling direction.

For High Strength Low Alloy (HSLA) steels, $C_1=1.7$ and $C_2=15$.

Comstock, Scherrer, and Adamczyk [78] studied the hole expansion of three stainless steels, and proposed the criteria Eq.(4.3) and Eq.(4.4). The tested materials were ferritic, ferritic stainless, and austenitic stainless steels (304, 304L, and 316, respectively) under machined and sheared plus de-burred hole conditions:

$$\text{HER} = C_3t + C_4e_t + C_5r_m \quad (4.3)$$

$$HER = C'_3 t - C'_4 n_t - C'_5 \quad (4.4)$$

Eq.(4.3) are regression analysis results of machined hole condition; $C_3=478$, $C_4=2.56$, and $C_5=35.3$. Eq.(4.4) was used for sheared plus de-burred hole condition, which dependent on the work-hardening rate; $C'_3=85.7$, $C'_4=31.4$, and $C'_5=23.6$.

t: thickness.

e_t : total elongation (TE).

n_t : work-hardening rate.

$r_m = \frac{r_0 + 2r_{45} + r_{90}}{4}$, 0, 45, and 90 indicate the number of degrees from the rolling direction.

$r = e_w/e_t$, plastic strain ratio or Lankford value.

True width strain $e_w = \ln(w_f/w_o)$; w_f : Final width; w_o : Original width.

True thickness strain $e_T = \ln(t_f/t_o)$; t_f : Final thickness; t_o : Original thickness.

$C_3, C_4, C_5, C'_3, C'_4, C'_5$: material constants.

4.4.2 Proposed new edge fracture criterion

The experimental and theoretical results shown in earlier sections indicate that the edge crack is initiated from the top-edge (tool non-contacting side), and after crack initiation there is limited further edge stretching (hole expanding) to reach a through-thickness crack. In addition, the stress state for the shear edge under stretching is similar to the uniaxial tension stress state, so the HER should have close correlation to the material's total elongation, and the amount of hole expansion at the crack initiation should have a close correlation to the material's UE before necking. Based on these arguments and also considered the previous criteria in the literature, a new edge fracture criterion, Eq.(4.5), with the consideration of critical microstructure parameters.

Here HER is assumed linear related the material's total elongation (e_t):

$$HER = C_6 e_t + C_7 + C_D \quad (4.5)$$

e_t : total elongation (TE).

C_6, C_7 : material constants.

C_D : a factor describing damage evolution process after uniform deformation, with the consideration of microstructure effects, namely to consider C_D is a function about $V_M\%$, H_M , and H_F , as shown in Eq.(4.6).

$$C_D = f(V_M\%, H_M, H_F) \quad (4.6)$$

$V_M\%$: martensite volume fraction.

H_M : hardness of martensite.

H_F : hardness of ferrite.

The proposed criterion doesn't include the plastic strain ratio (r-value) or work-hardening rate (n-value) as used in the previous criteria, but added an addition term C_D to address the effects of microstructure characteristics of steels. The reasons for using criterion (4.5):

1. The thinning (or necking) phenomenon were not very obvious for DP780 and DP980 in hole expanding process.

2. The previous criteria (given in Eqs.4.2, 4.3, and 4.4) are for steels with relatively large e_t but lower strength as compared with the DP steels studied in this dissertation.

3. In Eq.(4.5), " $C_6e_t + C_7$ " is the pseudo-uniform deformation portion of hole expanding process, assuming " $C_6e_t + C_7$ " is linearly correlated to e_u in uniaxial tensile test.

4. In Eq.(4.5), C_D is the pseudo-nonuniform deformation portion of hole expanding process. In this process, effects of crack initiation, propagation, and plastic deformation entangling together causing material deteriorating until fracture. Assuming C_D is a function about $V_M\%$, H_M , and H_F , because these data are easily available form lab testing or in open accessed literature.

The criterion can be used to predict DP steels processed with the same conditions, i.e. clearance, hole diameter, thickness; same material code, DP780 and DP980; but from different suppliers, Supplier 1 (S1) and Supplier 2 (S2). To achieve this task the material parameters in the proposed criterion need to be tuned or fitting to the obtained experimental data.

There are two approached to obtain values of C_6 , C_7 , and C_D in Eq. (4.5), as listed in following

The first approach to fit values of C_6 , C_7 , and C_D in Eq.(4.5), assuming uniform deformation portion in HER equals to e_u in tensile test.

Step 1: Using formula $e_u = C_6 \times e_t + C_7$ to determine values of coefficients C_6 , C_7 for DP780 and DP980. e_u and e_t are values of UE and TE obtained from tensile stress-strain curves, green lines in Table 4-6.

Step 2: Obtaining averaged HER of different initial hole diameters, named as AVG, blue lines in Table 4-6.

Step 3: Using formula $C_D = AVG - e_u$ to obtain C_D values.

The second approach to fit values of C_6 , C_7 , and C_D in Eq.(4.5), assuming the ratio of (uniform deformation)/(nonuniform deformation) in HER is the same as in tensile test.

Step 1: Obtaining averaged HER of different initial hole diameters.

Step 2: Using the formula equivalent averaged uniform elongation= $HER \times (e_u/e_t)$ to obtain equivalent averaged HER values, named as AVG2, red lines in Table 4-6.

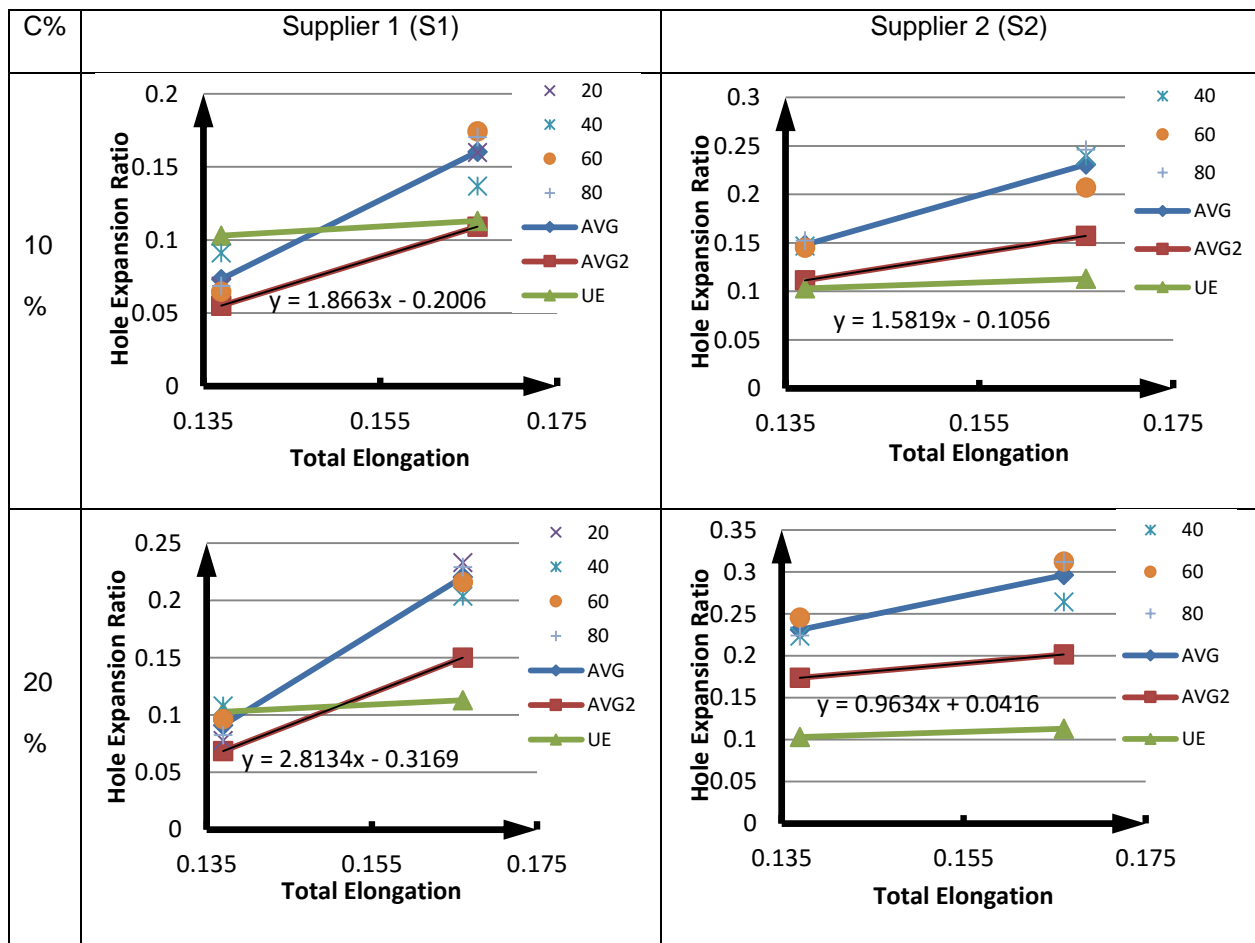
Step 3: Using formula: $AVG2 = C_6 \times e_t + C_7$, to determine values of coefficients C_6 , C_7 .

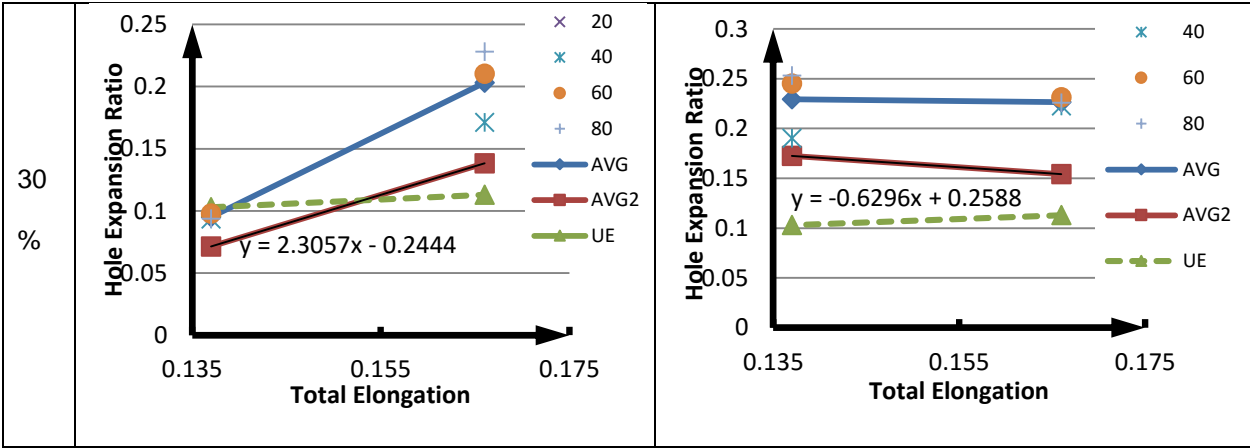
Step 4: Determining C_D values using formula: $HER \times (1 - e_u/e_t)$.

In real case, due to the differences in manufacturing processes, steels with the same grade number but from different suppliers showed different e_t values and e_u values. For tensile test results are not available, here assuming DP780 and DP980 from two suppliers with the same e_t values and e_u values.

Fitted lines are showed in Table 4-6.

Table 4-6 Data analysis of HER for DP780 and DP980 from two suppliers





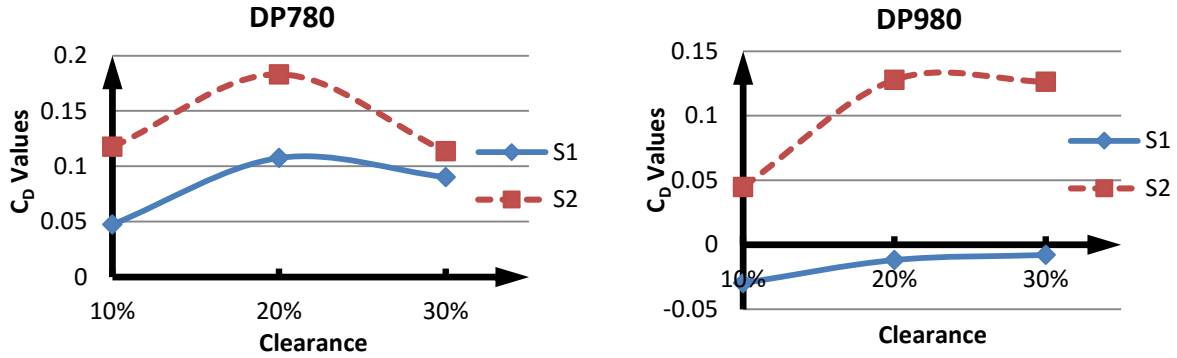
In Table 4-6, blue lines are values of averaged HER (denoted by AVG) of samples with initial hole diameters, d_o , equal to 20, 40, 60, and 80; green lines are e_t values of DP780 and DP980; red lines are equivalent uniform HER (AVG2), which equal to average HER values multiply by the ratio of e_u/e_t , which is uniform elongation divided by total elongation. Trend line formulas of AVG2 are as presented in Table 4-6. In practice, these experimental obtained values can be set as forming limits for DP780 and DP980.

Using the first approach to fit data, the equation of UE is expressed as $y=0.35x+0.06$, $C_6=0.35$ and $C_7=0.06$, C_D values of Eq. (4.5) are listed in Table 4-7.

Table 4-7 C_D values for DP780 and DP980 from two suppliers

C_D values		10%	20%	30%
S1	DP780	0.047427	0.107514	0.090231
	DP980	-0.02973	-0.01186	-0.00793
S2	DP780	0.117699	0.183065	0.113593
	DP980	0.044861	0.127903	0.126449

Plotting C_D values of DP780 and DP980 listed in Table 4-7 in Figure 4-15 (a) and Figure 4-15 (b).

(a) C_D values of DP780 from two suppliers(b) C_D values of DP980 from two suppliersFigure 4-15 C_D values for DP780 and DP980 from two suppliers

In Figure 4-15, assuming the deformation after the UE is the damage evolution process, higher C_D value means the higher HER values, also means longer damage evolution process or larger damage tolerance in test. The negative C_D value in case of DP980, is due to damage in the punching process, which lead to the values of HER less than UE or punching process put a negative effect on the HE test results. It can found for DP980, Supplier 1 case, HER value are less than UE values; while for other cases, HER values are greater than UE values. In application, because of this phenomenon, metal sheets of DP980 from Supplier 1 may fail at a strain lower than expectation in forming process.

4.5 Conclusions

By analyzing hole expanding process of DP780 and DP980, following conclusions were obtained:

1. For the hole expanding process, a crack first initiates at the top side of sheared edge, then propagate simultaneously on the sheared edge and (in the radial direction) on the metal sheet surface, finally form a through-thickness crack.
2. Clearance in punching process affects the HE test results; and among $C\%=10\%$, 20% , and 30% conditions, $C\%=20\%$ is the optimal condition for punching process for DP780 and DP980 in this dissertation.
3. DP steels from different suppliers show different ductile fracture surface morphologies different degrees of ductility at microscale, upon observing edge cracks using SEM.
4. Different fracture mechanisms of sheared edges lead to different HER. The initiation of multiple cracks on the sheared edge postponing the formation of the main crack and increasing HER.

CHAPTER 5 ANALYSIS OF MICROSTRUCTURE EFFECTS ON PLASTICITY AND FAILURE OF DP STEELS

In Chapter 4, an empirical failure criterion, Equation (4.5), was proposed. The parameters in the failure criterion includes martensite volume fraction and constituent phase properties, which are characteristic parameters of microstructures of DP steels. In this chapter, representative volume element (RVE) models are built to investigate the influence of these parameters on fracture mechanisms and tensile stress-strain relationships, especially for the damage evolution process, at mesoscale.

5.1 Literature review of effects of microstructures on stretchabilities of steel sheets

To research effects of microstructures on flangeabilities of steel sheets, Hyun et al. [79] investigated the differences in edge fracture behaviors of TRIP and Ferrite-Bainite duplex (F+B) steels. According to the research, edge fracture is mainly caused by localized necking under circumferential strain. When crack initiates on the surface of sheared edge, for TRIP steels, microcrack progressed in a branch shape, which does a suppressive role in formation and propagation of microcracks, while for F+B steel crack progressed in main direction uniformly. Due to the differences in microcrack progression, TRIP steel showed larger elongation but lower flangeability in comparing with F+B steel. Fang et al. [80] investigated the effects of the microstructure and chemical compositions on the hole expansion property of four C-Mn steels, which had been heat treated into different microstructures. According to the research, the higher difference between harder and softer microstructure the lower the hole expansion property. The higher strength of the soft matrix resulted in increased hole expansion ratio. A higher ratio of yield strength to ultimate tensile strength showed better hole expansion results. Hasegawa et al. [81] researched the relationship between microstructure and stretch-flange-formability of three types 980 MPa grade UHSS sheet, with either two ferrite/martensite dual-phase structures or a martensite single-phase structure, and got the following conclusions: 1. Microscopic plastic-flow or micro-void density generated by punching is not the dominant factor of the stretch-flange-formability of UHSS sheets. 2. Deep cracking resistance in punched surface is important to improve the stretch-flange-formability. 3. The strain gradient induced by hole punching is considered to be one of the reasons for the highest hole expanding ratio of the martensite single-phase steel. 4. During the hole expanding, for dual-phase steel in the case of low stretch-flange-formability, micro-cracks propagate mostly along the phase interfaces; in the case of high stretch-flange-formability, micro-

cracks tend to propagate through into ferrite or martensite phase. 5. The difference in hardness of ferrite and martensite is the dominant factor affecting the stretch-flange-formability of the dual-phase steel. 6. The volume fractions of phases also influence the formability.

According to research conducted by Lee et al. [82], strain-hardening rate can describe the effect of a hard constituent failure in sheared edge stretching, the greater the strain-hardening rate, the greater the deformation of ferrite relative to a hard constituent. Increasing the strain differential between ferrite and a hard constituent resulted in the increase in the rate of crack growth in the interface region. Levy and Van Tyne [83] used the strain-hardening rate at UE in a tensile test as the indicator of damage leading to failure in sheared edge stretching. According to data taken from other literature, it showed that the circumferential limit strain increases linearly with the decreasing strain-hardening rate at UE. The mentioned relationship applies to steels with a relatively soft ferrite and the following hard phases: angular or spherical carbides; pearlite; titanium carbonitride; bainite; and higher-carbon martensite. At the same strain-hardening rate, it was found that an increase in ferrite strength, such as a recovery-annealed product and lower carbon martensite in dual-phase or TRIP steels, resulted in improved circumferential limit strain. Levy et al. [84] considered the failure in fractured edge stretching as the result of a sequence of events: assumed cracking first develops in or adjacent to the martensite, then cracks grow in the interface between the martensite and ferrite. According to the research, it was found that in contrast to other studies, increased strength of the hard constituent retards crack initiation. Crack growth increased with increasing surface area of hard constituent-ferrite interfaces and increasing movement of ferrite relative to the hard constituent. According to the research conducted by Chung et al. [85], from an empirical argument, lower the strength difference between the matrix and the second phase tends to increase the hole expansion performance.

To investigate the effects of microstructures on crack morphologies of steels, Maire et al. [86, 87, 88] showed the method to quantify the evolution of damage using Non-destructive testing, and improved Rice and Tracey model using observed results of void nucleation and growth by X-ray microtomography. Al-Abbasi and Nemes [89, 90] developed a micromechanical model, aimed at capturing the mechanical behavior of DP steel. Constitutive behaviors of the constituents were obtained from literature, with the assumption that the deformation throughout the constituents are uniform, and the results of simulation and tensile test were compared and showed in good agreement. Sun et al. [91, 92] used microstructure-based

modeling approach to examine key factors influencing ductile failure of various grades of DP steels, and found that martensite volume fraction, 15% is a critical value: below it the ductility of DP steels is strongly dependent on the ductility of the ferrite matrix, while above it the overall ductility is mainly influenced by the mechanical property disparity between the two phases. Ramazani et al. [93] used in situ analysis of bending test in a large-chamber SEM (LC-SEM) combined with electron backscatter diffraction (EBSD) measurements in a conventional field-emission gun SEM (FEG-SEM), and conducted mini tensile test with DIC strain analysis, to investigate the failure initiation mechanisms of DP steel. According to the research, martensite cracking is the root cause of failure (or the crack initiation mechanism) for DP steel studied. Paul [94] used micromechanics based representative volume element (RVE) to predict the flow behavior, plastic strain localization, and plastic instability of DP steels. According to the research the microstructure inhomogeneity from various constituent phases can be the key factor influencing the final ductility of the DP steels under different loading conditions. Ductile failure of DP steels was predicted in the form of plastic strain localization without any prescribed damage/failure criteria for the individual phases in simulation.

5.2 Determination of input conditions for fracture analysis

Input conditions for fracture analysis of RVE model for DP steels, including $V_M\%$, strain hardening curves, and failure criteria of constituent phases.

5.2.1 Martensite volume fraction measurement for DP steels

Figure 5-1 is an image of typical grain structure of DP980, where the white areas are the martensite particles, and the dark areas are ferrite matrix.

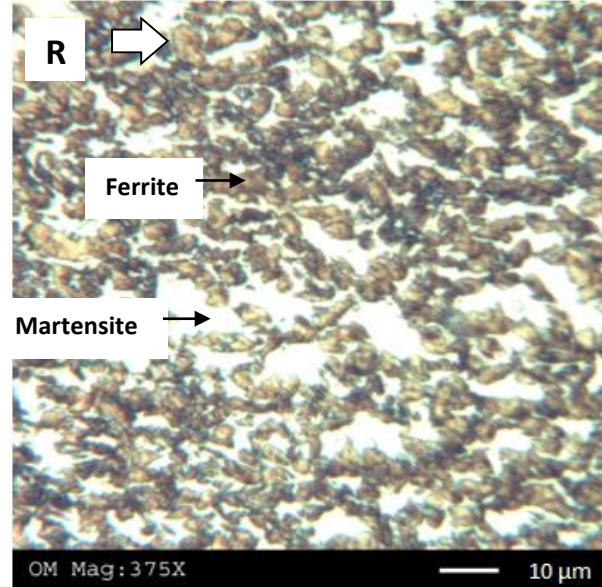
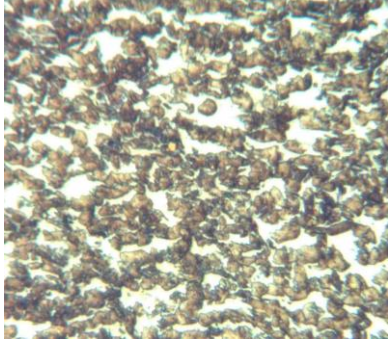

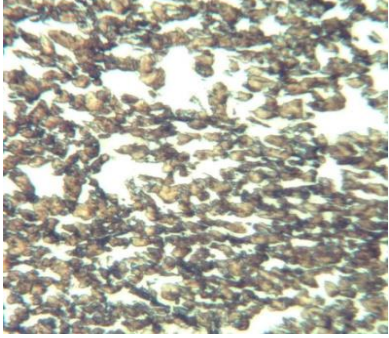

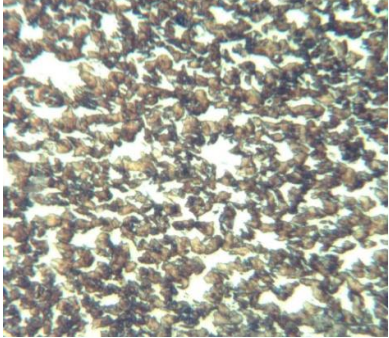
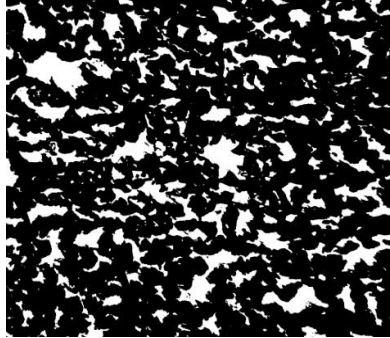


Figure 5-1 Typical grain structure image of DP980

In Figure 5-1, it can be observed that, martensite grains (white area) are different in shape and size. For a DP steel sheet, grain structures are different through the thickness. For images of grain structure at different thickness locations of a metal sheet, please reference Appendix G. The average martensite volume fraction used in the analysis of this chapter was obtained from three thickness locations and the measurement were performed after converting the micrographs into black/white images, and measured using an image processing software package “Image-Pro”, as shown in Table 5-1.

Table 5-1 Measurement of $V_M\%$ at different thickness locations

	a. Original	b. Black/White	Martensite $V_M\%$	Averaged $\langle V_M\% \rangle$
1			23.8%	26.3%

2			33%	
3			22.2%	

In Table 5-1, the value of martensite volume fraction ($V_M\%$) ranging from 22.2% to 33%, this variation means that $V_M\%$ is a value can roughly describing characters of grain structure images of DP steels studied. The averaged $V_M\%$ of these three locations is 26.3%. More details of steps of the measurement, please reference Appendix G.

It is worth mentioning that DP steels from different suppliers showed different grain structures, due to different manufacturing processing techniques, please reference Appendix H for more DP steel grain structure images.

The shape of single martensite grain vary with manufacturing process, chemical composition, thermal-mechanical condition, recrystallization, and post plastic. Figure 5-2 demonstrates the evolution processes of an original round shape grain, which ended up with three distinctly different grain shapes.

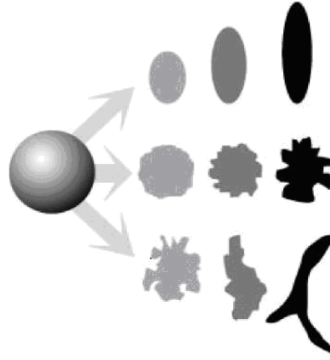


Figure 5-2 Three families of shapes originating from a circle with different thermomechanical histories [95]

In Figure 5-2, evolution process and results of an ideal sphere grain are demonstrated in an intuitive way. The grain shape evolution results include three families of shapes with significantly different geometries. In the top row, under stretching the circle changed into ellipses of various elongation. In the middle row, the edge of the circle deformed, grain shape evolved into shapes having various border irregularity. In the bottom a combination of loading conditions of previous two cases, the edge of the circle are changed and at the same time been stretched, the shape of the grain ended up with an irregular shape. In a real case, the evolution of grain structure is far more complex and influenced by multiple factors. In this dissertation, the current grain structure is of interest; the evolution process of grain structure is beyond research scope.

As summarized by Wojnar and Kurzydłowski [95], two main difficulties in shape quantification are: 1. lacking a precise, universal definition of the term for shape description. 2. A shape can't be described by a single number. In practice, to fully characterize a microstructure, four characteristics should be described, they are density, size, shape, and spatial distribution [96].

In this dissertation, to focus on investigating more general characters of DP steel grain structures, the specific shape of a grain structure is simplified as an element in the RVE model; the grain structure characteristic parameters of DP steels are reduced to one parameter, which is the martensite volume fraction, $V_M\%$; and martensite grains are randomly distributed in the ferrite matrix.

5.2.1 Input constituent phase properties from literature

According to experiments conducted by Nishimoto et al. [97] and Tsipouridis [102], the hardnesses of ferrite or martensite phases are not constant values. For a DP steel, after different thermal treatments, hardnesses of these two phases will be different from original ones.

In Table 5-2 are hardnesses of martensite and ferrite phases in three DP steels after different thermal treatments. 1.5 Mn-V and 2.1 Mn steels were heated to 850°C, kept for 90 seconds, then cooled in air to room temperature; 0.5 Mn-P steel was heated to 850°C, kept 90 seconds, then be water quenched to 250°C, kept 2 minutes, finally cooled in air [97].

Table 5-2 Vicker's Hardnesses of ferrite and martensite in DP steels with different annealing cycles [97]

1.5 Mn-V	2.1 Mn	0.5 Mn-P
HV _M : $\bar{x}=684$ $\sigma=83$	HV _M : $\bar{x}=405$ $\sigma=65$	HV _M : $\bar{x}=307$ $\sigma=22$
HV _F : $\bar{x}=125$ $\sigma=1$	HV _F : $\bar{x}=127$ $\sigma=4$	HV _F : $\bar{x}=144$ $\sigma=4$
HV _M / HV _F = 5.5	HV _M / HV _F = 3.2	HV _M / HV _F = 2.1

In Table 5-2 ratios of hardnesses of martensite and ferrite are presented. Based on Figure 5-4 and Table 5-2, it can be speculated that thermal treatment will change not only hardnesses but also ductilities and toughnesses of martensite and ferrite, and this qualitative guess is used to guide the determining of properties of constituent phases in modeling of RVE models.

There are two approaches were used to identify the mechanical properties of constituent phases of DP steels:

The first approach is based on dislocation theory to estimate properties of ferrite and martensite phases.

Uthaisangsuk [71] cited work by Bergström [98] and Rodriguez [99], , defined the isotropic flow behavior of two phases according the following formulas:

$$\sigma = \sigma_0 + \Delta\sigma + \alpha \times M \times \mu \times \sqrt{b} \times \sqrt{\frac{1 - \exp(-M \cdot k \cdot \epsilon)}{k \cdot L}} \quad (5.1)$$

σ_0 : yield strength, $\sigma_0 = 77 + 80\%Mn + 750\%P + 60\%Si + 80\%Cu + 45\%Ni + 60\%Cr + 11\%Mo + 5000N_{ss}$.

$\Delta\sigma$: additional strength caused by precipitation and carbon in solution.

α : a constant, $\alpha = 0.33$.

M : Taylor factor, $M=3$.

μ : the shear modulus, $\mu=80,000$ MPa.

b : the Burger's Vector, $b = 2.5 \times 10^{-10}$ m.

L : the dislocation mean free path.

k : the indication of the recovery rate.

For each phase, three parameters are different, values were taken from articles by Rodriguez [99] and Thomser [100], as shown in Table 5-3.

Table 5-3 Parameters for ferrite and martensite phases

	$\Delta\sigma$	$L(m)$	k
Ferrite	$5000 \times C_{SS}^F$	d_a	$10^{-5}/d_a$
Martensite	$3065 \times C_{SS}^M - 161$	3.8×10^{-8}	41

C_{SS}^F , C_{SS}^M : the carbon content in ferrite and martensite. The carbon contents were calculated according to the mass balance and the phase fraction.

d_a : the ferrite mean linear intercept, which is related to the grain size of ferrite.

The second approach is mainly through experiment to estimate properties of ferrite and martensite phases.

Sun [91] assumed plastic flow stresses for ferrite and martensite phases to satisfy the following laws:

$$\sigma_0 = \sigma_{y,F} + K_F \varepsilon_{ep}^{n_F} \quad (5.2)$$

$$\sigma_0 = \sigma_{y,M} + K_M \varepsilon_{ep} \quad (5.3)$$

$\sigma_{y,F}$ and $\sigma_{y,M}$: are the initial yield strengths of ferrite and martensite phases.

K_F and K_M : are the hardening coefficients of ferrite and martensite phases.

n_F : are the hardening exponent of the ferrite phase.

Parameters of ferrite phase in Eq. (5.2) were determined by the experiment using in situ high-energy X-ray diffraction, $\sigma_{y,F}=425$ MPa, $K_F=940$ MPa, $n_F=0.2$. The mechanical property data for the martensite phase are from literature by Sakaki [101], $\sigma_{y,M}=1180$ MPa, $K_M=1740$ MPa.

In this dissertation, properties of constituent phases are determined based on data in reviewed two approaches but with some modified, to make it is easier to study the influence of martensite phase

properties on the model. Two strain hardening curves represent the properties of hard martensite phase (red color) and softer ferrite phase (blue color), respectively, are presented in Figure 5-3.

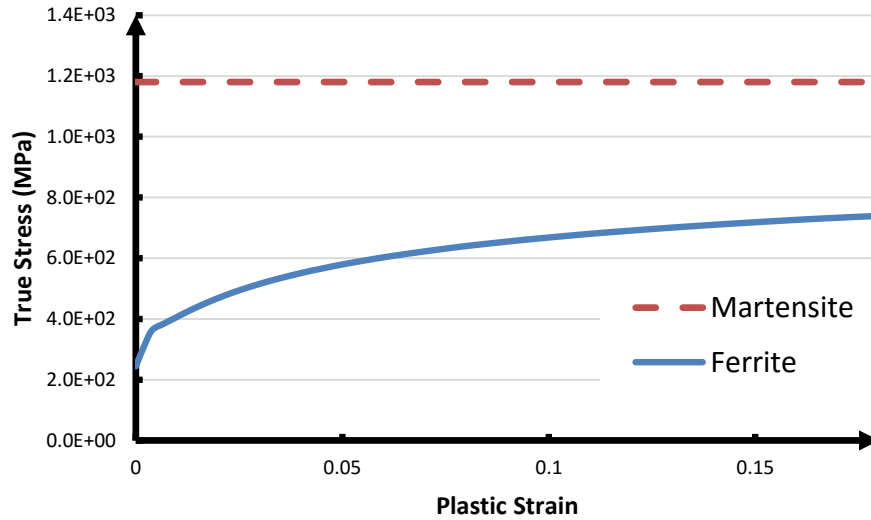


Figure 5-3 Strain hardening curves of martensite and ferrite

Figure 5-3, martensite is assumed to be perfectly plastic in plastic deformation, the constitutive relation of ferrite phase in plastic deformation is based on experiment conducted by Sun [91].

In this dissertation, the failure process of ferrite are described using GTN model, as discussed in Chapter 2.3.2, parameters of this model were listed in Table 5-4.

Table 5-4 GTN model failure related parameters for ferrite

	q_1	q_2	q_3	ε_N	S_N	f_N	f_c	f_F
Ferrite	1.5	1	2.25	0.16	0.01	0.4	0.29	0.3

Ductile damage model are applied to describing the failure process of martensite phase, for the model damage initiation strain is 0.09; displacement for damage evolution process is 0.001, the parameter is 20 for exponential form damage evolution law, for details of this model please reference Appendix E.

5.3 The effects of microstructures on fracture of DP steels

According to experimental observation and FE simulation, microstructure influence the fracture mechanism and morphologies of cracks of DP steels.

5.3.1 Effects of microstructures on the crack initiation and propagation

The fracture model in this dissertation is based on the experimental observed fracture mechanism for dual phase steel by Prodromos [102], as shown in Figure 5-4 for a tension fractured area of a DP steel, where the white particles are martensite particles, the brown areas are ferrite matrix, black particles are nucleated voids.

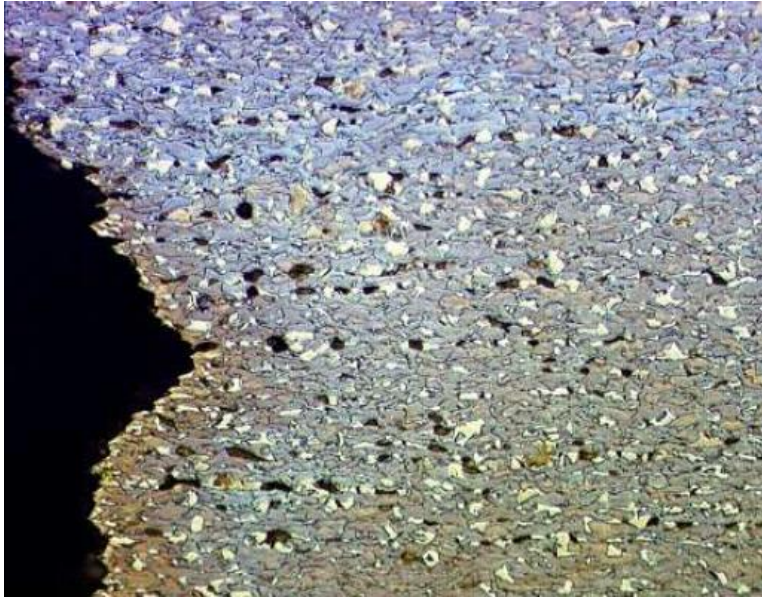


Figure 5-4 Tensile fracture area of a DP steel [102]

In Figure 5-4, observing microstructure close to tensile fractured area, it can be seen that the density of the cavities (the black spots) is high near the fractured edge, this phenomenon suggesting that the failure of researched DP steel is due to void nucleation, growth, and coalescence, which related to the non-uniform microstructure with contrasting constituent phase properties that causing stress concentration and strain localization. This fracture mechanism also agrees with the experimental observation as shown in Figure 4-13 (in section 4.3.3) for the current DP steels under investigation. Furthermore, it can be observed that most voids are caused by detaching boundaries between martensite particles and ferrite matrix, or splitting of martensite particles.

Figure 5-5 shows the crack propagation path in a DP steel. The island shape light color areas are martensite particles, and the rest area is the ferrite matrix.

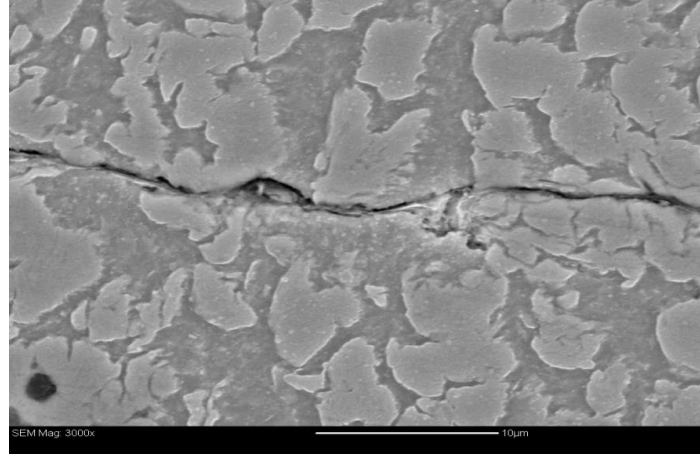


Figure 5-5 Crack propagation in a DP steel

According to Figure 5-5, it can be deduced that martensite particle influence the propagation of crack within ferrite matrix.

An FE model was built to demonstrate the influence of a harder inclusion on the crack propagation path within softer matrix, as shown in Figure 5-6 [103].

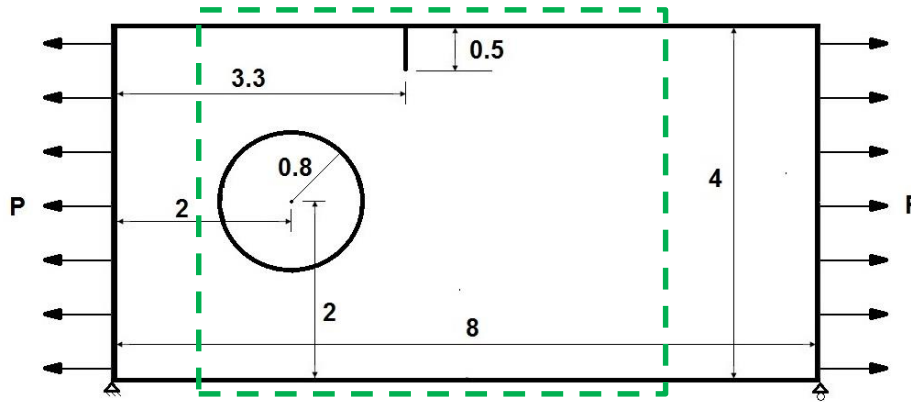
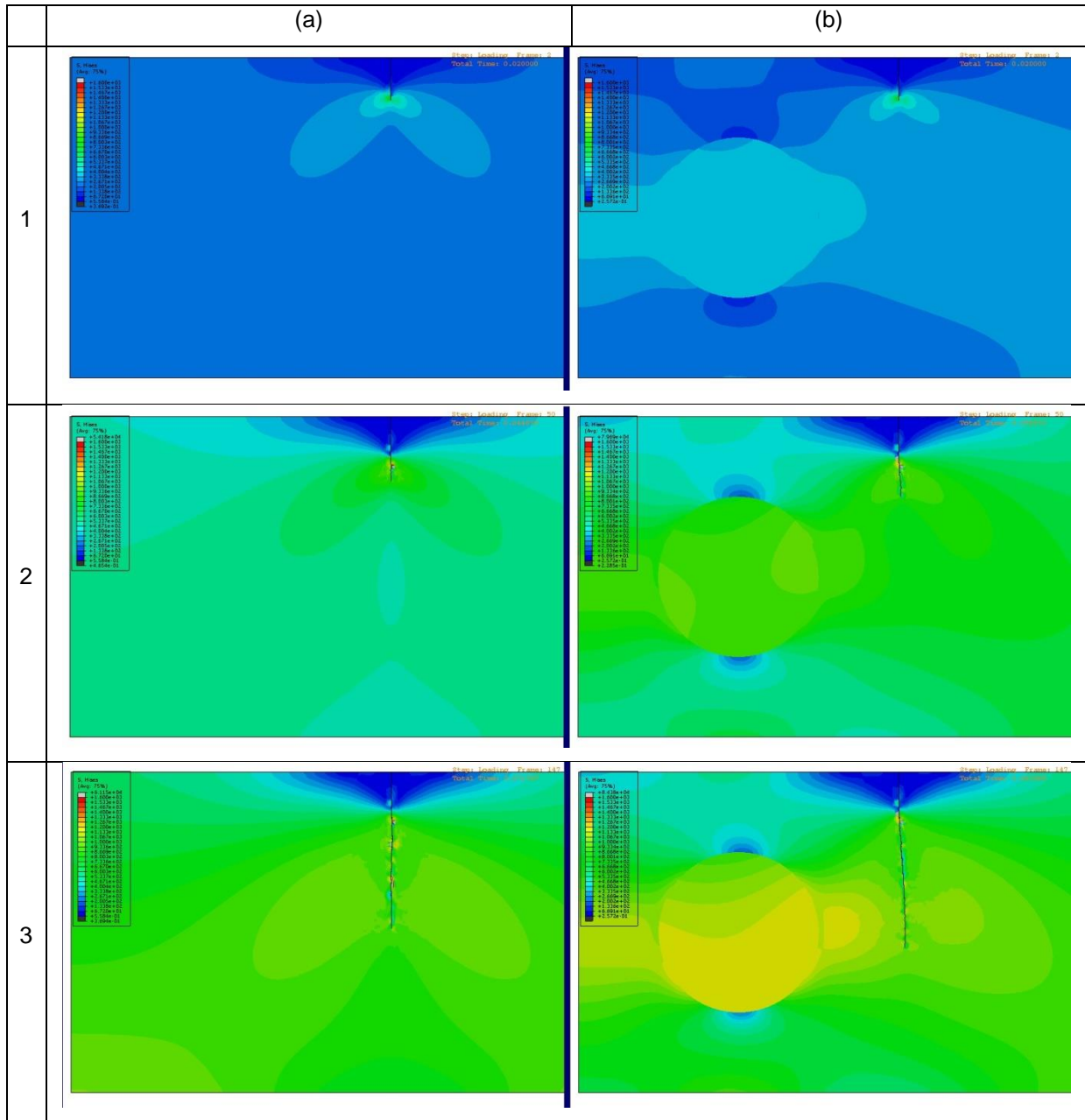


Figure 5-6 Sketch of heterogeneous model with one hard inclusion

In Figure 5-6, two sides of the model are stretching with pressure equals to 800, the left lower corner of the model is fully constrained, y-direction movement of the right lower corner is constrained. The inclusion and matrix are different in Young's modules. For the ferrite phase, the damage initiation criterion is value maximum principal stress equals to 1000; damage evolution is energy type, value of fracture energy equals to 50. For martensite particle, no failure criterion was assigned.

Table 5-5, the crack propagation process are simulated with homogeneous model, column (a), and heterogeneous model, column (b), to study the effects of harder inclusion on crack propagation path.

Table 5-5 Simulated crack propagation paths in homogeneous and heterogeneous models



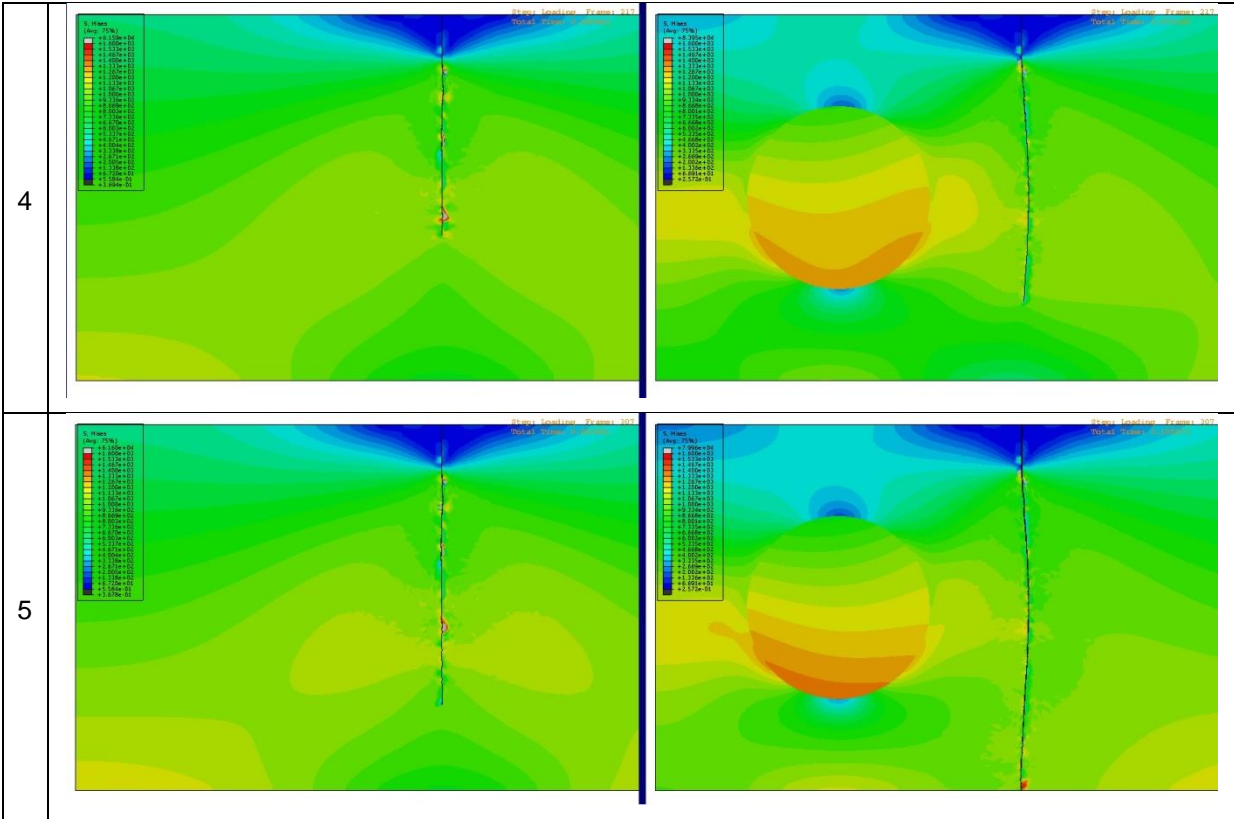


Table 5-5, column (a), the crack path in the homogeneous model is a straight line, the crack path is curved line in the heterogeneous model, as shown in column (b), it can be said the harder inclusion influenced the crack propagation path. Comparing column (a) and (b), row 1 to 5, it can be observed stress distribution for two models are different, for the homogeneous model, stress distribution at two sides of the crack is symmetry, while for heterogeneous mode, the stress distribution is influenced by the hard inclusion.

Observed phenomenon and simulation results can be summarized as, crack propagation path in dual phase steel is determined by the balance of the strengths of martensite particles and ferrite matrix.

5.3.2 Microstructure-based representative volume element (RVE) models of DP steels

Based on literature review and experimental investigation, the heterogeneous representative volume element (RVE) model of DP steels were built, pre-assumptions and features of the model are summarized in below:

1. The volume fraction of martensite was determined based on measured data of metallographic images of DP steels.

2. Martensite particles were randomly distributed in the ferrite matrix, the geometry of a single martensite particle is cubic.

3. The ferrite and martensite phase properties were estimated based on data from literature; martensite phase was simplified as perfectly plastic; GTN damage model was applied to the ferrite phase and ductile damage model was applied to the martensite phase.

Figure 5-7 is the sketch of the RVE model, which was modeled in ABAQUS.

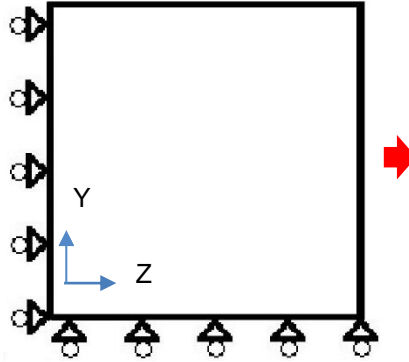


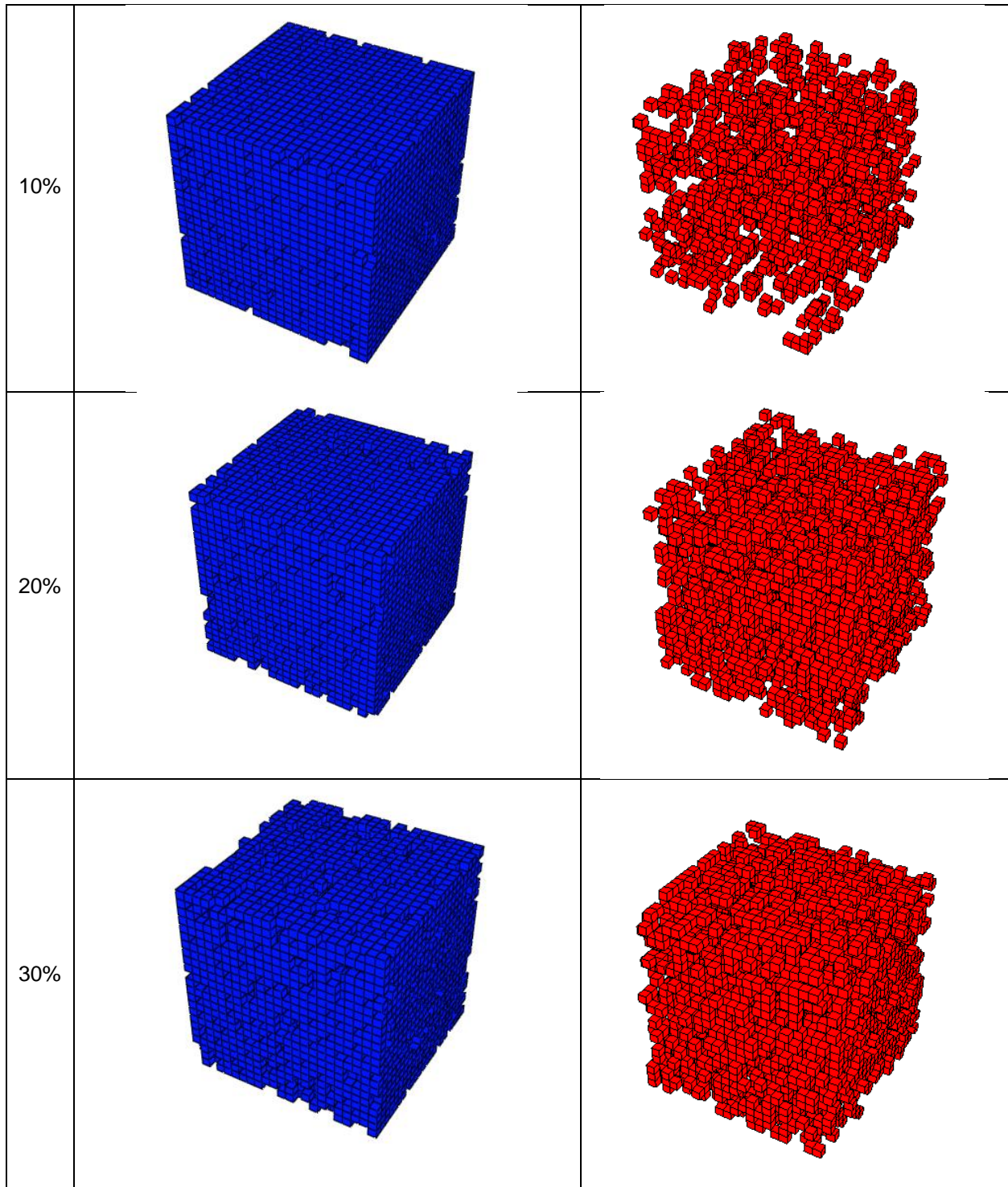
Figure 5-7 Sketch of RVE model

As shown in Figure 5-7, the geometry of the model is a cube, with 0.1mm edge length, three interconnected surfaces of the cube were constrained with displacement in X, Y, and Z directions, respectively; the surface (without constraint) perpendicular to Z direction was applied a displacement controlled movement.

To investigate the effects of martensite volume fraction ($V_M\%$) on fracture morphologies and mechanical properties of DP steels, RVE models with $V_M\%=10\%$, 20% , and 30% were built. RVE models consists of two groups quad elements with different properties, represent harder martensite inclusions and softer ferrite matrix, respectively. Blue color elements represent the ferrite matrix, red color elements represent martensite particles, as shown in Table 5-6.

Table 5-6 Ferrite and martensite phases in RVE models with different $V_M\%$

$V_M\%$	Ferrite Matrix	Martensite Particles
---------	----------------	----------------------

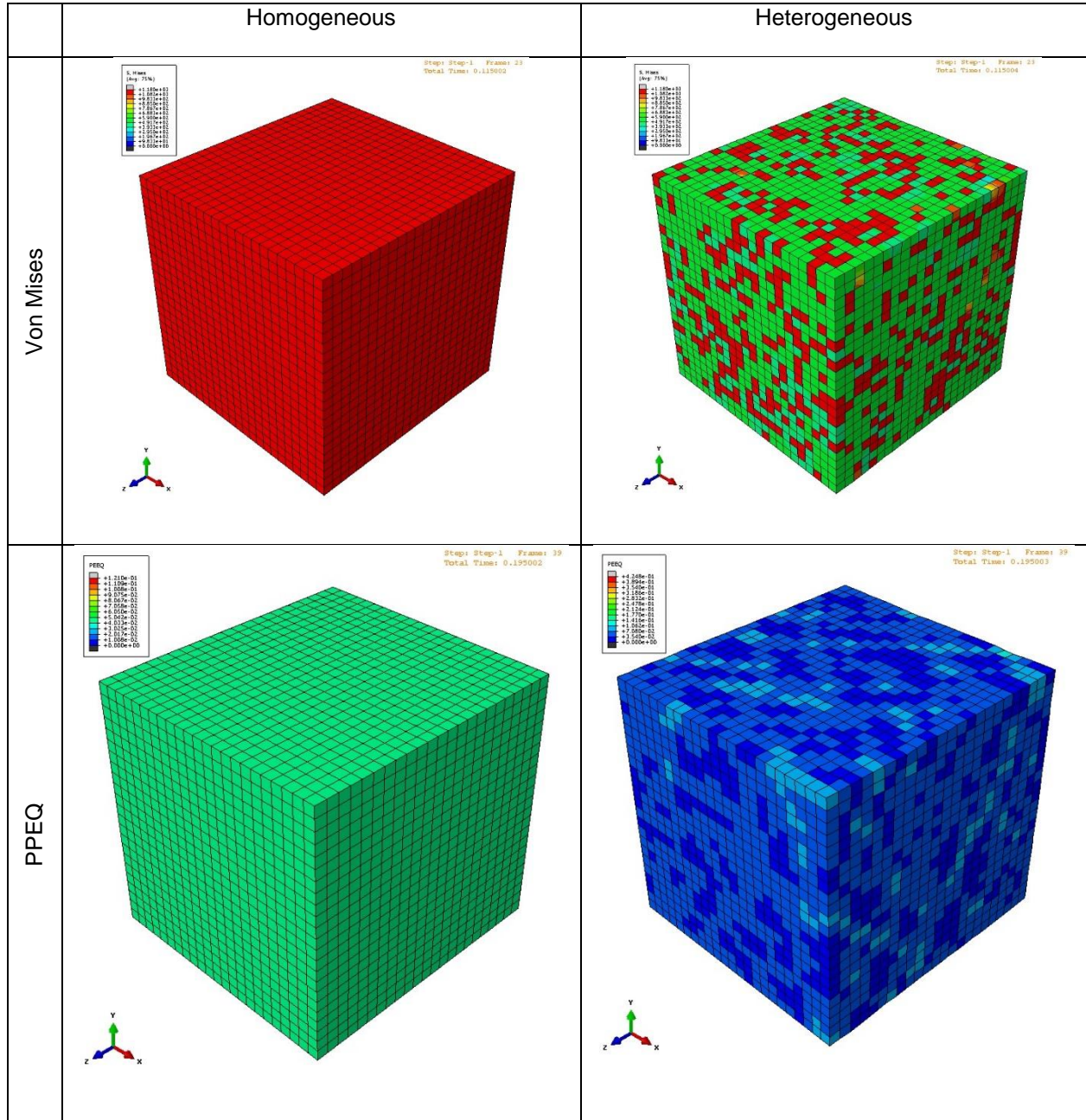


In Table 5-6, it can be observed, for the case $V_M\%=10\%$, particles in the RVE are separated from each other, when $V_M\%=30\%$, randomly distributed martensite particles connect to each other and form larger martensite islands with various shapes within ferrite matrix, in this case, although these martensite particles

seemed isolated upon observing a cross section (2D plane) of the RVE model, in 3D space have more chances to link with each other.

Table 5-7, row 1 and 2 are homogeneous and heterogeneous models. For these two models, Von Mises stress distribution and equivalent plastic strain distribution are compared.

Table 5-7 Stress and strain contours on outside surfaces of homogeneous and heterogeneous RVE models



According to Table 5-7, the Von Mises stress (row 1) and PEEQ (and 2) distributions in homogeneous model are uniform while in the heterogeneous model stress and strain distributions are discrete and obviously influenced by the existence of martensite, and martensite phase shows higher stress but lower strain.

In Figure 5-8, cracks on outside surfaces of homogeneous and heterogeneous models are presented.

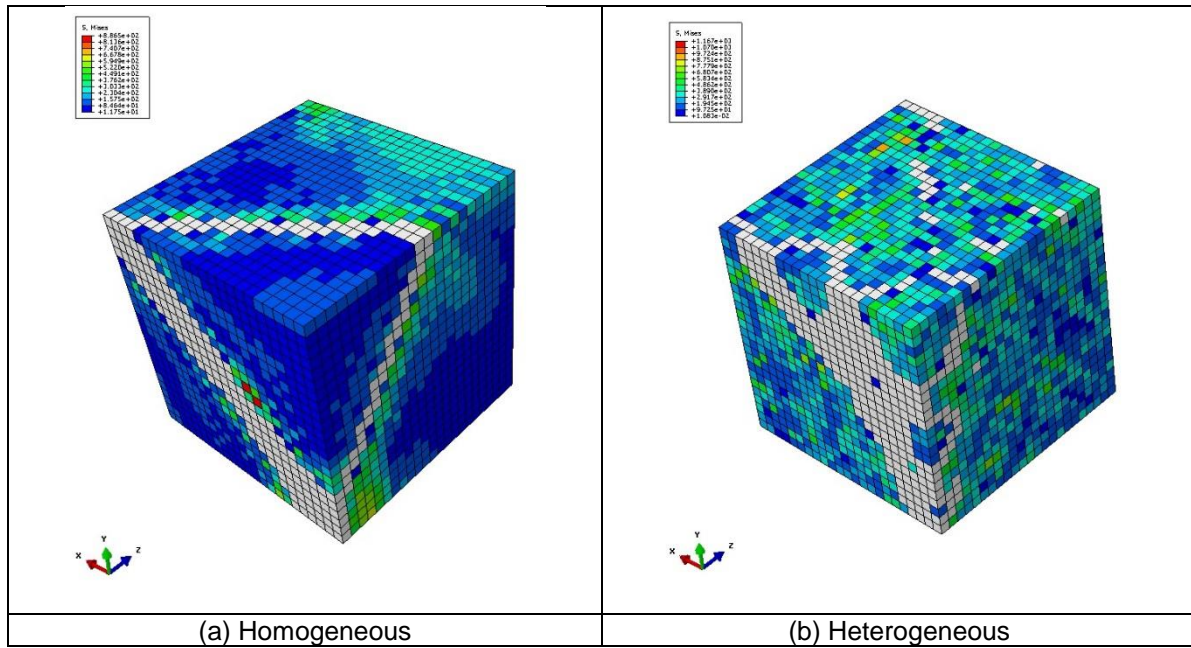


Figure 5-8 Failed elements on outside surface of RVE

Figure 5-8, failed element in the model were assigned with white color, these failed elements composed cracks on outside surfaces of the RVE.

For failed element (or cracks) on the outside surfaces of homogeneous model, as showed in Figure 5-8 (a), are straight lines and showed certain symmetry, because symmetrical stress distribution within the model. While for the heterogeneous model, as showed in Figure 5-8 (b), no obvious pattern can be found for cracks on the outside surfaces, because the stress/strain distributions in the model are distorted by the randomly distributed martensite particles.

5.3.3 Effects of microstructures on fracture morphologies of RVE models

Cracks inside RVE models with $V_M\%$ =10%, 20%, and 30% as presented in Figure 5-9.

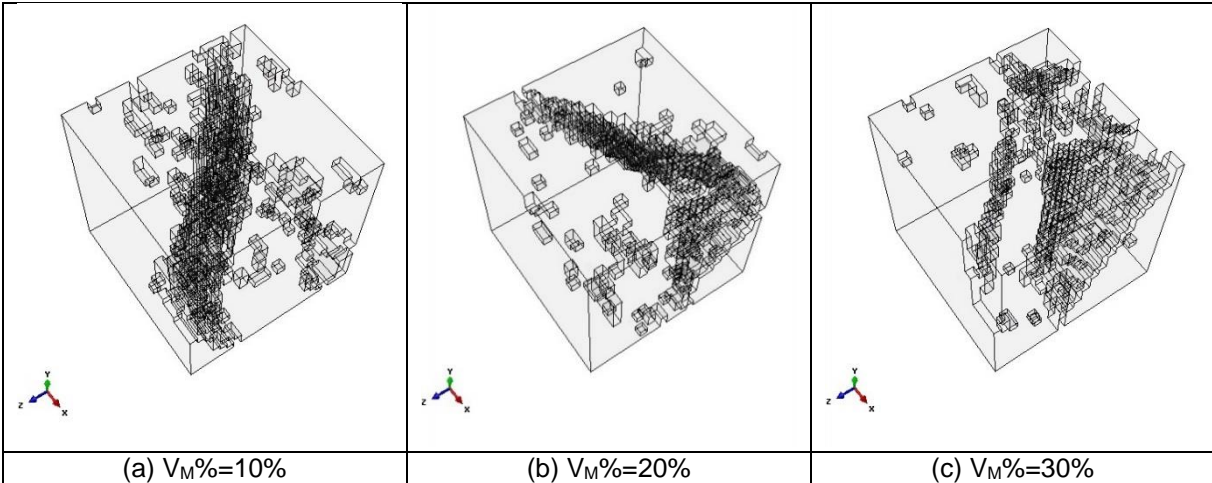
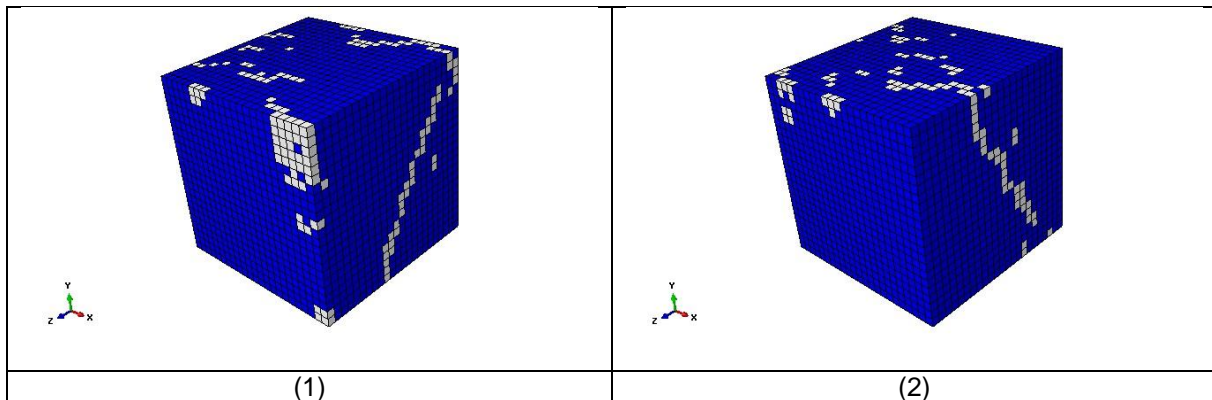


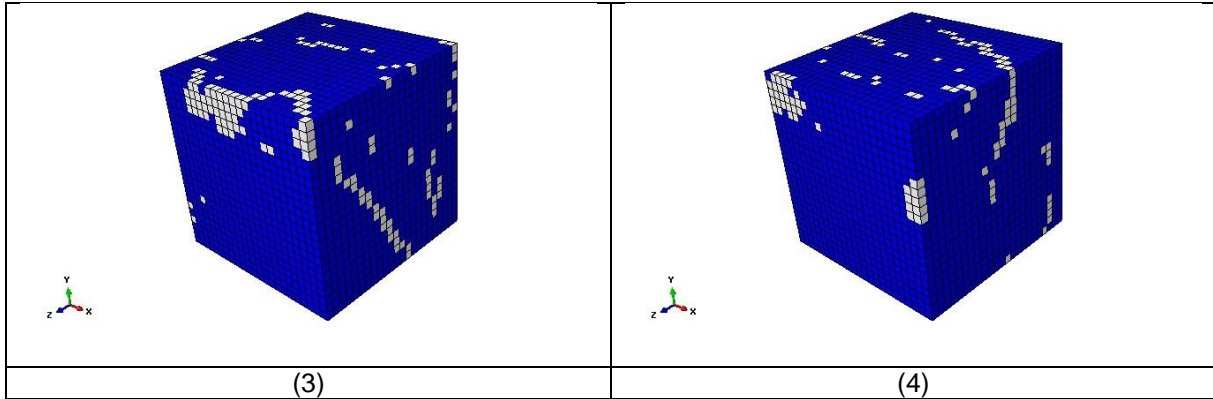
Figure 5-9 Crack initiation and propagation in heterogeneous RVE models with different martensite volume fractions

In Figure 5-9, failed elements were removed from the model and composed shades in the heterogeneous RVE. It can be observed, as the value of $V_M\%$ increases from 10% to 30%, morphologies of cracks are arbitrary and no obvious trend can be observed.

In Table 5-8 are four RVE models with $V_M\%=30\%$, the distribution of martensite particles in ferrite matrix are different, which were randomly generated.

Table 5-8 Cracks on outside surfaces of RVE with $V_M\%=30\%$ but different spatial (random) distributions





In Table 5-8, the cracks on the outside surfaces of RVE models shows random patterns.

Base on simulation results in Figure 5-9 and Table 5-8, it can be concluded that cracks randomly showed both inside and on the outside surfaces of the heterogeneous RVE, and cracks obviously were influenced by the stress/strain localization caused by the spatial distribution of martensite phase within ferrite matrix.

5.4 The effects of microstructures on constitutive relationships for DP steels

The effects of martensite volume fraction and properties of constituent phases on the stress-strain relationship of the RVE model are discussed in this section. In simulation, only martensite properties were changed and corresponding results were presented. The ductility and strength of ferrite obviously playing a determining effect on simulation result, for concise, the effects of ferrite properties will not be discussed.

5.4.1 Effect of martensite volume fraction

Stress-strain curves of RVE models with different $V_M\%$ =10%, 20%, and 30% are plotted in Figure 5-10.

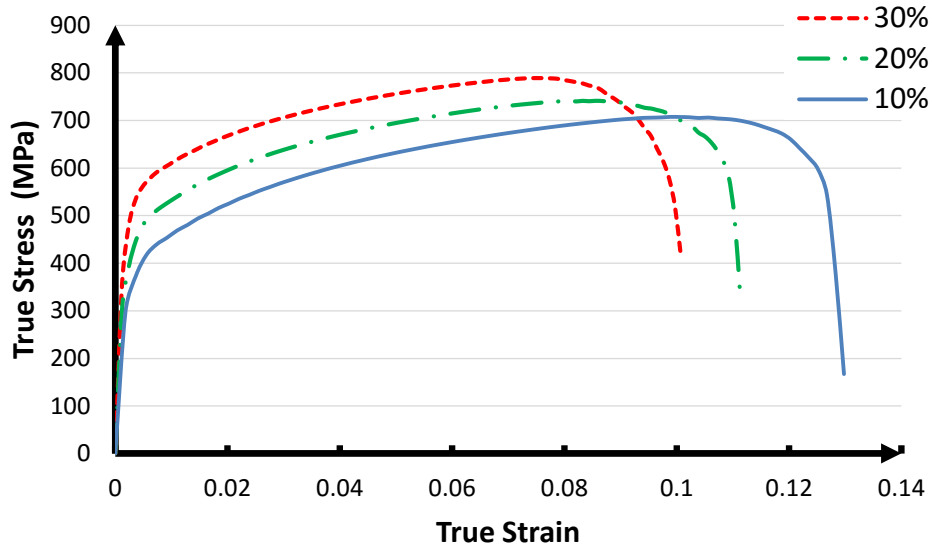


Figure 5-10 Stress-strain curves of RVE models with different martensite volume fraction

In Figure 5-10, it can be observed, as the increase of $V_M\%$, the strain hardening rate and ultimate tensile strength increase, but the total elongation (ductility) decreases. The phenomenon is due to the reduction of the volume of more ductile ferrite phase in the RVE model.

Figure 5-11, as $V_M\%$ increasing from 10% to 30%, the ultimate tensile strength (UTS) and damage initiation strain (DIS) are presented. Here damage initiation strain (DIS) is defined as the strain corresponding to UTS, for details please reference section 1.4.

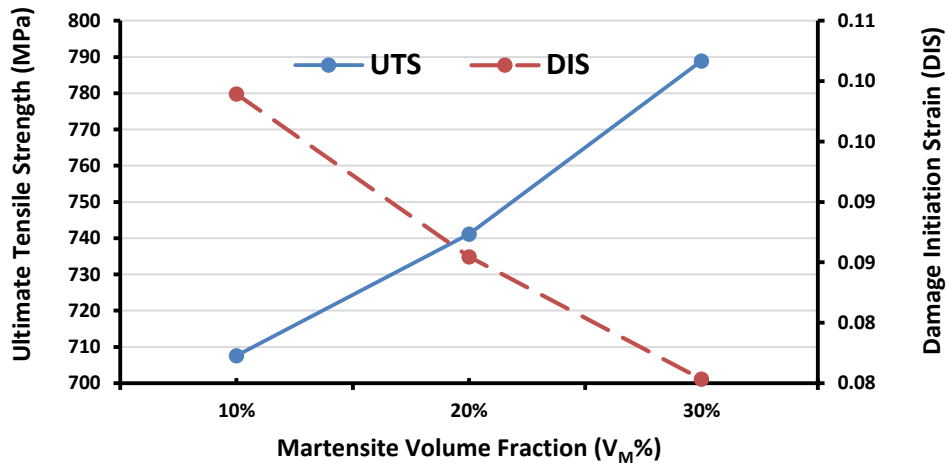


Figure 5-11 The effects of martensite volume fraction on ultimate tensile strength (UTS) and damage initiation strain (DIS)

In Figure 5-11, it can be observed as martensite volume fraction increases from 10% to 30%, UTS increases from 707.6 MPa to 788.9 MPa, an increase of 11.5%; DIS decreases from 0.0989 to 0.0753, a decrease of 23.9%.

Figure 5-12, the total energy (or external work to “split” the RVE) with respect to the martensite volume fraction (ranging from 10% to 30%) for the model are presented.

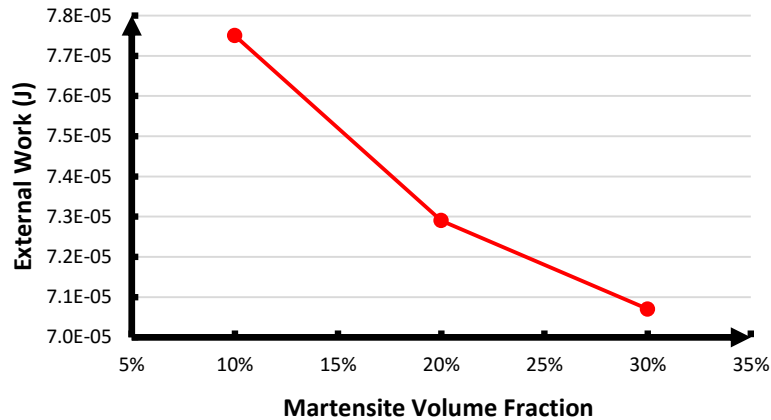


Figure 5-12 Total energy to split RVE models with different martensite volume fractions

In Figure 5-12, as $V_M\%$ increases from 10% to 30%, the external energy decreases from $7.75E-5$ mJ to $7.07E-5$ mJ, declined by 8.8%. This trend means that, with the increasing of $V_M\%$, the failure process of RVE model dissipates less energy, or to phase it another way, it consumes less energy (total/external work) to split the RVE.

Simulation results showed in Figure 5-10, Figure 5-11, and Figure 5-12 matches to the general relationship for grain structure and fracture toughness of DP steels: $V_M\%$ of DP980 is higher than DP780; DP980 is less ductile than DP780; (in most cases) HER of DP980s are less than DP780s.

5.4.2 Effect of martensite strength

Figure 5-13 are stress-strain curves of the same RVE model with different martensite strength, ranging from 1200 to 1800 MPa. It can be observed that, as the martensite strength increases, the strain hardening rate and ultimate tensile strength increase, but the total elongation (ductility) decreases.

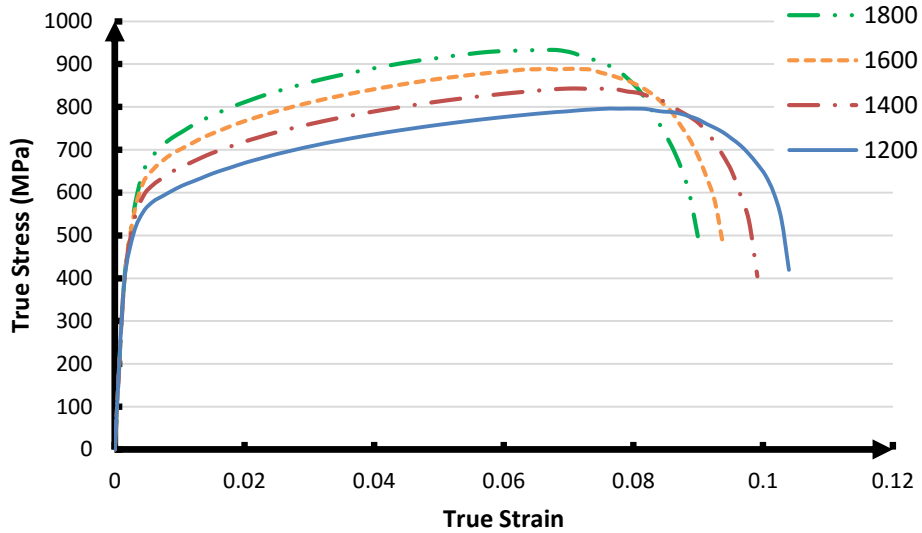


Figure 5-13 Stress-strain curves of the RVE model with different martensite strengths

Figure 5-14 demonstrates the variation of UTS and UE as the strength of martensite phase increases from 1200 to 1800 MPa. In this figure the only variable in the RVE models is the strength of martensite. It can be observed that as the martensite strength increases, UTS increases from 796.2 MPa to 933.6 MPa (17.3% increase), damage initiation strain (DIS) decreases from 0.0791 to 0.0652 (17.6% decrease).

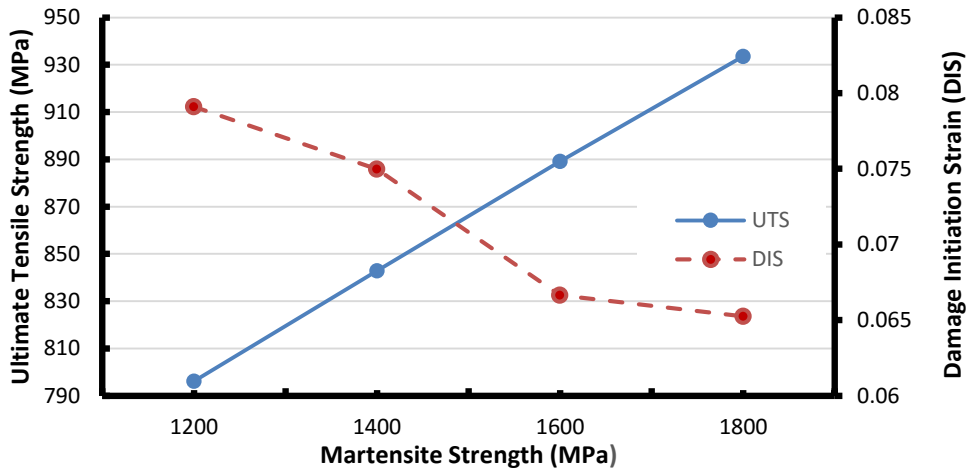


Figure 5-14 The effects of martensite strength on ultimate tensile strength (UTS) and damage initiation strain (DIS)

Figure 5-15 is the trend of external work of RVE model under tension. As martensite phase strength increases, external energy (to split the RVE) increase from 7.09E-5 mJ to 7.19E-5 mJ (1.4% increase).

The trend implies that, with the increase of martensite phase strength, the work to split the RVE model increases, although the percentage increase is not great.

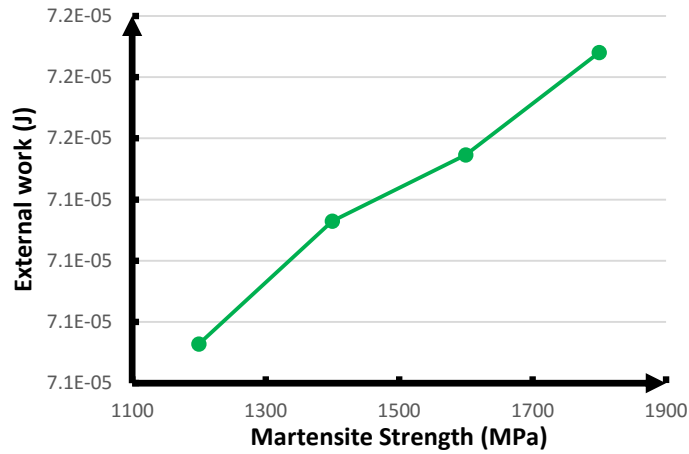


Figure 5-15 Total energy to split RVE models with different martensite strengths

5.4.3 Effect of martensite ductility

Figure 5-16 are stress-strain curves of RVE models for various martensite DIS from 0.06 to 0.09, for the model to describe martensite please reference 5.2.1 and Appendix E. In this figure, it can be observed that as the martensite damage initiation strain increases, both ductility and UTS increases, thus requiring more energy to “split” the RVE model.

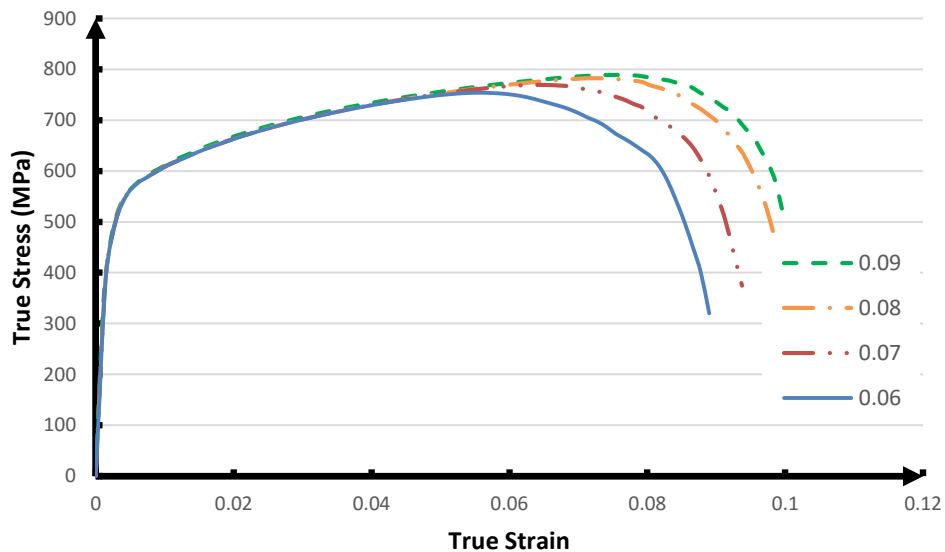


Figure 5-16 Stress-strain curves of RVE models with different martensite damage initiation strain

5.4.4 Effect of martensite spatial distribution

Figure 5-17 are stress-strain curves of RVE models, with the same $V_M\%=30\%$, distributions of the martensite particles are slightly different when the spatial locations of particles were randomly generated. It can be observed that these curves are almost identical until the onset of the apparent necking or damage initiation points, after DIS the stress-strain curves are different, which due to various local deformation fields and revealing the effect of martensite spatial distribution on stress-strain relationship for the RVE.

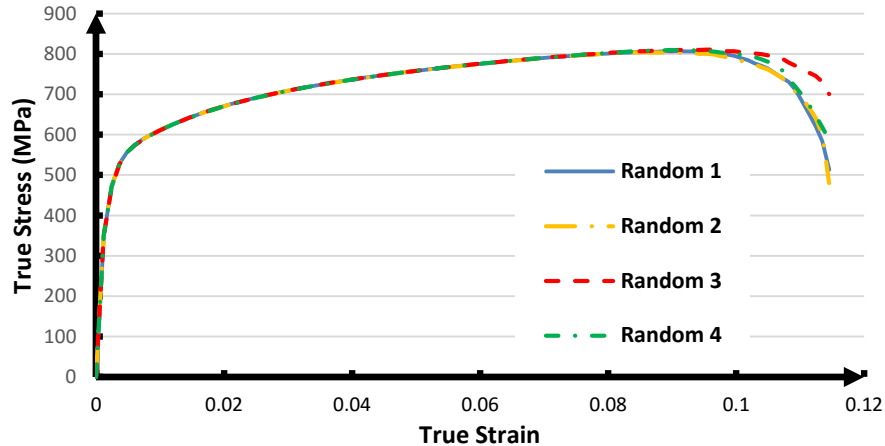


Figure 5-17 Stress-strain curves of RVE models with $V_M\%=30\%$ but different spatial (random) distributions

5.5 Discussions

According to literature view, the properties of martensite and ferrite phases are not constant for DP steels but vary from different chemical composition and material processes. The failure mechanism of DP steels in this dissertation was based on void nucleation, growth, coalescence. The properties of martensite particles influence the crack propagation path within the ferrite matrix.

The effects of volume fraction, strength, ductility, and distribution of martensite phase on the constitutive relationships and crack morphologies of RVE models were investigated through FEA.

According to the simulation, the following microstructure effects may appear in the predictions of RVE models:

1. As the martensite volume fraction increases from 10% to 30%, the martensite particles in the ferrite matrix have more chance to link with each other, forming larger phase particles of various shapes, or even

from isolated phase particles to be 3D networks that can significantly change the overall mechanical behavior;

2. As the martensite volume fraction increases, strain hardening rate (n-value) and ultimate strength increase; ductility, damage initiation strain, and total energy to split the RVE decrease.

3. As the martensite phase strength increases, strain hardening rate and ultimate strength increase; damage initiation strain decreases; and different from the results of increasing of martensite volume fraction, total energy to split the RVE increases, although the increase is not significant.

4. As the martensite damage initiation strain increases, ductility, ultimate strength, and total energy to split the RVE increase.

5. Given the same martensite volume fraction but different martensite spatial distribution within ferrite matrix, variations can occur in damage deterioration processes (or non-uniform deformation processes) observation stress-strain curves; locations and morphologies of cracks (inside and on outside surfaces) of RVE models are different.

In practice, the mechanical property of a DP steel is determined by the balance of properties of constituent phases. For concise, the effects of ferrite properties on constitutive relationships were not discussed.

CHAPTER 6 CONCLUSIONS AND SUGGESTIONS FOR FUTURE WORK

The chapter states conclusions and recommendations for future research of edge fracture of DP steels.

6.1 Conclusions

In this dissertation, a variety of experimental and FEA methods were applied to analyze effects of processing and material parameters on fracture mechanisms of DP steels in punching and hole expanding processes. A criterion to predict edge fracture was proposed. This criterion includes microstructure features of DP steels. The heterogeneous microstructure of DP steels was built into the Representative Volume Element (RVE) model to study the effects of microstructure parameters and fracture mechanisms on macroscale mechanical properties of DP steels, with damage-based failure criteria applied to constituent ferrous and martensitic phases.

Following conclusions were obtained:

1. Among C%=10%, 20%, and 30% conditions, 20% is the optimum processing parameter for punching process, DP steel sheets processed under this condition showed the best stretchabilities.
2. In engineering application, by properly tune up processing parameters for a material, sheared edge geometries and hole expansion results can be obtained for process design and optimization.
3. Steel sheets from different suppliers showed different edge fracture behaviors in hole expanding process and different hole expansion test ratios.
4. At the macroscale, multiple crack initiation can release the stretching stress and delay the crack propagation for DP steels in hole expansion test. This explains the different hole expansion ratios of the materials from different suppliers.
5. Both continuum and mesoscale micromechanics FEA models have been performed based on the fracture mechanism of void nucleation, growth, and coalescence, and the effects of microstructure on crack initiation and propagation of several DP steels are obtained. The simulation results can explain the experimental observations.

6.2 Future research

To further research in this topic, improvements can be made in the following aspects:

1. In this dissertation, hole punching and expanding processes were simulated in two separate models, the influence of hole punching process were not included in simulating hole expanding process. To

integrate two simulations into one model with two steps might increase the accuracy of simulation results, although costing in computing and the model complexity will increase.

2. Fracture related simulations used ABAQUS damage evolution law to describe the material weakening process. For this process, a more detailed damage evolution law for the void nucleation, growth, and coalescence processes, or a stochastic way to define the material deterioration process is needed. Experimental techniques to accurately measure the initiation of damage for DP steels are recommended for further study in similar topics.

3. The influence of microstructures at mesoscale was researched using local approach. The Non-local approach at macroscale is another approach to search fracture phenomenon. Providing more powerful computer, micro or atomicscale simulation of fracture process of DP steels is another approach.

4. The meso and macroscale phenomena were discussed separately in this dissertation, an approach linking them together seamless is in demand.

APPENDIX A

Table A.1 Properties of DP steels (provided by a US automaker)

Sample (L)	Thickness (mm)	Peak Stress (MPa)	.2% OY (MPa)	% UE	% TE	n ¹ Value	n ² Value	r- Value
DP600 GA	1.02	621	354	16.4	24.4	0.20	0.16	0.90
DP780 GA	1.03	873	503	11.0	14.6	0.15	0.11	1.15
DP980 GA	1.03	1055	621	8.3	11.3	0.10	*	0.82
DP980 CR	1.04	1138	668	7.0	10.8	0.08	*	1.12
TRIP780 GA	1.09	764	447	23.6	28.7	0.28	0.24	0.80
HSLA50GI	1.04	446	358	19.2	26.7	n/a	0.18	1.24

*Percent strain $\leq 10\%$

A	DP600 GA	1
B	DP980 GA	1
D	DP980 CR	1
G	TRIP780 GA	1
I	DP780 GA	1.0
R	HSLA50GI	1.0

Table A.2 Chemistry (all units are percent by weight):

Sample	C	Mn	P	S	Si	Al	Nb	Ti	V	Cr	Ni	Mo	B
DP600 GA	0.08	2	0.011	<.003	0.03	0.04	<.003	<.003	<.003	0.01	0.02	<.01	<.0003
DP980 GA	0.1	2.1	0.013	<.003	0.01	0.04	<.003	<.003	<.003	0.26	0.01	0.35	<.0003
DP980 CR	0.13	1.3	0.013	0.006	0.28	0.04	<.003	<.003	<.003	0.01	0.01	<.01	<.0003
TRIP780 GA	0.14	1.5	0.01	<.003	0.06	1.1	0.017	<.003	<.003	0.22	0.01	<.01	<.0003
DP780 GA	0.09	1.8	0.016	<.003	0.01	0.03	<.003	<.003	<.003	0.27	0.02	0.25	<.0003
HSLA50GI	0.08	0.52	0.012	0.008	<.01	0.03	0.016	<.003	<.003	0.02	0.01	<.01	<.0003

APPENDIX B

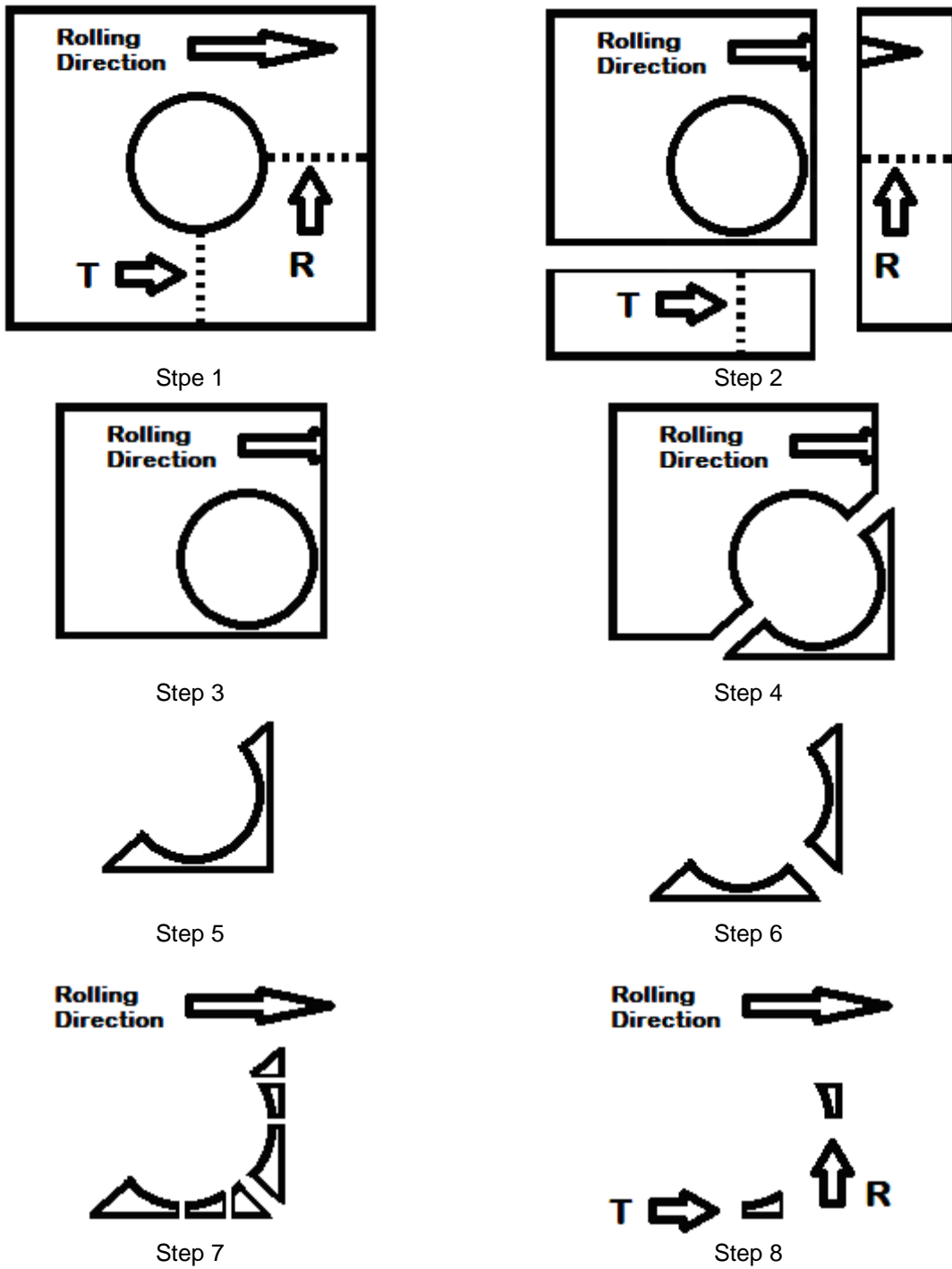


Figure B.1 Sample preparation steps for OD2 observation

APPENDIX C

Table C.1 Rollover zone relative height (h_r / h_0)

C%= 30%						
TD	831	843	873	987	1018	1111
20	0.168577	0.163857	0.220617	0.134523	0.163142	0.167971
40	0.159904	0.191699	0.231298	0.172609	0.165526	0.138534
60	0.166353	0.199704	0.200085	0.142689	0.163831	0.137173
80	0.17525	0.232199	0.193262	0.211918	0.18459	0.138597
RD	819	840	873	975	1055	1092
20	0.163752	0.147553	0.220846	0.163247	0.149018	0.128741
40	0.192016	0.222561	0.262289	0.190984	0.170376	0.152002
60	0.182031	0.20188	0.225578	0.150595	0.170521	0.157323
80	0.180875	0.218474	0.200927	0.153466	0.148501	0.165959
C%= 20%						
TD	831	843	873	987	1018	1111
20	0.087583	0.122041	0.124344	0.146569	0.112419	0.089864
40	0.109991	0.111815	0.14566	0.130875	0.12873	0.111769
60	0.111245	0.135456	0.113617	0.166518	0.137149	0.092082
80	0.105427	0.115845	0.151593	0.108217	0.111219	0.120289
RD	819	840	873	975	1055	1092
20	0.101202	0.11295	0.141615	0.092894	0.111902	0.099217
40	0.112403	0.157376	0.171841	0.11368	0.117819	0.109431
60	0.108433	0.125249	0.153352	0.113165	0.131463	0.146124
80	0.0952	0.145854	0.137735	0.11078	0.117031	0.125425
C%= 10%						
TD	831	843	873	987	1018	1111
20	0.174556	0.059455	0.09751	0.088413	0.070286	0.07376
40	0.110569	0.059326	0.137619	0.088305	0.065827	0.075394
60	0.092708	0.069333	0.100451	0.092577	0.089592	0.085163
80	0.068838	0.070484	0.086659	0.098408	0.073469	0.078609
RD	819	840	873	975	1055	1092
20	0.158806	0.064734	0.10507	0.187828	0.073598	0.068991
40	0.066777	0.090349	0.150542	0.112347	0.085667	0.065641
60	0.108179	0.066247	0.107005	0.098846	0.065731	0.130853
80	0.07798	0.068436	0.11452	0.078883	0.066802	0.073927

Table C.2 Burnish zone relative height (h_b / h_0)

C%= 30%						
TD	831	843	873	987	1018	1111
20	0.261218	0.278652	0.205138	0.14179	0.15054	0.104039
40	0.172574	0.204474	0.141628	0.092657	0.084899	0.09364
60	0.15953	0.160385	0.112145	0.078843	0.108959	0.078032
80	0.165295	0.173273	0.126868	0.085278	0.09461	0.077533
RD	819	840	873	975	1055	1092
20	0.284197	0.257245	0.234674	0.126455	0.128306	0.096307
40	0.212925	0.223841	0.147826	0.091985	0.099915	0.090808
60	0.181433	0.146395	0.121064	0.091057	0.101939	0.081154
80	0.166955	0.176743	0.125156	0.100282	0.083885	0.077134
C%= 20%						
TD	831	843	873	987	1018	1111
20	0.234169	0.193074	0.165262	0.12735	0.149299	0.09976
40	0.148356	0.153418	0.14134	0.065571	0.08777	0.081959
60	0.132551	0.133703	0.120096	0.08445	0.075962	0.074688
80	0.126878	0.115523	0.112642	0.055496	0.078772	0.064258
RD	819	840	873	975	1055	1092
20	0.246721	0.22612	0.159256	0.098312	0.105767	0.100641
40	0.16195	0.154779	0.162397	0.087114	0.106797	0.081946
60	0.139898	0.129582	0.132085	0.081374	0.078819	0.067671
80	0.133824	0.118769	0.105016	0.067705	0.067997	0.065986
C%= 10%						
TD	831	843	873	987	1018	1111
20	0.212207	0.168606	0.173564	0.121646	0.129553	0.103621
40	0.152444	0.147307	0.143129	0.081201	0.094394	0.058314
60	0.127819	0.113558	0.092852	0.070307	0.070213	0.059704
80	0.114909	0.115763	0.113062	0.061259	0.067137	0.060128
RD	819	840	873	975	1055	1092
20	0.256793	0.190605	0.170123	0.096157	0.098341	0.08797
40	0.164761	0.130992	0.157686	0.078054	0.106976	0.067637
60	0.13479	0.112264	0.093887	0.074058	0.072854	0.05604
80	0.129723	0.106135	0.092172	0.056641	0.072459	0.064475

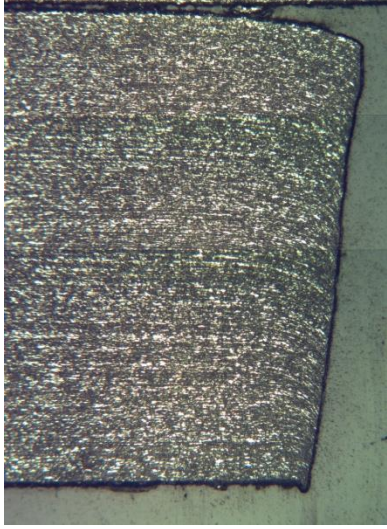
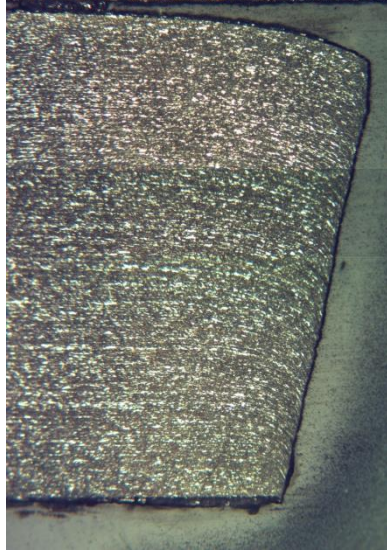
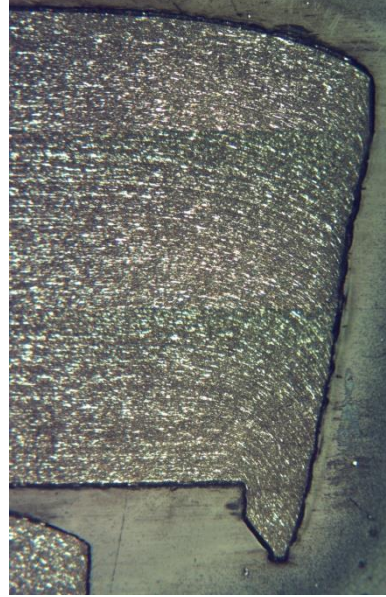
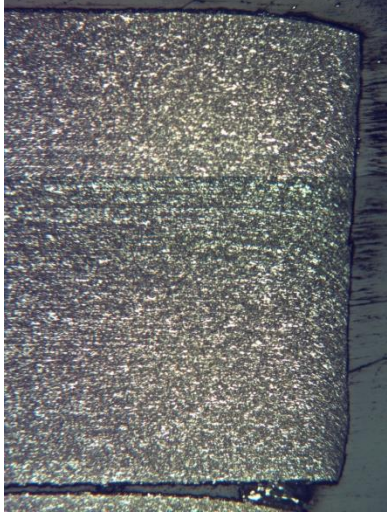
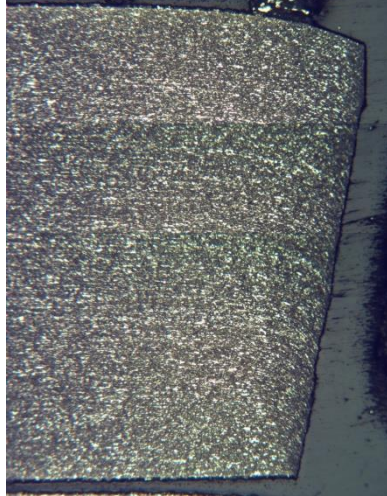
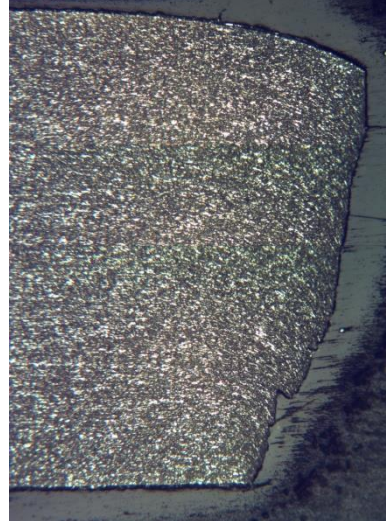
Table C.3 Fracture zone relative height (h_f/h_0)

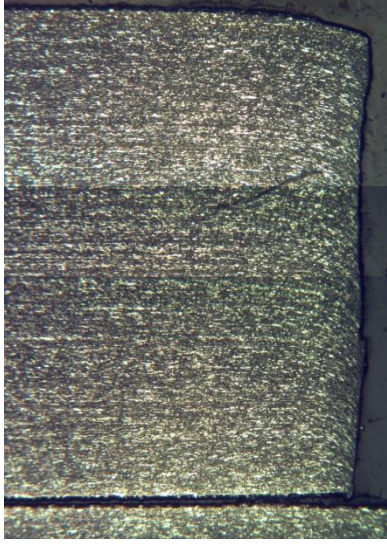
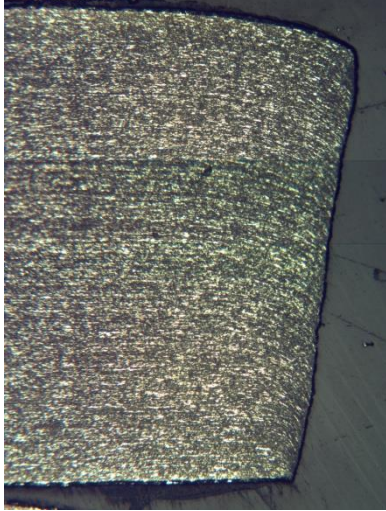
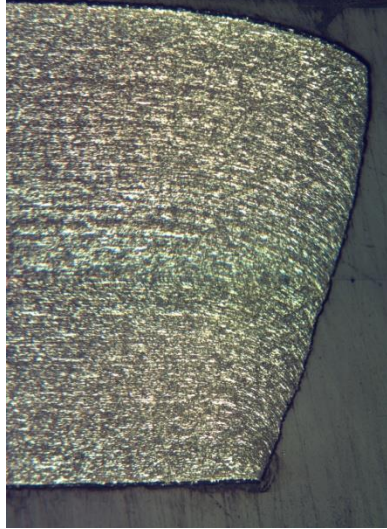
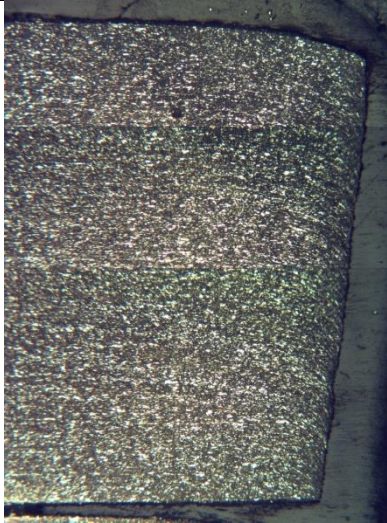
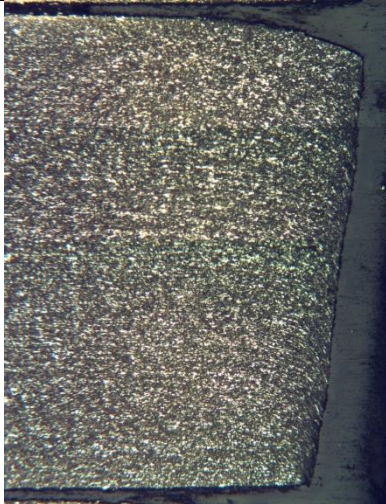
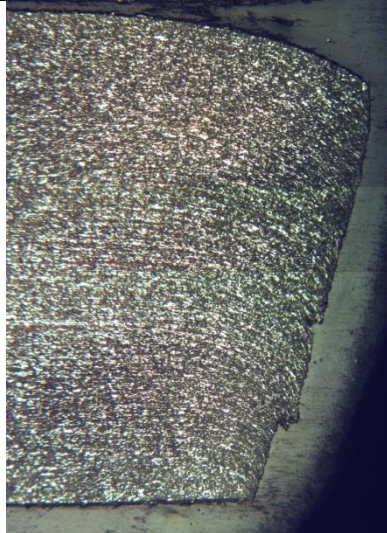
C%= 30%						
TD	831	843	873	987	1018	1111
20	0.570205	0.557491	0.574245	0.723687	0.686318	0.727989
40	0.667522	0.603827	0.627074	0.734734	0.749575	0.767827

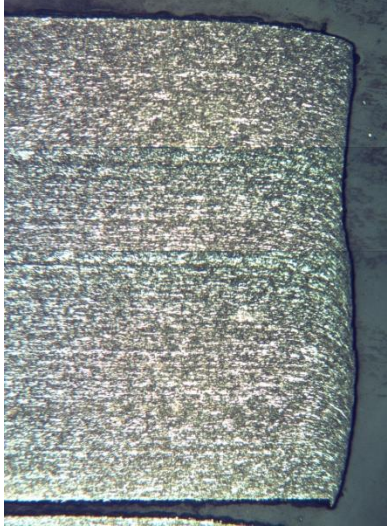
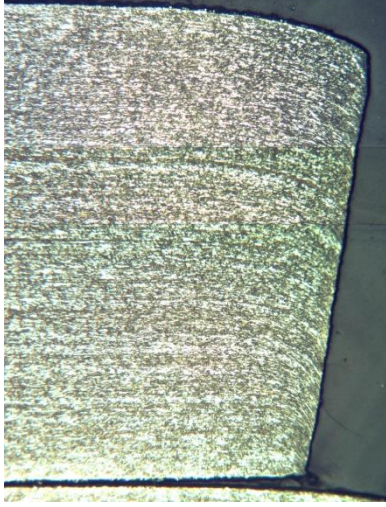
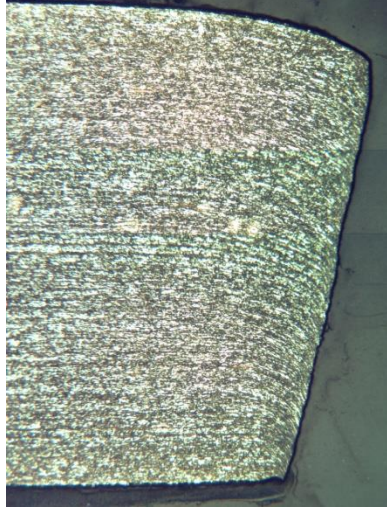
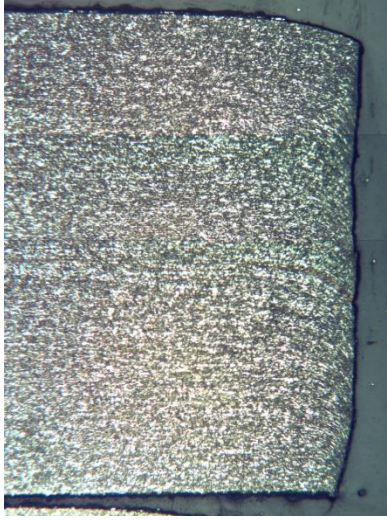
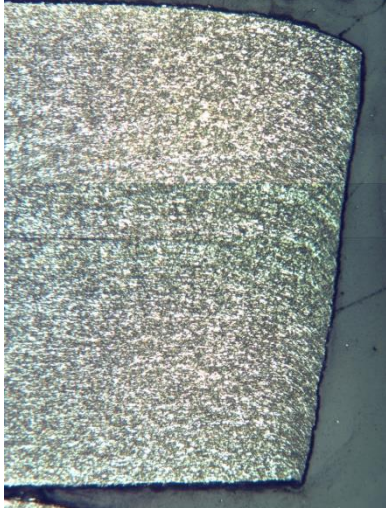
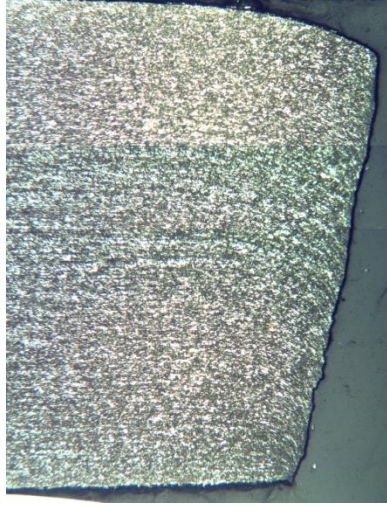
60	0.674116	0.639911	0.68777	0.778468	0.72721	0.784795
80	0.659455	0.594527	0.67987	0.702803	0.7208	0.783869
RD	819	840	873	975	1055	1092
20	0.552051	0.595202	0.54448	0.710298	0.722676	0.774953
40	0.595059	0.553598	0.589885	0.717031	0.729709	0.75719
60	0.636536	0.651725	0.653358	0.758348	0.72754	0.761523
80	0.65217	0.604784	0.673917	0.746253	0.767613	0.756908
C%= 20%						
TD	831	843	873	987	1018	1111
20	0.678248	0.684884	0.710394	0.726081	0.738282	0.810376
40	0.741653	0.734767	0.713	0.803554	0.7835	0.806273
60	0.756204	0.730841	0.766287	0.749033	0.786889	0.83323
80	0.767696	0.768632	0.735765	0.836287	0.810009	0.815453
RD	819	840	873	975	1055	1092
20	0.652078	0.66093	0.699128	0.808793	0.782331	0.800143
40	0.725647	0.687845	0.665762	0.799206	0.775384	0.808623
60	0.751668	0.745168	0.714563	0.805461	0.789718	0.786205
80	0.770976	0.735377	0.757249	0.821515	0.814972	0.808589
C%= 10%						
TD	831	843	873	987	1018	1111
20	0.613237	0.771938	0.728926	0.789941	0.800162	0.822619
40	0.736988	0.793367	0.719252	0.830494	0.839779	0.866292
60	0.779473	0.817109	0.806697	0.837116	0.840195	0.855133
80	0.816254	0.813753	0.80028	0.840333	0.859394	0.861264
RD	819	840	873	975	1055	1092
20	0.584401	0.744661	0.724807	0.716015	0.828061	0.84304
40	0.768463	0.778659	0.691772	0.809599	0.807357	0.866721
60	0.757031	0.821489	0.799108	0.827096	0.861415	0.813107
80	0.792298	0.825429	0.793307	0.864476	0.860739	0.861598

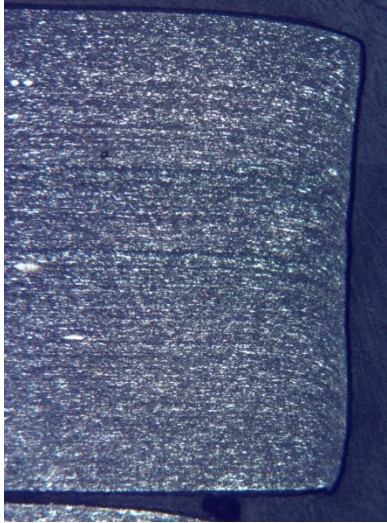
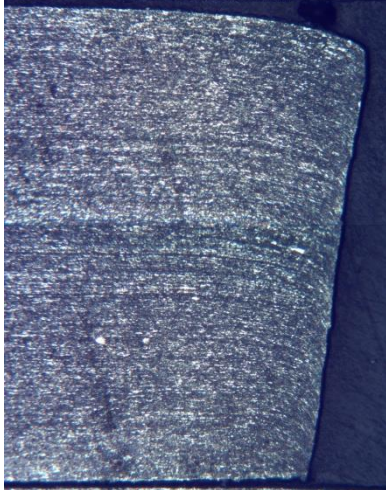
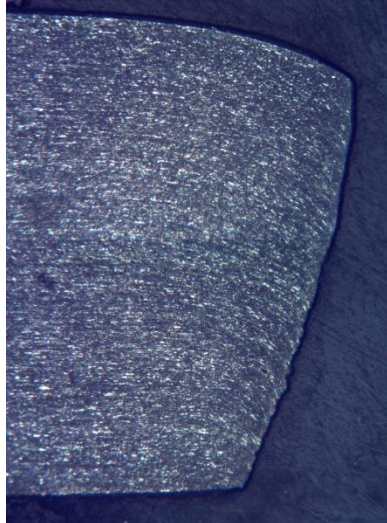
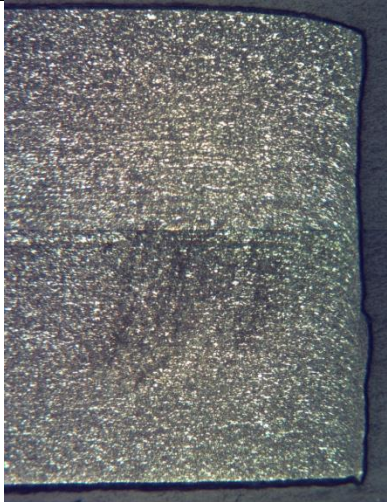
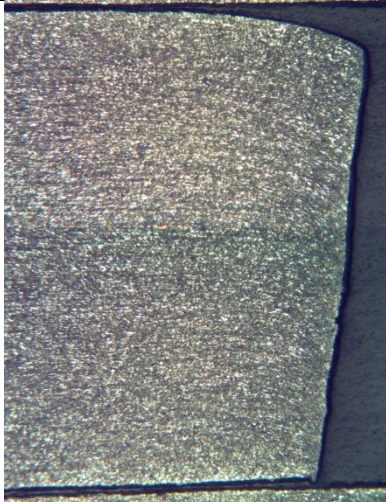
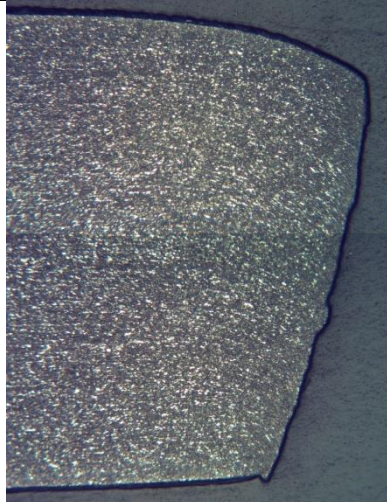
APPENDIX D

Table D.1 DP980 (Code 1) 1.4 Supplier 1 OD2 images

10%	20%	30%
		
1-20 R C1	1-20 R C2	1-20 R C3
		
1-20 T C1	1-20 T C2	1-20 T C3

		
1-40 R C1	1-40 R C2	1-40 R C3
		
1-40 T C1	1-40 T C2	1-40 T C3

		
1-60 R C1	1-60 R C2	1-60 R C3
		
1-60 T C1	1-60 T C2	1-60 T C3

		
1-80 R C1	1-80 R C2	1-80 R C3
		
1-80 T C1	1-80 T C2	1-80 T C3

APPENDIX E

E.1 Shear and ductile failure criteria in ABAQUS [104]

The shear criterion is a phenomenological model for predicting the onset of damage due to shear band localization; the ductile criterion is a phenomenological model for predicting the onset of damage due to nucleation, growth and coalescence of voids. Both of them assume the equivalent plastic strain at the onset of damage, $\bar{\epsilon}_S^{pl}$ or $\bar{\epsilon}_D^{pl}$, are functions of shear stress ratio (θ_s) or stress triaxiality (η) and strain rate ($\dot{\epsilon}^{pl}$).

Table E.1 Shear and Ductile damage initiation criteria

Shear criterion	Ductile criterion
$\bar{\epsilon}_S^{pl}(\theta_s, \dot{\epsilon}^{pl})$	$\bar{\epsilon}_D^{pl}(\eta, \dot{\epsilon}^{pl})$
$\theta_s = (q + k_s p) / \tau_{max}$, $\eta = p/q$, $\dot{\epsilon}^{pl}$ is the equivalent plastic strain rate, p is the pressure stress, q is the Mises equivalent stress, τ_{max} is the maximum shear stress, and k_s is a material parameter, default value is 0.	
$\omega_S = \int \frac{d\bar{\epsilon}^{pl}}{\bar{\epsilon}_S^{pl}(\theta_s, \dot{\epsilon}^{pl})} = 1$	$\omega_D = \int \frac{d\bar{\epsilon}^{pl}}{\bar{\epsilon}_D^{pl}(\eta, \dot{\epsilon}^{pl})} = 1$
ω_S and ω_D : are state variables that increase monotonically with plastic deformation proportional to the incremental change in equivalent plastic strain.	
$\Delta\omega_S = \frac{\Delta\bar{\epsilon}^{pl}}{\bar{\epsilon}_S^{pl}(\theta_s, \dot{\epsilon}^{pl})} \geq 0$	$\Delta\omega_D = \frac{\Delta\bar{\epsilon}^{pl}}{\bar{\epsilon}_D^{pl}(\eta, \dot{\epsilon}^{pl})} \geq 0$
$\bar{\epsilon}_0^{pl}$: is any initial value of the equivalent plastic strain $\Delta\bar{\epsilon}^{pl}$: is an increment of the equivalent plastic strain $\bar{\epsilon}_f^{pl}$: is the strain at failure, assumed to depend on the plastic strain rate $\dot{\epsilon}_f^{pl}$	

In this chapter, the shear failure model, which is based on the value of the equivalent plastic strain at element integration points, is used. Failure is assumed to occur when the damage parameter, ω , exceeds

1. The damage parameter:

$$\omega = \frac{\bar{\epsilon}_0^{pl} + \sum \Delta\bar{\epsilon}^{pl}}{\bar{\epsilon}_f^{pl}} \quad (E.1)$$

Because the effect of pressure-deviatoric stress ratio is ignored in the simulation, so in simulation use either shear or ductile criteria, lead to no difference in results.

E.2 Damage evolution laws in ABAQUS [105]

The damage evolution law describe the rate of degradation of the material stiffness after reaching the corresponding initiation criterion.

$$\sigma = (1 - D)\bar{\sigma} \quad (\text{E.2})$$

Where D is the overall damage variable and $\bar{\sigma}$ is the effective (or undamaged) stress tensor computed in the current increment. $\bar{\sigma}$ are the stress that would exist in the material in the absence of damage. The material has lost its loading-carrying capacity when D=1.

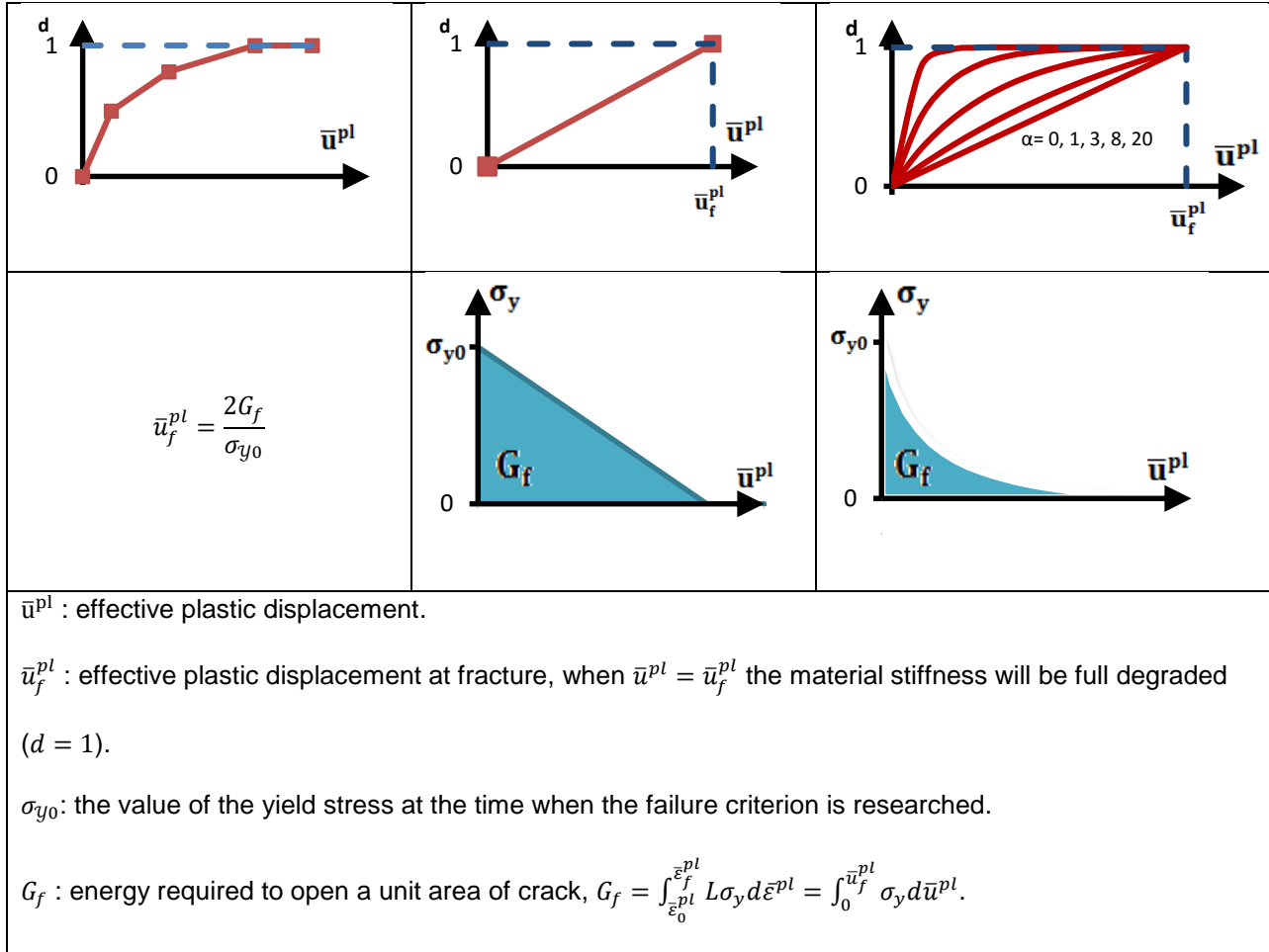
The overall damage variable, D, captures the combined effect of all active mechanisms and is computed in terms of the individual damage variables, d_i , according to a user-specified rule.

Before damage initiating, the effective plastic displacement rate ($\dot{\bar{u}}^{pl}$) equal to 0, after reaching the damage initiation criterion, the effective displacement (\bar{u}^{pl}) is defined with the evolution equation $\dot{\bar{u}}^{pl} = L\dot{\bar{\epsilon}}^{pl}$, L is the characteristic length of the element, which used to reduce mesh dependency. With brittle fracture approach, the softening response after damage initiation is characterized by a stress-displacement response rather than a stress-strain response.

The evolution of the damage variable with the relative plastic displacement can be specified in tabular, linear and exponential form.

Table E.2 Damage evolution laws

Tabular form	Linear form	Exponential form
For displacement $d = d(\bar{u}^{pl})$	For displacement $\dot{d} = \frac{L\dot{\bar{\epsilon}}^{pl}}{\bar{u}_f^{pl}} = \frac{\dot{\bar{u}}^{pl}}{\bar{u}_f^{pl}} ; d = \frac{\bar{u}^{pl}}{\bar{u}_f^{pl}}$ Based on energy dissipated during the damage process $d = \frac{\bar{u}^{pl}\sigma_{y0}}{2G_f}$	For displacement $d = \frac{1 - e^{-\alpha(\bar{u}^{pl}/\bar{u}_f^{pl})}}{1 - e^{-\alpha}}$ Based on energy dissipated during the damage process $d = 1 - \exp\left(-\int_0^{\bar{u}^{pl}} \frac{\bar{\sigma}_y \dot{\bar{u}}_f^{pl}}{G_f}\right)$



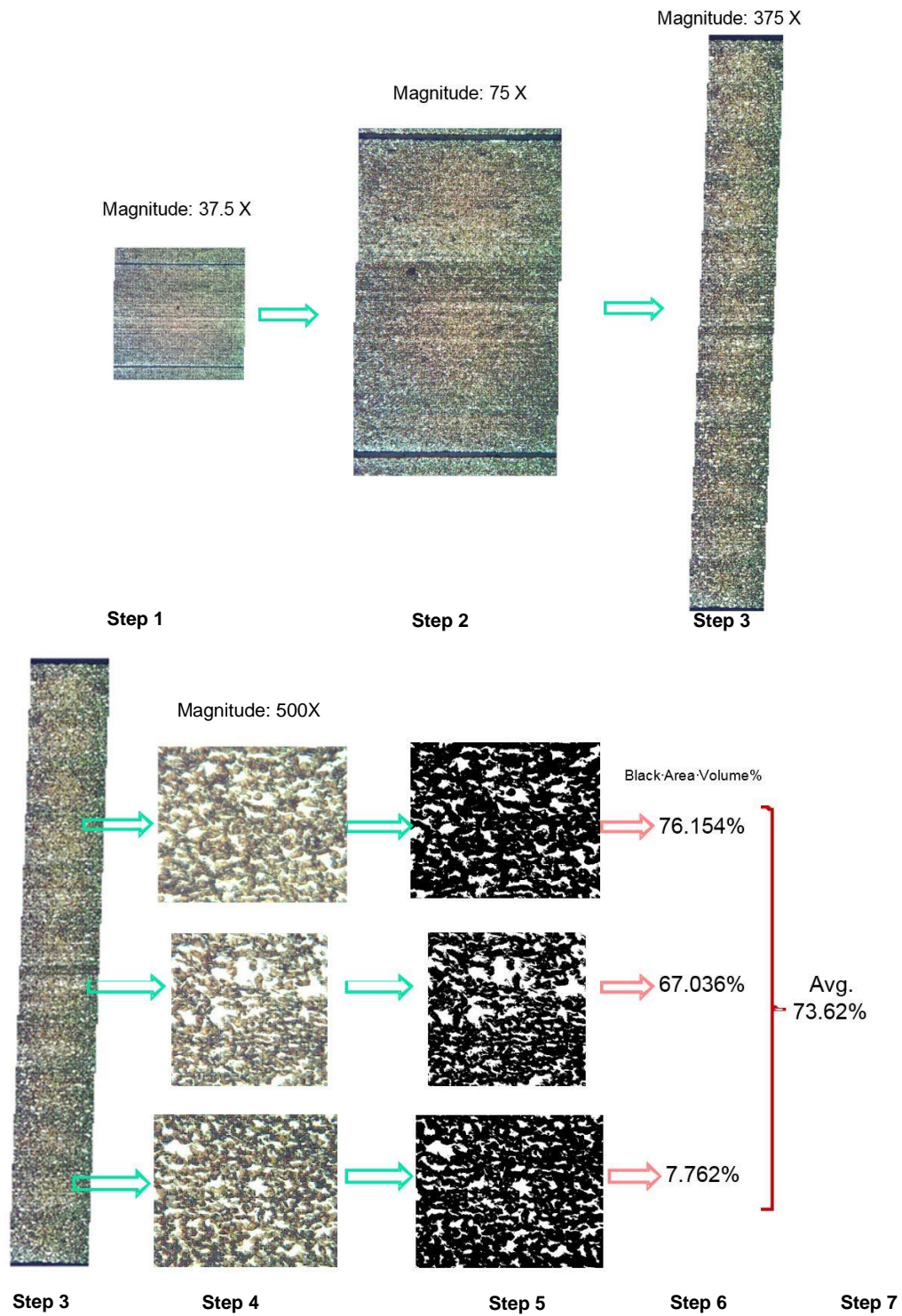
APPENDIX F

Table F.1 Hole expansion test result

Initial Hole Diameters	Type	DP780 1.4			DP980 1.4		
	C% Supplier	10%	20%	30%	10%	20%	30%
20	S1	16%	23%	13%	6.9%	7.8%	5.6%
20	S2	11%	16%	8%	14.0%	6.6%	5.1%
40	S1	14%	20%	17%	9%	11%	9%
40	S2	24%	26%	22%	15%	22%	19%
60	S1	17%	22%	21%	6%	10%	10%
60	S2	21%	31%	23%	14%	25%	25%
80	S1	17%	23%	23%	7%	8%	9%
80	S2	25%	31%	23%	15%	22%	25%

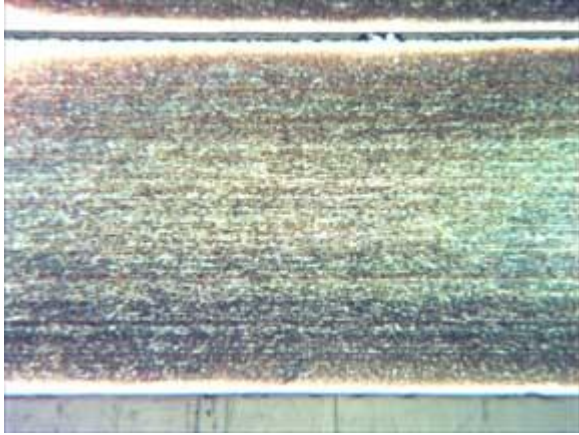
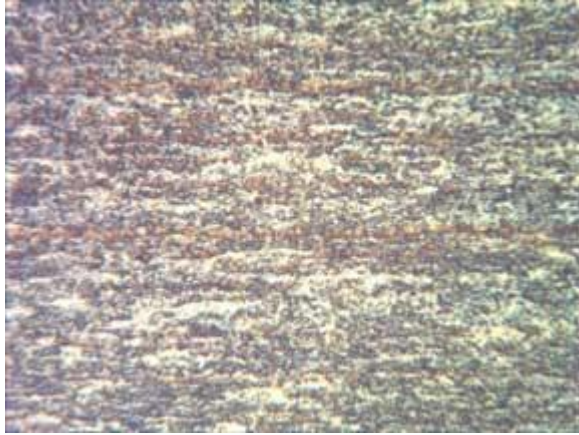
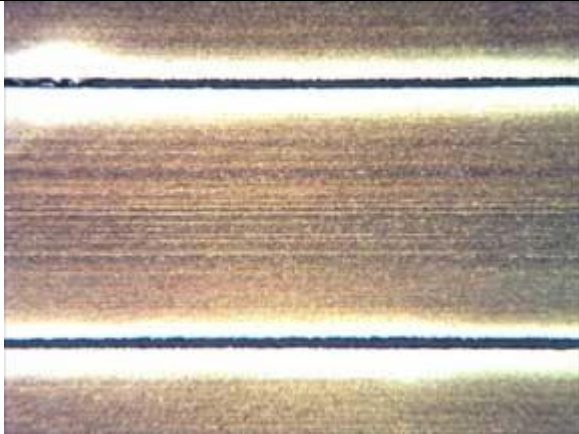
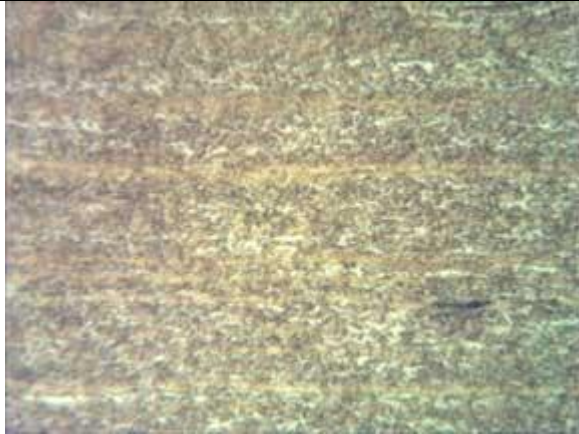
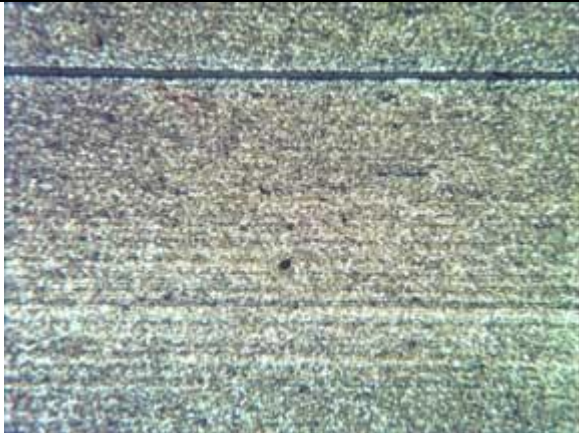

APPENDIX G

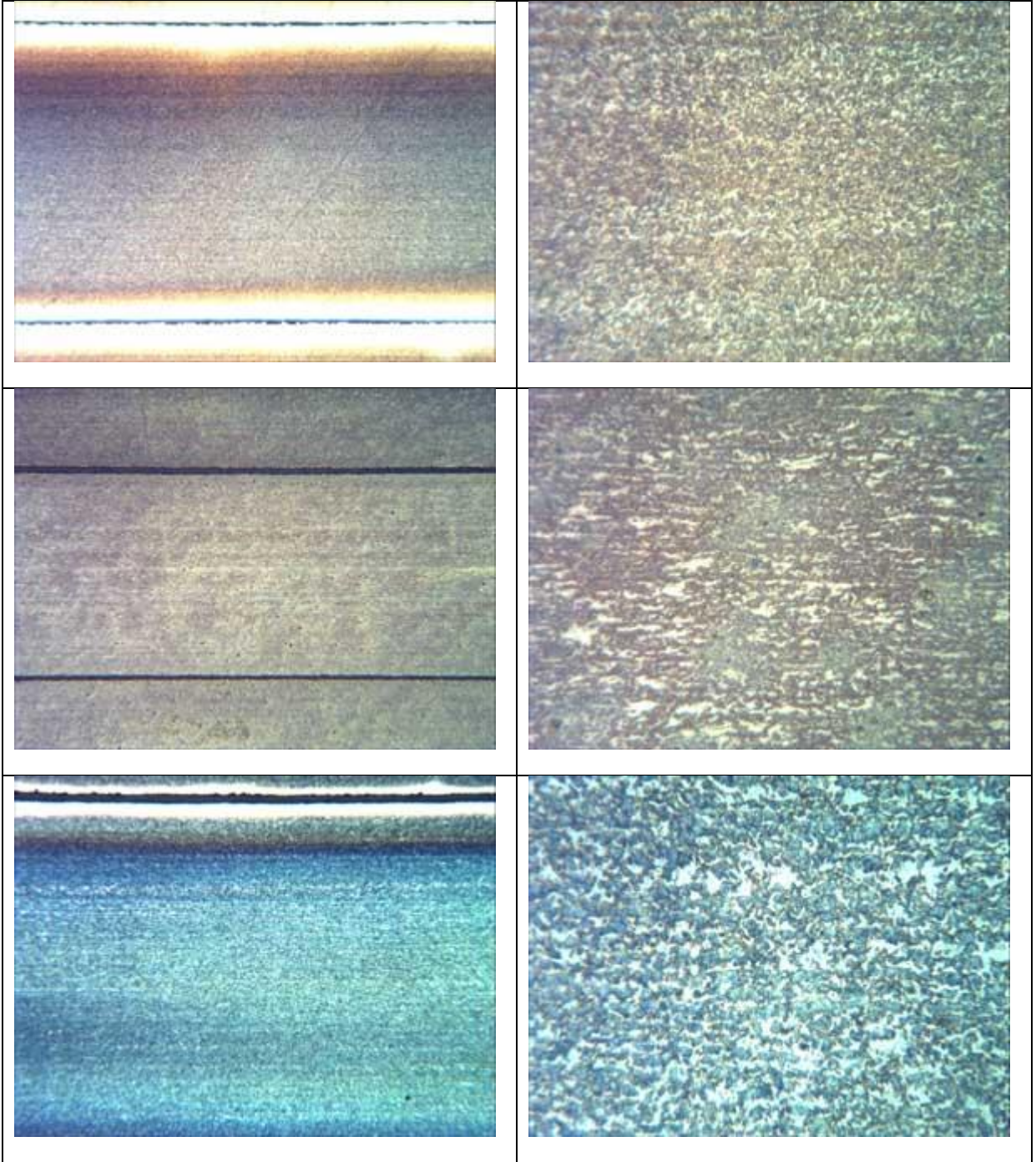
Steps to calculate the averaged martensite volume fraction

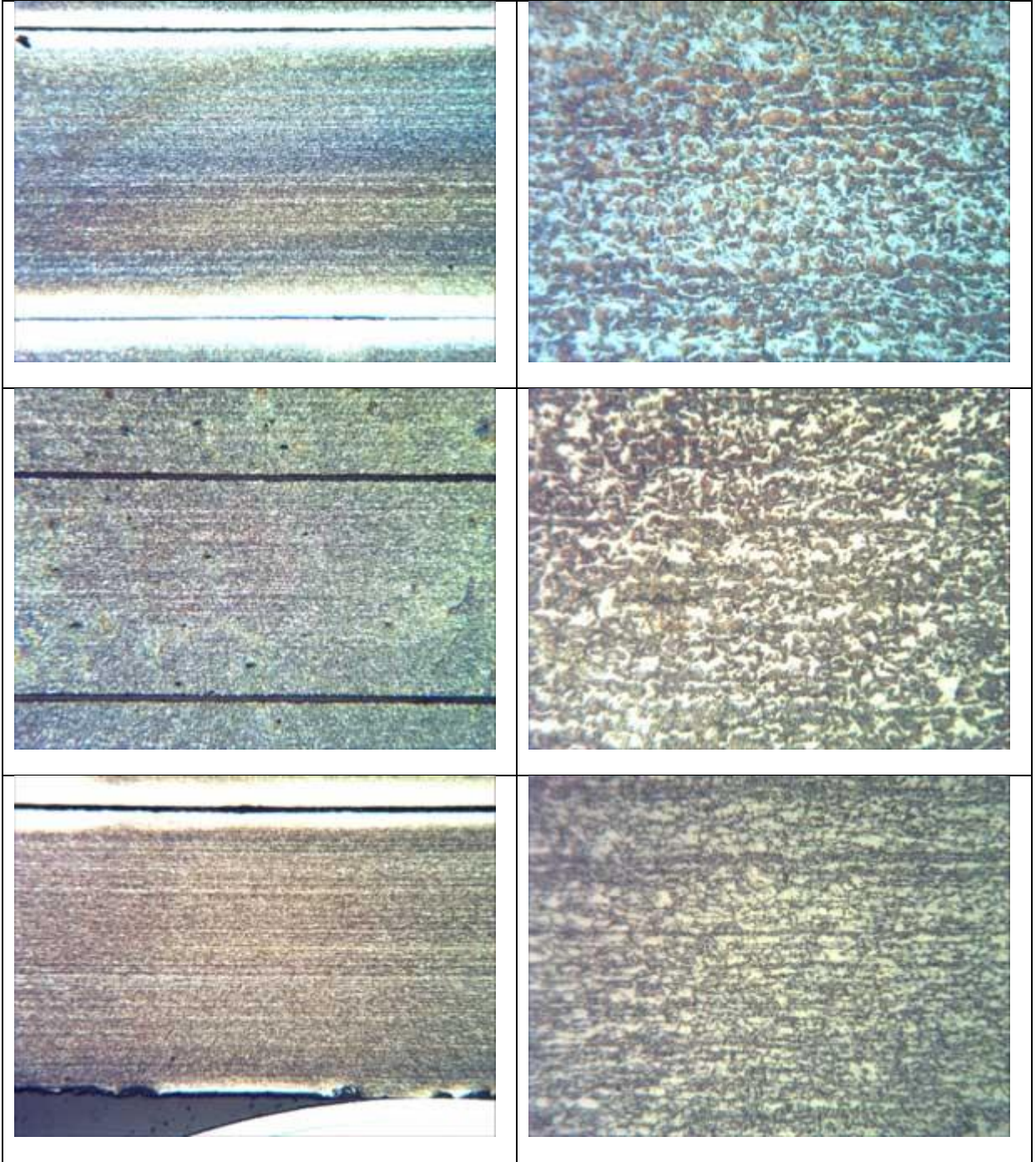


APPENDIX H

Table H.1 Microstructures of dual phase (DP) steels from different suppliers

Macro-scope images	Magnitude X500
	
	
	





REFERENCES

- [1] ADVANCED HIGH STRENGTH STEEL (AHSS) APPLICATION GUIDELINES Version 3, INTERNATIONAL IRON & STEEL INSTITUTE, September 2006
- [2] ADVANCED HIGH STRENGTH STEEL APPLICATION GUIDELINES, Version 4.1, WorldAutoSteel, June 2009
- [3] Advanced High-Strength Steels Application Guidelines, Version 5.0, WorldAutoSteel, May 2014
- [4] Stuart Keeler and Pete Ulintz, Advanced High Strength Steels Solve Growing Demands for Formability, May, 01,2011
- [5] ASTM Designation: E646-07, Standard Test Method for Tensile Strain-Hardening Exponents (n-value) of Metallic Sheet Materials
- [6] ASTM Designation: E517 Standard Test Method for Plastic Strain Ratio (r) for Sheet Metal
- [7] http://www.substech.com/dokuwiki/doku.php?id=dmitri_kopeliovich
- [8] R.A. Kot and B.L. Bramfitt, Fundamentals of Dual-Phase Steels, 1981
- [9] T.L. Anderson, Fracture mechanics Fundamentals and applications, Third Edition
- [10] William D. Callister, Jr. Fundamentals of Materials Science and Engineering, Second Edition, John Wiley & Sons, Inc., 2005
- [11] Jean Lemaitre and Rodrigue Desmorat, Engineering Damage Mechanics, Springer, 2005
- [12] H.P. Rossmannith, Fracture Research in Retrospect, Page125-126, 1997
- [13] Jean Lemaitre, A Course on Damage Mechanics, Springer-Verlag, 1992
- [14] Abaqus Analysis User's Manual (6.12), 24.1.1 Progressive damage and failure
- [15] Kenneth Schmid, Xin Wu, Flange Shear Affected Zone Study, Great Designs in Steel, May,2010
- [16] Mike Shih, Constantin Chiriac, Ming F. Shi, The effects of AHSS shear edge condition on edge fracture, Great Design in Steel, May, 2012
- [17] Jody N. Hall, Jason Coryell, Bill Wendt, Donald Adamski, Case Studies of Edge Fracture of Dual Phase Steel Stampings, *SAE Int. J. Mater. Manf.* 8(3):783-788, 2015, doi:10.4271/2015-01-0529
- [18] Dietmar Gross, Thomas Seeling, Fracture Mechanics with an introduction to micromechanics, Springer, 2006

- [19] Min Jie, GENERALIZED CRITERIA FOR LOCALIZED NECKING IN SHEET METAL FORMING, University of Michigan, Ph.D. Dissertation, 2003
- [20] Jean Lemaitre, A Course on Damage Mechanics, Springer-Verlag, 1992
- [21] J. Skrzypek and A. Ganczarski, Modeling of material Damage and Failure of Structures: Theory and Applications, Springer, 1999
- [22] C.W. Woo, D.L. Li, A universal physically consistent definition of material damage, International Journal of Solids and Structures, Volume 30, Issue 15, 1993, Page 2097-2108
- [23] LAZAE M. KACHANOV, Rupture time under creep conditions, Leningrad University, (translated from Izvestia Akademii Nauk SSSR, Otdelenie tekhnicheskikh nauk, no. 8. 1958 pp. 26-31, in Russian) International Journal of Fracture 97: xi–xviii, 1999
- [24] A.L. Gurson. Continuum theory of ductile rupture by void nucleation and growth: Part I. Yield criteria and flow rules for porous ductile media. Journal of Engineering Materials and Technology- Trans. of the ASME, 99;2-15.1977
- [25] VIGGO TVERGAARD, Influence of voids on shear band instabilities under plane strain conditions, Department of Solid Mechanics, The Technical University of Denmark, Lyngby, Denmark, December 4, 1979
- [26] R. Hill, Proceedings of the Royal Society of London. Series A, Mathematical and Physical Sciences Vol. 193, No. 1033 (May 27, 1948), pp. 281-297
- [27] D. Banabic, Sheet Metal Forming Processes, Springer-Verlag Berlin Heidelberg, 2010
- [28] R. Hill, Theoretical plasticity of textured aggregates, Mathematical Proceedings of the Cambridge Philosophical Society, 85, pp 179-191 doi:10.1017/S0305004100055596
- [29] R. Hill, A user-friendly theory of orthotropic plasticity in sheet metals, International Journal of Mechanical Science, Volume 35, Issue 1, January 1993, Pages 19-25
- [30] GORDON R. JOHNSON and WILLIAM H. Cook, Fracture Characteristics of Three Metals Subjected to Various Strains, Strain rates, Temperatures and Pressures, Engineering Fracture Mechanics, vol. 21, no.1, pp. 31–48, 1985
- [31] Liang Xue, Ductile Fracture Modeling- Theory, Experimental Investigation and Numerical Verification, Massachusetts Institute of Technology, Ph.D. Dissertation, 2007

- [32] <http://abaqusdoc.ucalgary.ca/v6.9/books/usb/default.htm?startat=pt05ch20s02abm41.html#usb-mat-cdamageinitductile>
- [33] M.L. Wilkins, R.D. Streit, J. E. Reaugh, Cumulative-Strain-Damage Model of Ductile Fracture: Simulation and Prediction of Engineering Fracture Tests, , October, 03, 1980
- [34] Viggo Tvergaard, Alan Needleman, Analysis of the cup-cone fracture in a round tensile bar, Acta Metallurgica, Volume 32, Issue 1, pp. 157-169, Jan 1984
- [35] <http://www.custompartnet.com/wu/sheet-metal-shearing>
- [36] T. M. CHANG, H. W. SWIFT, SHEARING OF METAL BARS, Journal of the Institute of Metals, Vol. 78, pp119-146, 1950
- [37] Sergey F. Golovashchenko, Andrey M. Ilinch, Analysis of Trimming Processes for Advanced High Strength, SAE International, 2008-01-1446
- [38] Mai Huang, Liwei Zhang, Standardization and Automation of Hole Expansion Test, Great Designs in Steel 2011 PowerPoint Presentations, 5/18/2011
- [39] Mai Huang, Jugraj Singh, A/SP Standardization of the Hole Expansion Text, Great Designs in Steel 2011 PowerPoint Presentations, 5/14/2014
- [40] Michael Shih, An Innovative Shearing Process For AHSS Edge Stretchability Improvements, Great Designs in Steel 2012 PowerPoint Presentations, 5/16/2012
- [41] Michael Shih, Gene Hsiung, Optimal Production Trimming Process for AHSS Sheared Edge Stretchability Improvements, Great Designs in Steel 2012 PowerPoint Presentations, 5/14/2014
- [42] A. G. ATKINS, On cropping and related processes, International Journal of Mechanical Sciences, Vol. 22, pp 215-231, 1980
- [43] QING ZHOU, TOMASZ WIERZBIKI, A TENSION ZONE MODEL OF BLANKING AND TEARING OF DUCTILE METAL PLATES, International Journal of Mechanical Sciences, Vol. 38. No. 3. pp. 303-324, 1996
- [44] Y.W. Stegeman, A.M. Goijaerts, D. Brokken, W.A.M. Brekelmans, L.E. Govaert, F.P.T. Baaijens, An experimental and numerical study of a planar blanking process, Journal of Materials Processing Technology, 87 (1999) 266–276

- [45] X.H. Hu, K. S. Choi, X. Sun, S. F. Golovashchenko, Edge Fracture Prediction of Traditional and Advanced Trimming Processes for AA6111-T4 Sheets, Journal of Manufacturing Science and Engineering, APRIL 2014, Vol. 136 / 021016-1
- [46] Xin Wu, Hamed Bahmanpour, Ken Schmid, Characterization of mechanically sheared edges of dual phase steels, Journal of Materials Processing Technology, 212 (2012) 1209– 1224
- [47] Abaqus Analysis User's Manual, Volume III: Material
- [48] K.H. Shim, S.K. Lee, B.S. Kang, S.M. Hwang, investigation on blanking of thin sheet metal using the ductile fracture criterion and its experimental verification, Journal of Materials Processing Technology 155-156 (2004) 1935-1942
- [49] Magnus Söderberg, Finite Element Simulation of Punching, Luleå University of Technology, 2006:068 CIV, ISSN: 1402-1617
- [50] C. Husson, J.P.M Correia, L. Daridon, S. Ahzi, Finite elements simulations of thin copper sheets blanking: Study of blanking parameters on sheared edge quality, Journal of material processing technology, Volume 199, Issues 1-3, 1 April 2008, Pages 74-83
- [51] A. Dalloz, J. Besson, A.-F. Gourgues-Lorenzon, T. Sturel, A. Pineau, Effect of shear cutting on ductility of a dual phase steel, Engineering Fracture Mechanics, 76 (2009) 1411-1424
- [52] Haykel Marouani, Mohamed Rachik, Eric Hug, Experimental investigations and FEM simulations of parameters influencing the Fe-(wt.3%)Si shearing process, Mechanics & Industry 13, 271-278 (2012)
- [53] X.H. Hu, K. S. Choi, X. Sun, S. F. Golovashchenko, Edge Fracture Prediction of Traditional and Advanced Trimming Processes for AA6111-T4 Sheets, Journal of Manufacturing Science and Engineering, APRIL 2014, Vol. 136 / 021016-1
- [54] Stuart Keeler, Are laboratory forming tests worthwhile? The Science of Forming, December 01, 2011 Issue
- [55] Shih H-C and Shi M.F., 2011, "An Innovation Shearing Process for AHSS Edge Stretchability Improvement," Journal of Manufacturing Science and Engineering, vol. 133 / 061018-1.
- [56] Hua-Chu Shih, Ching-Kuo Hsiung, Bill Wendt, Optimal Production Trimming Process for AHSS sheared Edge Stretchability Improvement, SAE Technical Paper 2014-01-0994, doi:10.4271/2014-01-0994.

- [57] A. Konieczny, T. Henderson, On Formability Limitations in Stamping Involving Sheared Edge Stretching, SAE Technical Paper 2007-01-0340, doi:10.4271/2007-01-0340
- [58] Xu Chen, Lianxiang Yang, Xiaoming Chen, Constantin Chiriac, Changqing Du, Dajun Zhou, Measure of Strain Distribution for Hole Expansion with Digital Image Correlation (DIC), SAE International, 2011-01-0993, 04/12/2011
- [59] Constantin Chiriac, A study of the Plastic Deformation of Sheared Edges of Dual Phase 780 Steels, SAE Technical Paper 2010-01-0441, 2010, doi:10.4271/2010-01-0441
- [60] Constantin Chiriac, Ming F. Shi, Todd M. Link, The Prestrain Effect on the Sheared Edge Flangeability of Dual Phase 780 Steels, SAE Technical Paper 2012-01-0533, 2012, doi:10.4271/2012-01-0533
- [61] Constantin Chiriac, Ming F. Shi, Study on Edge Strain Hardening Produced by Trimming Operations, SAE Technical Paper 2013-01-1774, 2013, doi:10.4271/2013-01-1774.
- [62] Constantin Chiriac, Ming F. Shi, Experimental Study of Edge Stretching Limits of DP980IBF Steel in Multistage forming Process, *SAE Int. J. Mater. Manf.* 8(2):415-418, 2015, doi:10.4271/2015-01-0525.
- [63] Andrey Ilinich, Lorenzo Smith, Sergey Golovashchenko, SAE Technical Paper 2011-01-1062, 2011, doi:10.4271/2011-01-1062.
- [64] Examining edge cracking in hole flanging of AHSS, STAMPING JOURNAL, JULY/AUGUST 2008.
- [65] SEBASTIAN SCHEIB, PARCHAPOL SATKULVANICH, TAYLAN ALTAN, Examining edge cracking in hole flanging of AHSS Part II: Modeling of blanking, STAMPING JOURNAL, SEPTEMBER 2008.
- [66] PARCHAPOL SATKULVANICH, TAYLAN ALTAN, Examining edge cracking in hole flanging of AHSS Part III: The effects of punch speed, materials, and tool wear, STAMPING JOURNAL, OCTOBER 2008.
- [67] PARCHAPOL SATKULVANICH, TAYLAN ALTAN, Examining edge cracking in hole flanging of AHSS Part IV: Sheared edge stretching, STAMPING JOURNAL, NOVEMBER 2008.
- [68] P. Sartkulvanich, B. Kroenauer, R. Golle, A. Konieczny, T. Altan, Finite element analysis of the effect of blanked edge quality upon stretch flanging of AHSS, *Manufacturing Technology*, Volume 59, Issue 1, 2010, Page 279-282

- [69] Ko Y.K., Lee J.S., Huh H., Kim H.K., Park S.H., Prediction of fracture in hub-hole expanding process using a new ductile fracture criterion. *J. Mater. Process. Technol.*, 358–362, 2007.
- [70] Butcher C., Anderson D., Worswick M., Predicting Failure during Sheared Edge Stretching Using a Damage-Based Model for the Shear-Affected Zone, *SAE Int. J. Mater. Manf.* 6(2):2013.
- [71] V. Uthaisangasuk, U. Prah, W. Bleck, Stretch-flangeability of multiphase steel using a microstructure based failure modelling, *Computational Materials Science*, Volume 45, Issue 3, Pages 617-623, May 2009
- [72] Ming F. Shi and Xiaoming Chen, Prediction of Stretch Flangeability Limits of Advanced High Strength Steels using the Hole Expansion Test, *SAE Technical Paper 2007-01-1693*, 2007, doi:10.4271/2007-01-1693.
- [73] Dajun Zhou, Changqing Du, John Siekirk III, Ken Schmid, Ming Chen, AHSS Edge Cracking Criteria Development from Large Stampings with a Big Cutout, *Great Designs in Steel 2011 PowerPoint Presentations*, 5/18/2011
- [74] Dajun Zhou, Changqing Du, John Siekirk, John McGuire, Xiaoming Chen, Bernard S. Levy, A Practical Failure Limit for Sheared Edge Stretching of Automotive Body Panels, *SAE Technical Paper 2010-01-0986*, doi:10.4271/2010-01-0986.
- [75] Yanshan Lou, Hoon Huh, Gihyun Bae, Younki Ko, Seokbong Kim, Application of Ductile Fracture Criteria to Fracture Prediction of Punch-Stretch Tests, *KSAE11-B0375*, 2011.
- [76] Nan Wang, Sergey Golovashchenko, Quochung Le, Experimental Study of Stretchability of Sheared Edge of Aluminum Sheet 6111-T4, 2015-01-0516, 2015-04-14
- [77] R.D. Adamczyk and G.M. Michal, Sheared Edge Extension of High-Strength Cold-Rolled steels, *J. Appl. Metalwork*, 1986, 4(2), p 157-163
- [78] R.J. Comstock, Jr., D.K. Scherrer, and R.D. Adamczyk, Hole Expansion in a Variety of Sheet Steels, *Journal of Materials Engineering and Performance*, January 20, 2006
- [79] Hyun, D.I., Oak, S.M., Kang, S.S., Moon, Y.H., 2002. Estimation of hole flangeability for high strength steel plates. *J. Mater. Process. Technol.*, 9–13
- [80] X. Fang, Z. Fan, B. Ralph, P. Evans, and R. Underhill, The relationships between tensile properties and hole expansion property of C–Mn steels. *Journal of Material Science* 38, 3877–3882, 2003.

- [81] Kohei HASEGAWA, Kenji KAWAMURA, Toshiaki URABE and Yoshihiro HOSOYA1, Effects of Microstructure on Stretch-flange-formability of 980 MPa Grade Cold-rolled Ultra High Strength Steel Sheets, *ISIJ International*, Vol. 44, No. 3, pp. 603–609, 2004.
- [82] S. B. Lee, J. G. Speer, D. K. Matlock, and K. G. Chin, “Analysis of Stretch-Flangeability using a Ductile Fracture Model,” *Proceedings of the 3rd International Conference on Advanced Structural Steels*, 2006, pp. 841–849.
- [83] B.S. Levy and C.J. Van Tyne, Failure During Sheared Edge Stretching , *Journal of Materials Engineering and Performance*, 17: 842-848, 2008
- [84] B.S. LEVY, M. GIBBS, and C.J. Van TYNE, Failure during Sheared Edge Stretching of Dual-Phase Steels, *Metallurgical and Materials Transactions A*, Volume 44, Issue 8, pp 3635-3648, August 2013.
- [85] Kwansoo Chung, Ning Ma, Taejoon Park, Dongun Kim, Donghoon Yoo, Chongmin Kim, A modified damage model for advanced high strength steel sheets, *International Journal of Plasticity* 27(2011) 1485-1511, 2011.
- [86] E. Maire, O. Bouaziz, M. Di Michiel, C. Verdu, Initiation and growth of damage in a dual-phase steel observed by X-ray microtomography, *Acta Materialia*, Volume 56, Issue 18, October 2008, Page 4957-4964
- [87] C. Landron, E. Maire, O. Bouaziz, J. Adrien, L. Lecarme, A. Bareggi, Validation of void growth models using X-ray microtomography characterization of damage in dual phase steels, *Acta Materialia*, Volume 59, Issue 20, December 2011, Page 7564-7573
- [88] C. Landron, E. Maire, J. Adrien, O. Bouaziz, M. Di Michiel, P. Cloetens, H. Suhonen, Resolution effect on the study of ductile damage using synchrotron X-ray tomography, *Nuclear Instruments and Methods in Physics Research Section B: Beam Interactions with Materials and Atoms*, Volume 284, 1 August 2012, Page 15-18
- [89] F.M. Al-Abbasi, J.A. Nemes, Micromechanical modeling of dual phase steels, *International Journal of Mechanical Sciences*, Volume 45, Issue 9, September 2003, Pages 1449–1465, doi:10.1016/j.ijmecsci.2003.10.007

- [90] F.M. Al-Abbasi, J.A. Nemes, Characterizing DP-steels using micromechanical modeling of cells, *Computational Materials Science*, Volume 39, Issue 2, April 2007, Pages 402–415, doi:10.1016/j.commatsci.2006.07.003
- [91] X. Sun, K.S. Choi, A. Soulami, W.N. Liu, M.A. Khaleel, On key factors influencing ductile fractures of dual phase (DP) steels, *Materials Science and Engineering: A*, Volume 526, Issues 1–2, 25 November 2009, Pages 140–149, doi:10.1016/j.msea.2009.08.010
- [92] X. Sun, K.S. Choi, W.N. Liu, M.A. Khaleel, Predicting failure modes and ductility of dual phase steels using plastic strain localization, *International Journal of Plasticity* 25 (2009) 1888-1909
- [93] A. Ramazani, A. Schwedt, A. Aretz, U. Prah, W. Bleck, *Computational Materials Science* 75 (2013) 35–44
- [94] Surajit Kumar Paul, Micromechanics based modeling of Dual Phase steels: Prediction of ductility and failure modes, *Computational Materials Science*, Volume 56, April 2012, Pages 34–42
- [95] Leczek Wojnar, Krzysztof J. Kurzydłowski, Chapter 7 of *Practical Guide to Image Analysis*. Materials Park, OH, USA: ASM International, Page 158, 2000.
- [96] Leczek Wojnar, Krzysztof J. Kurzydłowski, Chapter 7 of *Practical Guide to Image Analysis*. Materials Park, OH, USA: ASM International, Page 158, 2000.
- [97] A. Nishimoto, Y. Hosoya, K. Nakaoka, RELATION BETWEEN THE EXPANSION FORMABILITY AND METALLURGICAL FACTORS IN DUCAL-PHASE STEEL SHEET, *Fundamentals of Dual-Phase Steels*, page 447-463, 1981
- [98] Y. Bergström, *Material Science Engineering*, 5 (1969/1970), pp. 193–200
- [99] R. Rodriguez, I. Gutierrez, in: *Proceeding of TMP'04, Liege, 2004*, pp. 356–363
- [100] C. Thomser, U. Prah, H. Vegter, W. Bleck, in: *Proceeding of XIV Conference Comp. Methods in Mat. Sci, Zakopane, 14–17.01.2007*.
- [101] T. Sakaki, K. Ohnuma, K. Sugimoto, Y. Ohtakara, Plastic anisotropy of dual-phase steels, *International Journal of Plasticity*, Volume 6, Issue 5, 1990, Pages 591–613
- [102] Prodromos Tsipouridis, *Mechanical properties of Dual-Phase steels*, genehmigten Dissertation, 2006
- [103] <http://www.matthewpais.com/2dedgecrackinclusion>

[104] Abaqus Analysis User's Manual (6.12), 19.2.2 Damage initiation for ductile metals

[105] Abaqus Analysis User's Manual (6.12), 19.2.3 Damage evolution and element removal for ductile metals

ABSTRACT**EDGE FRACTURE PREDICTION OF DUAL PHASE STEELS WITH
CONSIDERATION OF MICROSTRUCTURES**

by

Ming Wen**December 2015****Advisor:** Professor Xin Wu**Major:** Mechanical Engineering**Degree:** Doctor of Philosophy

In recent years, Advanced High Strength Steels (AHSS) have been used for the lightweight structural design and manufacturing in automotive industry. This class of sheet metals are prone to edge fracture during stamping production, and the fracture often occurs at much lower strain than that predicted based on the forming limit curves. The uncertainty in predicting edge fracture represents a great challenge in the application of AHSS. This dissertation is focused on the better understanding of edge fracture phenomenon through experimental observation and computer modeling with the consideration of microstructure effect.

In this dissertation, Hole Expansion (HE) test was used to investigate the mechanisms of edge fracture of two AHSS, Dual Phase DP780 and DP980. The HE test includes two processing steps: hole punching and hole expanding. The punching process creates holes of various sheared edge morphologies, which are the input to the hole expanding process, along with the intrinsic property of material, produce a joint effect on the crack initiation and propagation on the sheared edges during HE test.

The hole punching process was first investigated. The sheared edges were analyzed with image processing, and the relative heights of sheared four edge zones were measured, which were used to determine the strain distributions of sheared edges. The punching process was further simulated with FEA, and referenced with the experimental observations. Fracture mechanism of hole punching process was deduced.

The process of crack initiation and propagation in hole expanding process was studied the next. Scanning Electron Microscope (SEM) was used to observe cracks on the sheared edges. FEA simulation

was applied to investigate the effect of sheared edge geometry on the stress evolution in the hole expanding process. The interaction of two neighboring parallel cracks in the crack propagation process was analyzed to explain the effect of crack population on the main crack propagation.

To investigate the microstructure effect on the edge fracture, the dual phase grain structure and its effect on mechanical properties and fracture behavior of DP steels were analyzed. Based on HE test results and observed DP steel grain structures, a criterion to predict edge fracture was proposed. This criterion includes mesoscale grain structure features of DP steels, and it can be applied to predict the HE test results of DP steels. The heterogeneous microstructures of DP steels were built into the Representative Volume Element (RVE) models to study the effects of microstructure parameters and fracture mechanisms on macroscale mechanical properties of DP steels, with damage based failure criteria applied to constituent ferritic and martensitic phases.

AUTOBIOGRAPHICAL STATEMENT**Ming Wen**

- 1983 Born in "Hu Garden", Tianmen, Hubei, P.R. China
- 1989-1996 Elementary School of Central China Normal University, Wuhan, Hubei, China
- 1996-1999 Wuluo Road Middle School, Wuhan, Hubei, China
- 1999-2002 No. 15 Middle School of Wuhan and No.1 Middle School of Zhijiang, Hubei, China
- 2002-2006 B.S., Vehicle Engineering, Wuhan University of Technology, Wuhan, Hubei, China
- 2006-2009 M.S., Vehicle Engineering, Wuhan University of Technology, Wuhan, Hubei, China
- 2009-2015 Ph.D., Mechanical Engineering, Wayne State University, Detroit, Michigan, U.S.A.